URANIUM OXIDES FOR SOLID-STATE DIRECT-CONVERSION NEUTRON DETECTION

A DISSERTATION IN
Physics
and
Chemistry

Presented to the Faculty of the University
of Missouri-Kansas City in partial fulfillment of
the requirements for the degree

DOCTOR OF PHILOSOPHY

by
SHAILESH DHUNGANA

B.Sc., Tribhuvan University, Nepal, 2007
M.Sc., Tribhuvan University, Nepal, 2012

Kansas City, Missouri
2020

URANIUM OXIDES FOR SOLID-STATE DIRECT-CONVERSION NEUTRON DETECTION

Shailesh Dhungana, Candidate for the Doctor of Philosophy in Physics and Chemistry
University of Missouri-Kansas City, 2020

ABSTRACT

This study is focused on studying the potential of uranium oxides as solid-state direct-conversion neutron detectors.

By modeling uranium oxides as neutron detectors, we found that thick detectors with suitable uranium isotopes would be required to achieve absorption probabilities of a few percentages: 1.5–4% for 10 MeV neutrons for natural uranium oxides, ~2% for 1 MeV neutrons for ^{235}U-based uranium oxides, and 7–9% for thermal neutrons for natural uranium oxides, assuming each detector is 1 cm thick. The leakage current associated with α-decay of uranium acts as the major source of noise in these materials, which imposes a minimum limit on the charge transport properties required to consider them for neutron detection. A charge carrier mobility of 1–10 $\mathrm{cm^2 \cdot V^{-1} \cdot s^{-1}}$ and carrier lifetime of 10^{-5}–10^{-4} s would be required to achieve a signal above the leakage current.

α-U_3O_8 pellets were fabricated with ~95% theoretical density and resistivity values on the order of 10^2–10^4 Ω-cm. The resistivity decreased slightly when the pellet composition was off-stoichiometric. The charge carrier mobility of these pellets could not

be determined due to the absence of a measurable signal and was estimated as less than 1 $cm^2 \cdot V^{-1} \cdot s^{-1}$ based on Hall effect measurements.

UO_3 pellets were fabricated with 85–90% of theoretical density. Most of these pellets, upon investigation with x-ray diffraction, were found to consist of ∼90% γ-UO_3 and ∼10% of α-$UO_2(OH)_2$. The direct and indirect band gap values of these pellets were ∼2 and ∼2.9 eV respectively and the resistivity values were on the order of 10^9–10^{10} Ω-cm. The charge carrier mobility could not be determined due to the absence of a measurable signal but the maximum value was estimated on the order of 10^{-2}–10^{-3} $cm^2 \cdot V^{-1} \cdot s^{-1}$ based on time-of-flight photoconductivity and steady-state space-charge-limited current methods. Our calculations showed that polaronic effects may be contributing to low charge carrier mobility in these materials.

The charge carrier mobility of uranium oxides must be increased to be able to measure and use these materials for neutron detection. Based on our understanding of these materials, we have proposed various methods that may be used to increase the charge carrier mobility, however, until the charge carrier mobility measurements are carried out, the potential of these materials for neutron detection will remain unclear.

APPROVAL PAGE

The faculty listed below, appointed by the Dean of the School of Graduate Studies have examined a dissertation titled “Uranium Oxides for Solid-State Direct-Conversion Neutron Detection”, presented by Shailesh Dhungana, candidate for Doctor of Philosophy in Physics and Chemistry, and certify that in their opinion it is worthy of acceptance.

Supervisory Committee

Anthony N. Caruso, Ph.D., Committee Chair
Department of Physics and Astronomy

Michelle M. Paquette, Ph.D., Dissertation Advisor
Department of Physics and Astronomy

Zhonghua Peng, Ph.D.
Department of Chemistry

Paul Rulis, Ph.D.
Department of Physics and Astronomy

Nathan A. Oyler, Ph. D.
Department of Chemistry

CONTENTS

ABSTRACT iii

LIST OF ILLUSTRATIONS xiii

LIST OF TABLES xix

ACKNOWLEDGEMENTS xxi

CHAPTER 1. INTRODUCTION 1

- 1.1. Motivation and Objectives 1
- 1.2. Neutron Detection 3
  - 1.2.1. Free Neutron Interactions with Matter 3
    - 1.2.1.1. Scattering 4
    - 1.2.1.2. Absorption 4
  - 1.2.2. Neutron Interaction Cross-Section 5
  - 1.2.3. Neutron Detection Efficiency 8
  - 1.2.4. Neutron Detectors 9
    - 1.2.4.1. Gas-Filled Neutron Detector 9
    - 1.2.4.1.1. Gas-Based Thermal Neutron Detectors 10
    - 1.2.4.1.2. Gas-Filled Fast Neutron Detectors 10
    - 1.2.4.2. Solid-State Neutron Detectors 10
    - 1.2.4.2.1. Indirect-Conversion Neutron Detector 11
    - 1.2.4.2.2. Direct-Conversion Neutron Detector 12
- 1.3. Solid-State Direct-Conversion Neutron Detector Requirements 13

1.4. Uranium Oxide Semiconductors for Neutron Detection....................................15

1.4.1. Uranium Dioxide (UO_2) 17

1.4.2. Triuranium Octoxide (U_3O_8) 18

1.4.3. Uranium Trioxide (UO_3) 19

1.5. Summary 20

1.6. Outline of Dissertation 22

CHAPTER 2. THEORY AND MODELING 23

2.1. Efficiency of a Direct-Conversion Solid-State Neutron Detector......................24

2.2. Neutron Absorption Probability of Uranium Oxide 31

2.3. Charge Excitation in Uranium Oxide Detectors..37

2.4. Leakage Current: Effect of α-Particle Decay 37

2.5. Transport Properties Requirements 45

2.6. Evaluation of Potential Detector Efficiency..47

2.7. Summary 49

CHAPTER 3. METHODS: THEORY AND EXPERIMENTAL PROCEDURE 52

3.1. Fabrication of U_3O_8 Pellets (UTK)...52

3.1.1. U_3O_8 Powder Preparation 53

3.1.2. Pressing of U_3O_8 Pellets 53

3.1.3. U_3O_8 Pellet Sintering..53

3.1.4. $U_3O_{8\pm x}$ Sample Preparation..54

3.2. Fabrication of UO_3 Pellets (UTK) 54

3.2.1. UO_3 Powder Preparation by Decomposition of Uranyl Nitrate..................54

3.2.1.1. Theory 54

3.2.1.2. Experiment 55

3.2.2. UO_3 Powder Preparation from Commercially Available Material 55

3.2.3. Uniaxial Hot Pressing of UO_3 Pellets..55

3.3. Basic Characterization of Pellets (UTK) 56

3.3.1. Density...56

3.3.2. Stoichiometry...56

3.3.2.1. Redox Titration...57

3.3.2.1.1. Theory 57

3.3.2.1.2. Experiment 58

3.3.2.2. Inductively Coupled Plasma Mass Spectrometry...............................58

3.3.3. Phase Determination: X-ray Diffraction..59

3.3.4. Sample Polishing and Grain Size Measurement..59

3.4. Device Fabrication: Contact Deposition and Wiring (UMKC)..........................60

3.5. Electronic Structure Study: Band Gap (UMKC)..60

3.5.1. Diffuse Reflectance Spectroscopy: Theory 61

3.5.2. Kubelka–Munk Theory 62

3.5.3. Determination of Band Gap: Experiment...63

3.6. Electronic Structure: Computational Studies: Theory (UMKC)........................65

3.6.1. Density Functional Theory 67

3.6.2. The Hohenberg and Kohn Theorems 67

3.6.3. The Kohn–Sham Equations 68

3.6.4. Approximate Exchange-Correlation Functionals......................................70

3.6.5. The Hubbard Coefficient (DFT+U) 72

3.6.6. Pseudopotentials..72

3.6.7. Density of States 74

3.6.8. Electronic Structure Calculation 74

3.7. Resistivity Measurement (UMKC)..75

3.7.1. Four-Point Probe – van der Pauw 76

3.7.1.1. Theory...76

3.7.1.2. Experiment 77

3.7.2. Four-Point Probe – Linear 78

3.7.2.1. Theory...78

3.7.2.2. Experiment 79

3.7.3. Metal–Insulator–Metal Heterostructure 80

3.8. Charge Carrier Mobility Measurements (UMKC) 82

3.8.1. DC Hall Effect Measurement..88

3.8.1.1. Theory...88

3.8.1.2. Experiment 90

3.8.2. Steady-State Space-Charge-Limited Current..91

3.8.2.1. Theory...91

3.8.2.2. Experiment 93

3.8.3. Time of Flight Photoconductivity 94

3.8.3.1. Requirements for the ToF Photoconductivity Experiment 96

3.8.3.2. Choice of Electrodes 97

3.8.3.3. ToF Photoconductivity Experiment 101

3.9. Mobility–Lifetime Measurements (UMKC) 101

3.9.1. Theory 101

3.9.2. Mobility–Lifetime from ToF Photoconductivity: Theory 102

3.9.3. Mobility–Lifetime from Steady-State Photoconductivity: Experiment 103

CHAPTER 4. RESULTS AND DISCUSSIONS: U_3O_8 104

4.1. Stoichiometric U_3O_8 Sample Preparation 104

4.2. Basic Characterization 108

4.2.1. Density of Stoichiometric U_3O_8 Samples 108

4.2.2. Microstructure of Stoichiometric U_3O_8 Samples 109

4.2.3. X-ray Diffraction of Stoichiometric U_3O_8 Samples 110

4.3. Resistivity of Stoichiometric U_3O_8 Samples 111

4.4. Nonstoichiometric U_3O_8 Sample Preparation 116

4.5. Basic Characterization 118

4.5.1. Density of Non-Stoichiometric U_3O_8 Samples 118

4.5.2. Microstructure of Non-Stoichiometric U_3O_8 Samples 119

4.5.3. Stoichiometry of Non-Stoichiometric U_3O_8 Samples 120

4.5.4. Resistivity of Non-Stoichiometric U_3O_8 Samples (UTK) 121

4.6. Charge Carrier Mobility: Hall Effect Measurements 123

4.7. Summary 124

CHAPTER 5. RESULTS AND DISCUSSIONS: UO_3 126

5.1. UO_3 Sample Preparation 126
5.2. Basic Characterization 131
5.2.1. Density of UO_3 Samples 131
5.2.2. Microstructure of UO_3 Samples 133
5.2.3. Stoichiometry of UO_3 Samples 133
5.2.4. Phase of UO_3 Samples 134
5.3. Electronic Structure Study: Band Gap 137
5.4. Resistivity 143
5.5. Charge Carrier Mobility from Space-Charge-Limited-Current 146
5.6. Mobility and Mobility–Lifetime of Charge Carriers from Photoconductivity 147
5.6.1. Discussion on Potential Ways to Improve Charge Carrier Mobility 151
5.6.1.1. Effective Mass 151
5.6.1.2. Scattering 152
5.6.1.3. Ways to Increase Charge Carrier Mobility 153
5.6.1.4. Computational Studies of Electronic Structures of UO_3 and Mixed Crystals 154
5.7. Polaronic Effect in UO_3 158
5.8. Summary 161
CHAPTER 6. CONCLUSION AND FUTURE WORK 164
APPENDIX A: EXAMPLE VASP INPUT FILES 168
APPENDIX B: I–V MEASUREMENTS ON U_3O_8 171
APPENDIX C: HALL EFFECT MEASUREMENTS ON U_3O_8 174

APPENDIX D: BAND GAP ANALYSIS OF UO_3 175

APPENDIX E: I–V MEASUREMENTS ON UO_3 180

APPENDIX F: HIGH VOLTAGE MEASUREMENTS ON UO_3 182

APPENDIX G: ELECTRONIC STRUCTURE OF MIXED CRYSTALS OF UO_3.... 183

REFERENCES 185

VITA 205

LIST OF ILLUSTRATIONS

Figure 1. Microscopic cross-section of nuclei that produce moderate-to-high-energy charged particles for the reactions given in Table 1 [23]. 6

Figure 2. Representation of a planar detector: (a) indirect-conversion (b) direct-conversion. 13

Figure 3. Fast neutron cross-section of nuclei that produce moderate-to-high-energy charged particles for the reactions given in Table 1. 16

Figure 4. Representation of a detector of thickness d; x represents a point in the detector at which the incident neutrons are absorbed. 26

Figure 5. Analysis of CCE for different detector configurations: (a) CCE vs $\mu\tau$ for different detector thicknesses and electric fields; (b) CCE vs electric field for different detector thicknesses and $\mu\tau$ values; (c) CCE vs detector thickness for different electric fields and $\mu\tau$ values; (d) CCE vs charge carrier drift length ($\mu\tau E$) for different detector thicknesses. 28

Figure 6. Representation of a detector of thickness d with x as a boundary that separates two regions in the detector: all of the neutrons absorbed to the left are detected while all of those absorbed to the right are not. 29

Figure 7. Detection probability per absorbed neutron of a UO_3 detector as a function of charge carrier $\mu\tau$ for 10 MeV neutrons when the minimum charge collection efficiency is set to 1, 10, and 25%. Here we have considered a detector thickness of 1 cm with an electric field set at 1000 V·cm^{-1}..31

Figure 8. Absorption probability as a function of detector thickness: (a) of 1 MeV neutrons for UO_3 detectors with different ^{235}U content (b) of thermal neutrons for detectors based on different O/U ratios. 34

Figure 9. Photo-fission cross-section of ^{238}U and ^{235}U as a function of γ-ray energy. Data taken from [23]. 38

Figure 10. Detection efficiency as a function of charge carrier $\mu\tau$ of natural UO_2 detectors for thermal neutrons: (a) electric field of 10^4 V·cm^{-1} applied across detectors of different thicknesses (b) 1 cm thick detector with different electric fields. 48

Figure 11. Plot to obtain the band gap of a material using Tauc's method. 63

Figure 12. Schematic of experimental set up for diffuse reflectance spectroscopy. 65

Figure 13. Optical fiber arrangement at different instruments. 65

Figure 14. Schematic illustration of an all-electron potential (dashed lines) and a pseudopotential (solid lines) and the associated wave functions; r_c is the cut-off radius [136]. 73

Figure 15. (a) A schematic for a circular sample with four-point contacts for van der Pauw resistivity measurement; (b) A U_3O_8 sample in the van der Pauw probe system. 77

Figure 16. (a) Schematic of linear 4-point probe resistivity measurement (b) a U_3O_8 sample wired for resistivity measurement in a 4-point linear probe configuration. 80

Figure 17. (a) Circuit diagram to measure resistivity in the MIM geometry with a guard ring (b) Representation of top view of a sample in an MIM structure with a guard ring. 81

Figure 18. *I–V* measurement in MIM geometry (a) without a guard ring (b) with a guard ring. 82

Figure 19. A typical dark-injection space-charge-limited current signal. The top graph represents the applied voltage pulse whereas the bottom graph represents the signal observed. 85

Figure 20. Representation of an ideal transient current obtained in the CELIV experiment. The top graph represents the applied voltage ramp whereas the bottom graph represents the signal observed. Here, $j(0)$ is the current due to the capacitance of the sample and Δj is the difference between maximum current density and $j(0)$. 86

Figure 21. A schematic of the Hall effect for an *n*-type semiconductor. 89

Figure 22. U_3O_8 sample in van der Pauw geometry placed in a magnetic field. 91

Figure 23. Circuit for high-voltage *I–V* measurements. 93

Figure 24. A schematic of the ToF photoconductivity experiment. 95

Figure 25. A typical signal obtained from a ToF photoconductivity experiment...........96

Figure 26. Band line up of gold and UO_3 (a) when they are apart, and (b) when they are in contact...98

Figure 27. *I–V* characteristics of a Schottky diode made from UO_3 using gold as contacts [168] (Reprinted from Vacuum, 83/1, T.T. Meek and B. von Roedern, Semiconductor devices fabricated from actinide oxides, 226–228, Copyright (2008), with permission from Elsevier)..99

Figure 28. Transmittance of thin gold films deposited by thermal evaporation [169] (Reprinted from Physics Procedia, 32, A. Axelevitch, B. Gorenstein, and G. Golan,

Investigation of Optical Transmission in Thin Metal Films, 1–13, Copyright (2012), with permission from Elsevier)....................100
Figure 29. Transmittance of a 25 nm thick gold film deposited by resistive heating...100
Figure 30. Schematic of the experimental set-up for steady-state photoconductivity..103
Figure 31. Density of the stoichiometric U_3O_8 samples as a function of sintering times (a) pellets fabricated with die A (b) pellets fabricated with die B. 109
Figure 32. Average grain size of stoichiometric U_3O_8 pellets as a function of sintering time....................110
Figure 33. X-ray diffraction spectra for a stoichiometric U_3O_8 pellet sintered at 1350 °C for 12 hours....................111
Figure 34. Results of 4-point *I–V* measurements on sample A0403....................113
Figure 35. Resistivity of stoichiometric U_3O_8 samples (a) as a function of density (b) as a function of grain size. 114
Figure 36. Resistivity of stoichiometric U_3O_8 samples as a function of sintering time. 114
Figure 37. Density of $U_3O_{8\pm x}$ sintered at 1000 °C for different durations 119
Figure 38. Grain size of nonstoichiometric $U_3O_{8\pm x}$ as a function of sintering time for different oxygen environments. 120
Figure 39. Resistivity of $U_3O_{8\pm x}$ samples as a function of grain size....................122
Figure 40. Resistivity as a function of stoichiometry of nonstoichiometric $U_3O_{8\pm x}$ samples: (a) when all the resistivity values are considered. (b) when the outlier value of resistivity is left out....................123

Figure 41. Results of Hall effect measurements showing no discernible Hall voltage.124

Figure 42. Density of the pellets that were assigned as γ-UO_3 as a function of powder conditioning temperature. 132

Figure 43. Density of the UO_3 pellets as a function of their press time for pellets that were pressed at 180 °C with a load of 4.5 ton. 132

Figure 44. Grain size of the UO_3 pellets as a function of their density for pellets that were fabricated by pressing at 180 °C with a load of 4.5 ton for 10 minutes. 133

Figure 45. X-ray diffraction data of some UO_3 samples: (a) data that do not show aluminum peaks (b) data that show aluminum peaks. 136

Figure 46. X-ray diffraction pattern of sample 423 with Rietveld refinement overlay showing the best matches with α-UO_3 and α-$UO_2(OH)_2$. 137

Figure 47. Representation of energy bands of a semiconductor (*n*-type). 138

Figure 48. Band gap analysis of some representative samples: (a) sample 205, prepared without powder conditioning (b) sample 223, prepared without powder conditioning (c) sample 423, characterized as α-UO_3, and (d) sample 518, characterized as γ-UO_3......141

Figure 49. *I–V* characteristics of (a) samples 501 (b) sample 427. 144

Figure 50. Resistivity of the UO_3 samples as a function of their density....................145

Figure 51. Resistivity of the UO_3 samples as a function of their grain size. 145

Figure 52. *I–V* characteristic of sample 410 measured using high-voltage program/circuit. 147

Figure 53. Results of steady-state photoconductivity experiments on sample 203, 410 and 250.10.8. 148

Figure 54. Transient photocurrent signal for different voltages for samples 203 and 250.10.8. 150

Figure 55. PDOS of γ-UO_3 calculated by the DFT+U method showing that the conduction band of γ-UO_3 consists of mainly 5*f*- and 6*d*-orbitals of U and 2*s*-orbitals of O. (a) conventional representation (b) log-scale used in y-axis for a better view of all the states. 156

Figure 56. PDOS of conduction band of Cr-mixed UO_3 157

Figure 57. Comparison of contribution of cation *s*-orbital to the conduction band in UO_3 and Cr-mixed UO_3 157

LIST OF TABLES

Table 1. Nuclear reactions that produce moderate-to-high-energy charged particles. 6

Table 2. The chemical composition of some common hydrates of UO_3........................20

Table 3. Fission cross-sections of ^{238}U and ^{235}U for thermal and fast neutrons. Data taken from [23]. 32

Table 4. Macroscopic cross-section (Σ) and mean penetration depth (λ) of thermal and fast neutrons for different uranium oxides. 35

Table 5. Absorption probability of thermal and fast neutrons of different uranium oxide detectors 1 and 10 mm thick. 36

Table 6. Charge excited by α-particles and corresponding $\mathrm{CCE}_{\mathrm{min}}$ in uranium oxide with different uranium isotopic compositions for detector areas of 1×1 cm^2 and 0.5×0.5 cm^2. Here we have assumed a charge carrier transit time of 0.1 ms....................................43

Table 7. Charge excited by α-particles in uranium oxides for different isotopes in different integration times in detectors of thicknesses of 1 and 10 mm with cross-sectional area of 1 cm^2...44

Table 8. Detection efficiency of natural UO_2 detectors,1 and 10 mm thick, operating at electric fields of 10^3 and 10^4 $\mathrm{V \cdot cm^{-1}}$, if the charge carrier mobilities are 1 and 10 $\mathrm{cm^2 \cdot V^{-1} \cdot s^{-1}}$. Each detector is assumed to have a cross-sectional area of 1 cm^2 and charge carrier lifetime of 10^{-4} s. The integration time is set equal to the charge carrier transit time. The minimum CCE is set equal to the charge excited by α-particles within the integration time. A missing detection efficiency value means that there is no detection because the charge excited by fission fragments is smaller than that by α-particles. 49

Table 9. Sintering time and density of stoichiometric U_3O_8 pellets fabricated using die A. 105

Table 10. Sintering time and density of stoichiometric U_3O_8 pellets fabricated using die B. 107

Table 11. Resistivity of stoichiometric U_3O_8 samples. 115

Table 12. Resistivity and stoichiometry of non-stoichiometric U_3O_8 sintered at 1000 °C in varying oxygen environment. 117

Table 13. Processing conditions and properties of UO_3 samples. 128

Table 14. Band gap and resistivity of UO_3 samples. 142

ACKNOWLEDGEMENTS

I would like to express my sincere graduate to my research advisors Professor Michelle M. Paquette and Professor Anthony N. Caruso for providing me the guidance, opportunity, and financial support to pursue my studies. I would also like to thank Professor Paul Rulis, Professor Zhonghua Peng, and Professor Nathan Oyler for their contribution and time in serving as the members of my Ph.D. Supervisory Committee.

I would like to thank Professor Thomas T. Meek and the members of his research group, especially Brandon Shaver and Seth Lawson, at The University of Tennessee, Knoxville for the collaborating with us and preparing samples. I would also like to thank Professor James Murowchick at UMKC for allowing me to use his x-ray diffractometer and teaching me the data acquisition process. Similarly, I want to thank Professor David van Horn at UMKC for discussions on uranium oxides and doping of semiconductors. I would also like to thank the Radiation Safety Offices at both UTK and UMKC.

I want to thank my wife Puja for helping me with electronic structure calculations and providing me support and encouragement. I would like to express my gratitude to Gyanendra Bhattarai for his guidance. My friend Rupak Thapa deserves a special mention for his support and contribution with LabView-based programs. A special thanks to Mark Pederson for constantly encouraging me. I would also like to thank all the fellows in our research group; all of them have contributed in some way to this research.

This work was funded by the Defense Threat Reduction Agency, award no. HDTRA1-15-1-0072.

CHAPTER 1. INTRODUCTION

1.1. Motivation and Objectives

Detecting neutrons is very important in multiple fields, including nuclear power production [1]–[4], non-proliferation of nuclear weapons [5], medical physics [6], [7], as well as fundamental scientific research such as space physics [8], [9] and material characterization [10], [11]. In most of these areas, traditional ^{3}He-based detectors are used. Although these detectors offer high detection efficiency, they suffer from drawbacks such as high-power requirements and sensitivity to microphonics (conversion of mechanical vibrations to electrical signal). They are usually large in size, which makes them inconvenient to use for portable radiation monitoring devices [12]–[14]. Additionally, ^{3}He is a relatively rare gas and is getting increasingly expensive and difficult to source [15]–[17]. These demerits of traditional neutron detectors have encouraged scientists to search for alternatives.

An alternative to traditional neutron detectors is a class of detectors called direct-conversion solid-state neutron detectors, which consist of a semiconductor device made up of a material that can absorb neutrons. Direct-conversion solid-state devices can in theory offer very high neutron detection efficiency. However, they have been difficult to achieve in practice due to challenges in finding materials that simultaneously meet the necessary criteria, including high neutron absorption, high charge carrier mobility, and low leakage current, among other features such as processability and stability. At present, ^{10}B- and ^{6}Li-based semiconductors are regarded as two of the best candidates for direct-conversion neutron detectors, mainly because of their high thermal neutron cross-sections (i.e., high interaction probability) and the relatively high energy of their primary reaction products (i.e., high signal current possible). However, there are a few other isotopes that could potentially be used in neutron detection that have not yet been fully explored. One such material is uranium. Uranium-based semiconductors have previously been proposed as potential neutron detector materials [18], and uranium dioxide has been studied in this context with some promise [19]–[21]. Additionally, ^{238}U has been used in conjunction with a silicon charged particle detector to detect neutrons with partial success [22]. However, there has been no systematic study of uranium-based materials for neutron detection applications.

Uranium-based semiconductors are of interest for neutron detection because uranium (^{238}U, ^{235}U) nuclei undergo neutron-induced fission to yield primary reaction products with a very high energy (>165 MeV) [18]. Such high energy deposition in the detector material can excite a large number of electron–hole (e–h) pairs, which is at least two orders-of-magnitude higher than in ^{10}B- or ^{6}Li-based materials. The excitation of such a large quantity of charge could potentially help to overcome the limitations of poor carrier mobility, high leakage current, and other inadequate charge transport properties that have historically hindered the progress of direct-conversion neutron detectors.

The objective of this work is to study the efficacy or uranium oxides as direct-conversion solid-state neutron detectors. This work is divided into three parts: (1) modeling uranium oxide (UO_2, U_3O_8, and UO_3) as a detector material to evaluate the required charge transport properties and potential detection efficiency, (2) fabricating pressed pellets of U_3O_8 and UO_3 and studying their basic physical/chemical properties (density, grain size, stoichiometry, and phase), and (3) studying the electronic and charge transport properties of these materials as a function of fabrication conditions, towards understanding the range of material properties possible and establishing a path for optimization.

1.2. Neutron Detection

In order to detect a neutron directly, one would have to utilize the interaction(s) based on its intrinsic properties, such as translation momentum, quantum mechanical spin, and/or proposed electric dipole moment. However, this is impractical or impossible due to either insufficient interaction energy and/or lack of advanced technology to measure such a tiny amount of energy and interpret the result of the measurements. While it may seem possible to detect neutrons directly by utilizing their primary reaction with matter, this is possible only under strict laboratory conditions. Therefore, almost all neutron detection technologies use the higher-order products of interaction between neutrons and matter [18]. These higher-order products are electron–ion pairs in gas-based detectors and electron–hole pairs in semiconductor detectors, which are collected in the form of electric pulses by applying an electric field across the detector.

1.2.1. Free Neutron Interactions with Matter

In order to understand neutron detection technology, it is imperative to understand the way in which a free neutron interacts with matter. Since a neutron is electrically neutral, it does not electrostatically interact with either protons or electrons. However, it can interact with an atomic nucleus by one of the two mechanisms: scattering and absorption. These interactions are described in the following sections.

1.2.1.1. Scattering

A free neutron is said to be scattered by a nucleus if the kinetic energy of the former is transferred to the latter. The scattering process can be either elastic or inelastic. In elastic scattering interactions, some portion of the kinetic energy of the incident neutron is transferred to the recoil nucleus; the total kinetic energy of the scattered neutron–recoil nucleus system is equal to the kinetic energy of the system before the scattering event. In inelastic scattering interactions, some portion of the kinetic energy of the incident neutron is transferred to the recoil nucleus as kinetic energy while some portion is transferred as excitation energy to the recoil nucleus such that the total kinetic energy of the scattered neutron–recoil nucleus system is not conserved.

1.2.1.2. Absorption

A free neutron is said to be absorbed by a nucleus if the nucleus goes to an "excited state" by capturing the free neutron. The excited nucleus, sometimes also referred to as a compound nucleus, can undergo de-excitation by four different modes, dividing the absorption interaction into four types: radiative capture, fission, neutron emission (or neutron multiplicity), and charged particle emission. In radiative capture, a compound nucleus de-excites by emitting one or more γ-rays. In fission, a compound nucleus de-excites by splitting into two smaller nuclei, called fission fragments or daughter nuclei, while simultaneously emitting one or more neutrons and/or γ-rays. In neutron emission interactions, a compound nucleus de-excites by emitting one or more neutrons. In charged particle emission, a compound nucleus de-excites by emitting one or more charged particles, such as α-particles and protons.

1.2.2. Neutron Interaction Cross-Section

There is a finite probability of occurrence of each type of interaction between a neutron and a given material. This probability is expressed in terms of microscopic cross-section. The microscopic cross-section of a nucleus is a function of neutron energy. That means, any material will have a microscopic scattering cross-section and a microscopic absorption cross-section (one for each of the four types) as a function of neutron energy. The microscopic cross-section of a material is defined as the ratio of the probability of neutron absorption relative to the number of absorbing nuclei per unit area. Physically, it represents the effective area of a nucleus in a target that can interact with incident neutrons. The microscopic cross-section is measured in units of barn (1 barn = 10^{-28} m^2). In this dissertation, microscopic cross-section (or simply the cross-section) of a nucleus refers to the cross-section for charged particle emission except in the case of uranium, for which it refers to the cross-section for fission (sometimes also called the fission cross-section). The microscopic cross-section of nuclei that produce moderate-to-high-energy charged particles is shown in Figure 1. The cross-section data was obtained from [23] and the corresponding reactions are provided in Table 1 [18].

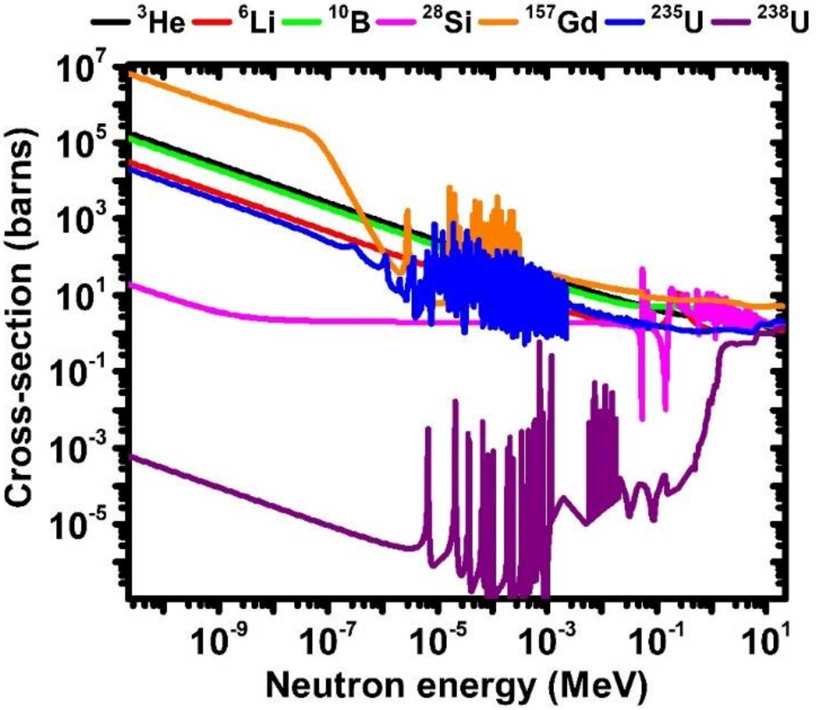

Figure 1. Microscopic cross-section of nuclei that produce moderate-to-high-energy charged particles for the reactions given in Table 1 [23].

Table 1. Nuclear reactions that produce moderate-to-high-energy charged particles.

Isotope	**Reaction**	***Q*-value (MeV)**
^{3}He	${}^{1}_{0}\mathrm{n} + {}^{3}_{2}\mathrm{He} \longrightarrow {}^{3}_{1}\mathrm{H} + {}^{1}_{1}\mathrm{H}$	0.764
^{6}Li	${}^{1}_{0}\mathrm{n} + {}^{6}_{3}\mathrm{Li} \longrightarrow {}^{3}_{1}\mathrm{H} + {}^{4}_{2}\mathrm{He}$	4.783
^{10}B	${}^{1}_{0}\mathrm{n} + {}^{10}_{5}\mathrm{B} \longrightarrow {}^{7}_{3}\mathrm{Li} + {}^{4}_{2}\mathrm{He}$	2.312
^{28}Si	${}^{1}_{0}\mathrm{n} + {}^{28}_{14}\mathrm{Si} \longrightarrow {}^{28}_{13}\mathrm{Al} + {}^{1}_{1}\mathrm{H}$	–3.840
^{157}Gd	${}^{1}_{0}\mathrm{n} + {}^{157}_{64}\mathrm{He} \longrightarrow {}^{0}_{-1}\mathrm{e} + \gamma$	0.079
^{235}U	${}^{1}_{0}\mathrm{n} + {}^{235}_{92}\mathrm{U} \longrightarrow {}^{A_1}_{Z_1}\mathrm{X}_1 + {}^{A_2}_{Z_2}\mathrm{X}_2 + x\,{}^{1}_{0}\mathrm{n}$	199.9
^{238}U	${}^{1}_{0}\mathrm{n} + {}^{238}_{92}\mathrm{U} \longrightarrow {}^{A_1}_{Z_1}\mathrm{X}_1 + {}^{A_2}_{Z_2}\mathrm{X}_2 + x\,{}^{1}_{0}\mathrm{n}$	199.9

Beyond the microscopic cross-section of a material, there is the macroscopic cross-section, Σ, which represents the effective area of all the nuclei present in a unit volume of the material that can interact with incident neutrons. The macroscopic cross-section of a material is related to its microscopic cross-section (σ) as:

$$\Sigma = n\sigma \tag{1.1}$$

where n is the number of nuclei per unit volume of the material.

The reciprocal of the macroscopic cross-section is the neutron mean free path (sometimes also referred to as its mean penetration depth), which is the thickness of material that decreases the number of neutrons to $1/e$ times the incident quantity.

If we consider a target material of cross-section A and thickness d, which contains N_n number of nuclei, then the number of nuclei per unit volume in the material is given as:

$$n = \frac{N_n}{Ad} \tag{1.2}$$

Now, if p is the probability that a neutron is absorbed by the material, then from the definition of microscopic cross-section:

$$\sigma = \frac{p}{N_n/A} \tag{1.3}$$

Using Equations (1.2) and (1.3) in Equation (1.1), we have:

$$\Sigma = \frac{p}{d} \tag{1.4}$$

Thus, the macroscopic cross-section of a material can also be defined as the absorption probability per unit thickness. It is measured in units of cm^{-1}.

Now in terms of molar mass, M, Avogadro's number, N_A, and material density, ρ, Equation (1.2) can be expressed as:

$$n = \frac{N_A}{M}\rho \tag{1.5}$$

Substituting Equation (1.5) in Equation (1.1), we get:

$$\Sigma = \frac{N_A}{M}\rho\sigma \tag{1.6}$$

Until this point, we have assumed that a target material is made up of a single type of atom. Equation (1.6) can be extended to a compound material, which consists of n_i number of i type of nuclei of microscopic cross-section, σ_i, as:

$$\Sigma = \sum_i \frac{N_A}{M}\rho\sigma_i n_i \tag{1.7}$$

1.2.3. Neutron Detection Efficiency

For neutron detectors, efficiency is divided into two categories: intrinsic and absolute. The intrinsic efficiency (ϵ_{int}) of a neutron detector is defined as the ratio of the number of electric pulses recorded to the number of neutrons incident on the detector. The absolute efficiency (ϵ_{abs}) of a neutron detector is defined as the ratio of the number of electric pulses recorded to the number of neutrons emitted by a source. For neutrons of fixed energy, the intrinsic detection efficiency of a detector depends on its properties only, whereas the absolute detection efficiency depends not only on the detector properties but also on the details of counting geometry, such as distance and solid angle between the source and the detector. The two efficiencies are related by $\epsilon_{int} = \epsilon_{abs} \cdot (4\pi/\Omega)$, where, Ω is the solid angle for the detector seen from the actual source position.

1.2.4. Neutron Detectors

A neutron detector consists of a target material—either gas-based or semiconductor-based—that can interact with incident neutrons to produce energetic charged particles. These energetic charged particles excite charge carriers—electron–ion pairs in a gas and electron–hole pairs in a semiconductor—within the detector material. These charge carriers are collected at the respective electrodes by applying an electric field, and electric pulses are recorded, leading to neutron detection.

1.2.4.1. Gas-Filled Neutron Detector

A gas-filled neutron detector consists of a metallic tube filled with a gas that can interact with neutrons. A conducting wire, insulated from the body of the tube, runs along its axis. A potential difference is applied in such a way that the tube acts as a cathode and the wire acts as an anode. When a neutron interacts with the gas inside the chamber, either absorption or scattering of neutron occurs, which subsequently leads to electron–ion pair (sometimes simply called ion pair) generation. These electron–ion pairs give rise to an electric signal as they are collected at the electrodes through the application of a suitable electric field. Based on the initial energy of the detected neutrons, gas-filled neutron detectors can be either thermal (neutron energy ≈ 25 meV) or fast (neutron energy > 1 MeV) detectors. These are discussed in the following sections.

1.2.4.1.1. Gas-Based Thermal Neutron Detectors

The commonly used gases for thermal neutron detection are helium (^{3}He) and boron trifluoride ($^{10}BF_3$). The associated reactions are [24]:

$$^{3}_{2}\mathrm{He} + ^{1}_{0}\mathrm{n} \longrightarrow ^{3}_{1}\mathrm{H} + ^{1}_{1}\mathrm{H} + 0.765\ \mathrm{MeV}$$

$$^{10}_{5}\mathrm{B} + ^{1}_{0}\mathrm{n} \longrightarrow ^{4}_{2}\mathrm{He} + ^{7}_{3}\mathrm{Li} + \gamma\ (0.48\ \mathrm{MeV}) + 2.31\ \mathrm{MeV}$$

$$^{10}_{5}\mathrm{B} + ^{1}_{0}\mathrm{n} \longrightarrow ^{4}_{2}\mathrm{He} + ^{7}_{3}\mathrm{Li} + 2.79\ \mathrm{MeV}$$

These reactions yield energetic ions, which give rise to ion pairs inside the chamber. An externally applied voltage separates the ion pairs, which gives rise to a detectable electrical signal in the external circuit.

1.2.4.1.2. Gas-Filled Fast Neutron Detectors

These detectors rely on the recoil of gas nuclei due to an elastic scattering interaction between the nuclei and an incident free neutron. During the interaction, a portion of the kinetic energy of the incident neutron is transferred to the nuclei of the fill-gas. The recoil nuclei then ionize the gas to excite ion pairs. These ion pairs are collected at the respective electrodes, giving rise to an electrical signal. The commonly used gases for these types of detectors are helium (^{4}He) and methane (CH_4).

1.2.4.2. Solid-State Neutron Detectors

The development of solid-state neutron detectors has been gaining rapid interest because of their advantages over their conventional gas-based counterparts. Compared to traditional neutron detectors, solid-state neutron detectors offer potential improvement in multiple areas such as design, stability, operating power, size, cost, versatility, and efficiency [14]. Solid-state neutron detectors are divided into two categories: indirect- and direct-conversion.

1.2.4.2.1. Indirect-Conversion Neutron Detector

In a simple planar configuration, an indirect-conversion neutron detector uses a conversion layer—a layer of material that can interact with neutrons—on top of a semiconductor detector (Figure 2(a)). The interaction of a neutron with a nucleus in the top layer produces two high-energy product particles. One of the product particles moves through the conversion layer to excite e–h pairs in the detector, which are subsequently collected in the external circuit and detected. The remaining product particle travels in the opposite direction (i.e., away from the detector, due to conservation of momentum) and therefore does not contribute to exciting e–h pairs, causing an inherent signal loss. The conversion layer has a conflicting thickness requirement: it should be thick enough to absorb a maximum number of incident neutrons, yet thin enough so that the product particle(s) can travel through it to reach the detector without a significant loss in kinetic energy. This limits the detection efficiency of these detectors to about 5% [19]. The detection efficiency can be improved by sandwiching the conversion layer between two detectors, thereby utilizing the energy of both the product particles in exciting e–h pairs; however, self-absorption of the primary reaction products still occurs. An efficiency of up to 12% has been reported for such detectors [25]. An improved efficiency can be achieved by inserting the conversion layer into trenches within a semiconductor, a configuration commonly known as a microstructured semiconductor neutron detector (MSND). Of the different types of indirect-conversion neutron detectors, MSNDs are known to offer maximum efficiencies [26]. The state-of-the-art microstructured thermal neutron detectors with ^{6}Li as a conversion layer, manufactured by RDT Inc., have a reported detection efficiency of 30% [27].

1.2.4.2.2. Direct-Conversion Neutron Detector

A direct-conversion neutron detector consists of a semiconductor detector that can itself interact with incident neutrons (Figure 2(b)). It can therefore be used in a simple planar configuration to achieve maximum efficiency. Both the primary reaction products formed within the detector take part in exciting e–h pairs, thereby eliminating the inherent signal loss that exists in indirect-conversion devices. The detection efficiency of a direct-conversion neutron detector can be much higher than that of an indirect-conversion neutron detector, approaching 100% [13], [18], [28]. This has been supported by the recent development of a prototype direct-conversion neutron detector based on hexagonal boron nitride, which has a reported detection efficiency of 58%, with the potential for additional efficiency improvements [29].

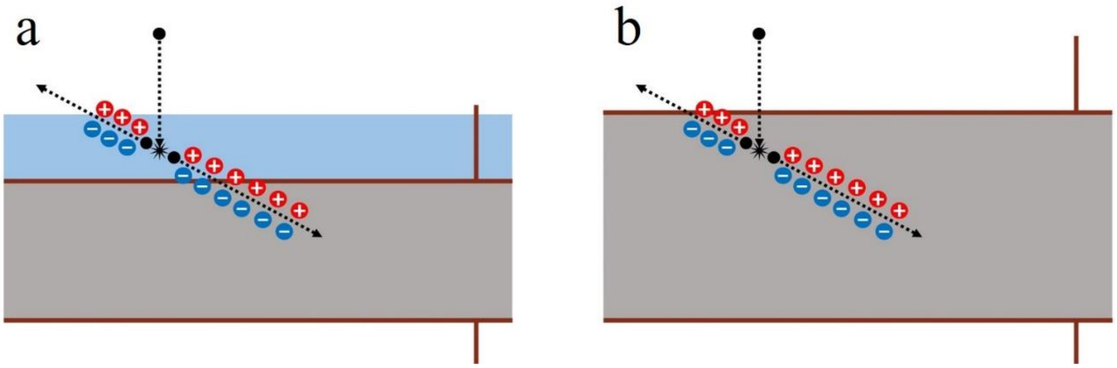

Figure 2. Representation of a planar detector: (a) indirect-conversion (b) direct-conversion.

1.3. Solid-State Direct-Conversion Neutron Detector Requirements

Despite vigorous research in the area, solid-state direct-conversion neutron detectors have not been achieved in practice due to a lack of suitable materials. Some general properties that should be considered for direct-conversion neutron detector materials include neutron cross-section (both microscopic and macroscopic), energy of the primary reaction products, charge transport properties (charge carrier mobility, lifetime, and mobility–lifetime product), resistivity/leakage current, end electronic structure (band gap, band line up).

It is obvious that a detector material should have a high microscopic cross-section so that the probability of interaction between the material and an incident neutron is maximized [24]. Higher interaction probability may lead to higher detection probability (although this is not strictly true, since there are other factors that play an equally important role in detection). In addition, it is convenient to have a material with a high macroscopic cross-section, since this will enable a thinner detector, which is extremely important in terms of the miniaturization and portability of a detector.

The energy of the primary reaction products obtained from the interaction of incident neutrons with the detector material determines the number of e–h pairs that can be excited [18], [24]. This energy should be high enough (at least a few MeV) such that the number of e–h pairs excited can contribute to an electrical signal higher than the noise level.

The charge transport properties, including charge carrier mobility, lifetime, and mobility–lifetime product, are of fundamental importance to the performance of a material as a detector. The charge carrier mobility gives a measure of how fast the excited charge carrier(s) can drift through the material when an electric field is applied; the carrier lifetime is a measure of how long the charge carriers can remain free before being trapped or recombined. These two quantities together (usually referred to as the mobility–lifetime product) determine the drift length and ultimately the detection efficiency of a material [24], [30], [31].

When a material is used as a neutron detector, the leakage current—a steady current due to an external voltage—acts as a major source of noise, which needs to be minimized. Therefore, it is optimal to have a material with a high resistivity [32]. In addition to affecting the leakage current, the resistivity of a material determines the maximum electric field that can be applied across it without causing electrical breakdown. A material with high resistivity can be biased with a higher voltage, which gives higher charge collection efficiency and may lead to a higher signal current [24], [32]. However, in many practical cases, the leakage current is minimized by employing noninjecting contacts, which are materials that do not replenish the charge carriers in the detector material [24].

The electronic structure (such as work function, electron affinity, and relative positions of valence and conduction bands) of a detector material helps to understand the physics of the metal–semiconductor interface and interpret the detector operation [32].

In summary, there are only a few materials that contain isotopes with relatively high neutron cross-sections that can give off moderate-to-high-energy primary reaction products. In order to consider those materials for direct-conversion neutron detection, we must understand their charge transport properties, particularly their charge carrier mobility, lifetime, and/or mobility–lifetime product. An additional requirement is that these materials have a high resistivity. It is either hard to find materials that fulfill all of these requirements simultaneously or we do not have an adequate understanding of their charge transport properties to begin with.

1.4. Uranium Oxide Semiconductors for Neutron Detection

The concept of using uranium oxide semiconductors for solid-state direct-conversion neutron detection is based on the fission of the uranium nucleus. Neutron-induced fission of a uranium nucleus gives primary reaction products with energy in excess of 165 MeV. Such high-energy charged particles can excite a large number of e–h pairs in the detector, which enables a lower level discriminator (LLD) setting well above the energy deposited by any background radiation. Here, LLD refers to the value that must be reached by the signal to be recorded as a “neutron count”. In any detector system, the LLD is set in such a way that any unwanted signal is minimized, and ideally avoided.

A uranium-based semiconductor neutron detector, if achieved in practice, could be used for both thermal and fast neutron detection. Since ^{235}U has a high fission cross-section for thermal neutrons, a detector based on this isotope (for example, uranium enriched with ^{235}U) will be suitable for thermal neutron detection. Similarly, since the fission cross-sections of both ^{235}U and ^{238}U are high for fast neutrons (^{235}U has the highest fission cross-section of all isotopes except gadolinium for neutron energy >10 MeV; Figure 3), neutron detectors based on either of these isotopes are particularly well-suited for fast neutron detection.

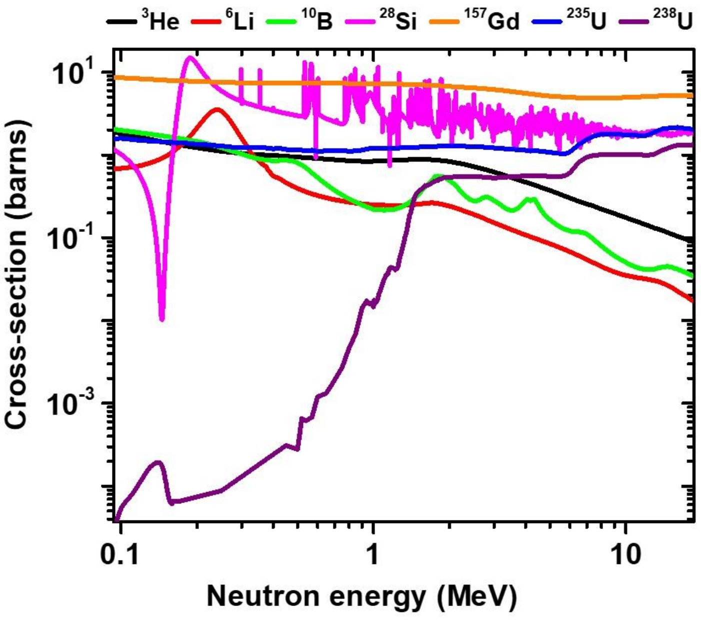

Figure 3. Fast neutron cross-section of nuclei that produce moderate-to-high-energy charged particles for the reactions given in Table 1.

Uranium oxides are the most common forms of uranium. There are several stable and metastable oxides of uranium, which include UO_2, U_4O_9, $U_{16}O_{37}$, U_3O_7, U_8O_{19}, U_2O_5, $U_{13}O_{34}$, U_8O_{21}, $U_{11}O_{29}$, U_3O_8, $U_{12}O_{35}$, and UO_3. Of these oxides, only UO_2, U_3O_8, and UO_3 are thermodynamically stable and are known to display a wide variation in stoichiometry [33], [34]. All of these three oxides can be considered for direct-conversion neutron detectors. These oxides are discussed below.

1.4.1. Uranium Dioxide (UO_2)

Uranium exists in various oxidation states in its oxides due to its unfilled 5*f* orbital: the oxidation states are U^{2+} in uranium monoxide (UO), U^{4+} in uranium dioxide (UO_2), U^{5+} in diuranium pentoxide (U_2O_5), and U^{6+} in uranium trioxide (UO_3). UO_2 is one of the most commonly found oxides of uranium along with U_3O_8.

UO_2 has been reported to be a semiconductor with an intrinsic resistivity value on the order of 10^2–10^3 Ω-cm [35]–[41] and charge carrier mobility value on the order of 10^{-3}–10^{-2} $cm^2 \cdot V^{-1} \cdot s^{-1}$ [42], [43]. Various studies have been performed on the correlation between electrical properties and stoichiometry of UO_2, with some reporting the intrinsic UO_2 to be a *p*-type semiconductor and the hypostoichiometric UO_2 to be an *n*-type semiconductor [38], [42], [43]. Some studies have demonstrated that the resistivity of UO_2 increases with increasing oxygen content (hyperstoichiometric UO_2) until the formation of a two-phase solid UO_{2+x}+U_4O_{9-y}; the resistivity is found to increase by almost two orders-of-magnitude at the $UO_{2.13}$–$UO_{2.16}$ phase boundary. It has been reported that at this phase transition, UO_{2+x} transitions from a *p*-type metal-deficit semiconductor to an *n*-type metal-excess semiconductor [36], [42]. Similarly, the resistivity of UO_2 has been found to increase by about two orders-of-magnitude with decreasing oxygen content (hypostoichiometric UO_2) [44]. While no explicit studies have been performed to specifically understand the influence of grain size, collective data from previous research suggest that the microstructure can have an even greater impact on the resistivity of UO_2 [45]–[48]. These data suggest that a three order-of-magnitude increase in electrical resistivity can be achieved by reducing the average grain size from $\sim 100\ \mu m$ to less than $10\ \mu m$ [49]. Additionally, it has been found that the resistivity of UO_2 can be increased to 10^5–10^6 Ω-cm by doping with Nb_2O_5 [50], [51].

1.4.2. Triuranium Octoxide (U_3O_8)

Uranium exists in a mixed oxidation state of U^{5+} and U^{6+} in U_3O_8. There are three polymorphs—*α*-, *β*-, and *γ*-U_3O_8—with well-defined structures reported in the literature [33], [52]–[55].

U_3O_8 is naturally occurring as a further oxidized component of the mineral form of UO_2, since the latter gradually converts to the former at ambient temperature [53]. It is chemically stable in ambient conditions and is one of the preferred forms of disposal of post-uranium-enrichment waste after conversion from uranium hexafluoride (UF_6). It can also be produced easily by heating uranyl oxide (UO_3), generated during the mining and refinement of uranium oxides.

The importance of U_3O_8 to the nuclear fuel cycle and its chemical and thermodynamic stability have led to a number of investigations of its crystal structure

[52], [53], [56]–[61], thermodynamics [56], [62]–[64], electrical properties [65]–[69], and electronic structure [53], [56], [70]. The electrical resistivity of U_3O_8 has been reported in the range of 10^3–10^5 Ω-cm [66] and its charge carrier mobility has been reported on the order of 1 $cm^2 \cdot V^{-1} \cdot s^{-1}$ [65], [67]. These transport properties, slightly better than those of UO_2 from a semiconductor radiation detector viewpoint, make U_3O_8 a potential candidate material for neutron detection.

1.4.3. Uranium Trioxide (UO_3)

UO_3 is the end point of the uranium–oxygen system in which uranium exists in an oxidation state of U^{6+} ($5f^0$ configuration) with all the valence electrons removed. The U^{6+} ion displays a variety of coordination environments with oxygen to form seven crystalline modifications, α-, β-, γ-, δ-, ε-, ζ-, η-, and an amorphous variant; out of these, γ-UO_3 is the most thermodynamically stable phase [33], [66], [71]–[73]. Since the U^{6+} ion is the soluble form of uranium, UO_3 compounds form hydration products under ambient conditions. Additionally, UO_3 compounds tend to exist as a combination of multiple phases. So, obtaining a stoichiometric crystal with no hydration products is very challenging [34], [74]–[76]. Some common hydrates of UO_3 are listed in Table 2.

UO_3 has been studied in the past, primarily as a major component of the nuclear fuel cycle [77]. While there have been numerous studies to understand the structure and phase of UO_3 [71], [78]–[83], and the complexity of its polymorphs and its hydrates [74], [75], [84], there have been very few attempts to understand its electrical properties [66], [85], and electronic structure (e.g., band structure) [70], [86]. The resistivity of UO_3 is reported to be on the order of 10^7–10^9 Ω-cm and its band gap is reported to be 2.1–2.6 eV. Despite the complex nature of the material and potential complications in fabricating samples, UO_3 could become a very good candidate for direct-conversion solid-state neutron detection from a charge transport point of view.

Table 2. The chemical composition of some common hydrates of UO_3.

Mineral	**Chemical Formula**	**Composition**
Ianthinite*	$(UO_2)\cdot5(UO_3)\cdot10(H_2O)$	94.07% UO_3 and 5.93% H_2O 88.81% UO_2 and 11.19% H_2O
Schoepite	$(UO_2)_8O_2(OH)_{12}\cdot12(H_2O)$ $U_2O_5(OH)_2\cdot3(H_2O)$	82.69% UO_3 and 12.41% H_2O
Metaschoepite	$(UO_2)_4O(OH)_6\cdot5(H_2O)$	91.37% UO_3 and 8.63% H_2O
Paraschoepite	$UO_3\cdot2H_2O$	88.81% UO_3 and 11.19% H_2O

* Composition varies due to polyvalent uranyl hydroxide.

1.5. Summary

There are several drawbacks and limitations of traditional ^{3}He-based neutron detectors, such as the need for dangerously high voltage, their large size making portable devices inconvenient, as well as the imminent shortage and rising price of ^{3}He. This has persuaded the scientific community to search for alternatives such as direct-conversion solid-state neutron detectors, which offer advantages such as low-cost production, low operational power, small size (portability), and high efficiency. Despite these potential benefits, direct-conversion solid-state neutron detectors have not been achieved in practice for two reasons: (1) there exist a limited number of materials that can serve the purpose, (2) there is an insufficient understanding of the transport properties as well as a lack of mature fabrication technology of such materials.

The goal of this research is to evaluate the efficacy of uranium oxides as candidate materials for direct-conversion solid-state neutron detection. A neutron can induce fission of a uranium nucleus, releasing fission fragments with more than 165 MeV of energy. These fragments excite a large number of e–h pairs, which can be detected as electrical signals in a detector configuration. Since the energy obtained from the fission products is extremely large compared to other nuclear reactions used for neutron detection purposes, it could possibly open a path towards developing a solid-state neutron detector with an excellent discrimination of background radiation and/or noise.

This study has been divided into three major parts: (1) modeling uranium oxides (UO_2, U_3O_8, and UO_3) as neutron detectors to evaluate their potential detection efficiency and the required range of charge transport properties for achieving detection, (2) fabricating pellets of U_3O_8 and UO_3 and studying their basic physical/chemical properties, and (3) studying the charge transport properties of these U_3O_8 and UO_3 samples to determine the range of properties that can be achieved by varying the fabrication conditions, and a potential path toward optimization.

1.6. Outline of Dissertation

The remainder of this dissertation is organized as follows. In CHAPTER 2, we describe the fundamental concepts pertaining to a solid-state direct-conversion neutron detector and use these concepts to estimate the charge transport properties required for uranium oxide neutron detectors as well as estimate their potential detection efficiency. In CHAPTER 3, we discuss the theory and experiments used to fabricate and characterize U_3O_8 and UO_3 pellets. In CHAPTER 4, we discuss the results of our measurements of the basic properties (density, microstructure, and phase), resistivity, and charge carrier mobility of stoichiometric and non-stoichiometric U_3O_8 pellets. Likewise, in CHAPTER 5, we discuss the results of our measurements of the basic properties (density, microstructure, phase, and stoichiometry), resistivity, band gap, charge carrier mobility, and mobility–lifetime of UO_3 pellets. The conclusion of this dissertation and possible future work are presented in CHAPTER 6.

CHAPTER 2. THEORY AND MODELING

Towards the goal of developing uranium oxide-based direct-conversion solid-state neutron detectors, we lay out some evaluations of potential detector efficiency. A direct-conversion solid-state neutron detector consists of a detector material sandwiched between two metal electrodes. Once the electron–hole (e–h) pairs are excited in the detector following a neutron absorption event, one or both types of charge carriers are swept towards the appropriate electrodes by an external electric field, which constitutes a signal current. We will start from the charge excited in the detector in the event of interaction with a neutron and obtain an expression for current induced at the electrodes. We will then find the charge collected within a certain integration time followed by obtaining an expression for charge collection efficiency. The expression up to this point holds true for a direct-conversion neutron detector made from any material. We will then apply these expressions to the special case of uranium oxide semiconductors and explore the potential efficiency of neutron detectors fabricated from oxides of different uranium isotopes (^{238}U, ^{235}U, depleted U, natural U, and U enriched with ^{235}U).We will assume that only the majority charge carriers are mobile. This applies to materials in which the mobility of the majority charge carriers is much higher than that of the minority charge carriers, which is the case for a majority of semiconductors—we believe also the uranium oxides.

2.1. Efficiency of a Direct-Conversion Solid-State Neutron Detector

A neutron interacts with a nucleus in a detector to produce energetic reaction product particles, which deposit their energy within the detection medium, exciting many e–h pairs. If U is the energy deposited by the product particles and E_{eh} is the energy required to excite an e–h pair in the detector material, the number of excited e–h pairs (n_{eh}) is given as:

$$n_{\mathrm{eh}} = \frac{U}{E_{\mathrm{eh}}} \tag{2.1}$$

where E_{eh} is obtained as [87]:

$$E_{\mathrm{eh}} = \frac{14}{5} E_{\mathrm{g}} + r(\hbar\omega_{\mathrm{R}}) \tag{2.2}$$

Here, E_{g} represents the band gap of the detector material and r is the mean free path for ionizing collisions and photon emission, with $0.5 \leq r \leq 1.0$ eV.

The charge, q, generated as a result of the excited e–h pairs is given as:

$$q = e\, n_{\mathrm{eh}} \tag{2.3}$$

The time required by a charge carrier to traverse the detector, referred to as the transit time (t_{tr}), is given as:

$$t_{\mathrm{tr}} = \frac{d}{v_{\mathrm{d}}} \tag{2.4}$$

where d is the detector thickness and v_{d} is the drift velocity of the charge carrier in the detector material.

The drift velocity of a charge carrier depends on its mobility (μ) in a material as well as the electric field (E) applied across it. Mathematically, this is expressed as:

$$v_{\mathrm{d}} = \mu E \tag{2.5}$$

Using Equation (2.5) in Equation (2.4), we get:

$$t_{\mathrm{tr}} = \frac{d}{\mu E} \tag{2.6}$$

As soon as the excited charge carriers move inside the detector material, a current (i_0) is induced at its electrodes (equivalently, in the external circuit), which is given by the Shockley–Ramo theorem [30], [31] as:

$$i_0 = \frac{q\mu E}{d} \tag{2.7}$$

Due to the finite lifetime, τ, of free charge carriers, the current decays exponentially with time; the instantaneous current, $i(t)$, is given as:

$$i(t) = i_0 \exp\left(-\frac{\mathrm{t}}{\mathrm{\tau}}\right) \tag{2.8}$$

The total charge collected, q_{col}, in the external circuit is obtained by integrating the current over a certain integration time (t). Mathematically, this is expressed as:

$$q_{\mathrm{col}} = \frac{q\mu E}{d} \int_0^t \exp\left(-\frac{t}{\tau}\right) \mathrm{d}t \tag{2.9}$$

Assuming that the incident neutron is absorbed at x on a detector of thickness d, as shown in Figure 4, and the electric field is applied in such a way that the majority charge carriers move towards the right electrode, the transit time of the charge carriers reaching the right end of the detector is given as:

$$t_{\mathrm{tr}}(x) = \frac{d - x}{\mu E} \tag{2.10}$$

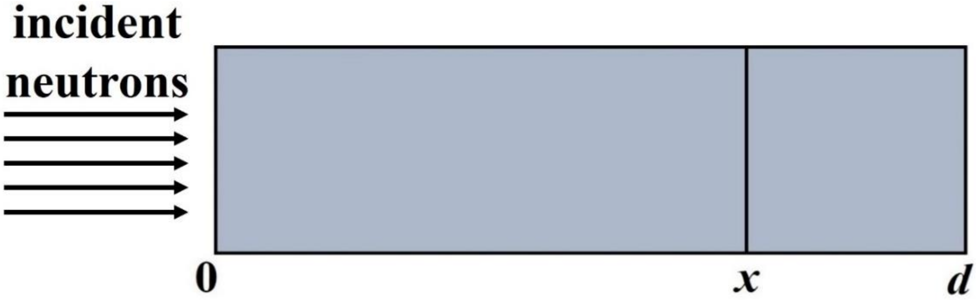

Figure 4. Representation of a detector of thickness *d*; *x* represents a point in the detector at which the incident neutrons are absorbed.

Here we have assumed that the primary reaction products deposit their energy at the same point at which the neutron is absorbed. This is valid if the detector is much thicker than the stopping range of the primary reaction products in the detector material. Keeping the integration time the same as the transit time, Equation (2.9) gives:

$$q_{\mathrm{col}} = \frac{q\mu E}{d}\int_0^{\frac{d-x}{\mu E}} \exp\left(-\frac{t}{\tau}\right)\,\mathrm{d}t \tag{2.11}$$

Carrying out the integration, we have:

$$\frac{q_{\mathrm{col}}}{q} = \frac{\mu\tau E}{d}\left[1-\exp\left(-\frac{d-x}{\mu\tau E}\right)\right] \equiv \mathrm{CCE}(x) \tag{2.12}$$

where CCE(x) is the charge collection efficiency of the detector. It is defined as the ratio of charge collected in the external circuit to the charge excited in the detector.

If we assume a uniform absorption of neutrons (valid for weak absorption), then the CCE is given as:

$$\mathrm{CCE} = \frac{\mu\tau E}{d}\left[1-\frac{\mu\tau E}{d}\left\{1-\exp\left(-\frac{d}{\mu\tau E}\right)\right\}\right] \tag{2.13}$$

Some plots of CCE as a function of different detector parameters are shown in Figure 5. All the plots show a maximum CCE of 50% because we have assumed only one charge carrier type as mobile. For detectors with the same value of charge carrier mobility–lifetime, the CCE depends on the applied electric field per unit thickness of the detector (Figure 5(a), for example). Likewise, for detectors biased with the same electric field, the CCE depends on the ratio $\mu\tau/d$ (Figure 5(b), for example). Similarly, for detectors of the same thickness, the CCE depends on the product $\mu\tau E$ (Figure 5(c), for example). The quantity $\mu\tau E$ has a dimension of length and represents the charge carrier drift length, which is the distance traveled by the charge carrier in the detector before being trapped or recombined. Overall, the CCE of a detector depends on its thickness and the drift length of the charge carriers. When the detector thickness is equal to the drift length of the charge carriers, the CCE equals $1/e$, i.e., the charge collected is ~37% of the charge excited by the incident radiation (Figure 5(d), for example). In order to achieve a higher CCE, it is necessary to have either a sufficiently thin detector or one with sufficiently high charge carrier mobility–lifetime, that can also be biased with a sufficiently high electric field without causing electrical breakdown. However, from a neutron detection point of view, it is not necessary to achieve maximum CCE, but rather a high enough CCE to overcome a lower level discriminator (LLD) setting, as discussed in **Section 1.4**.

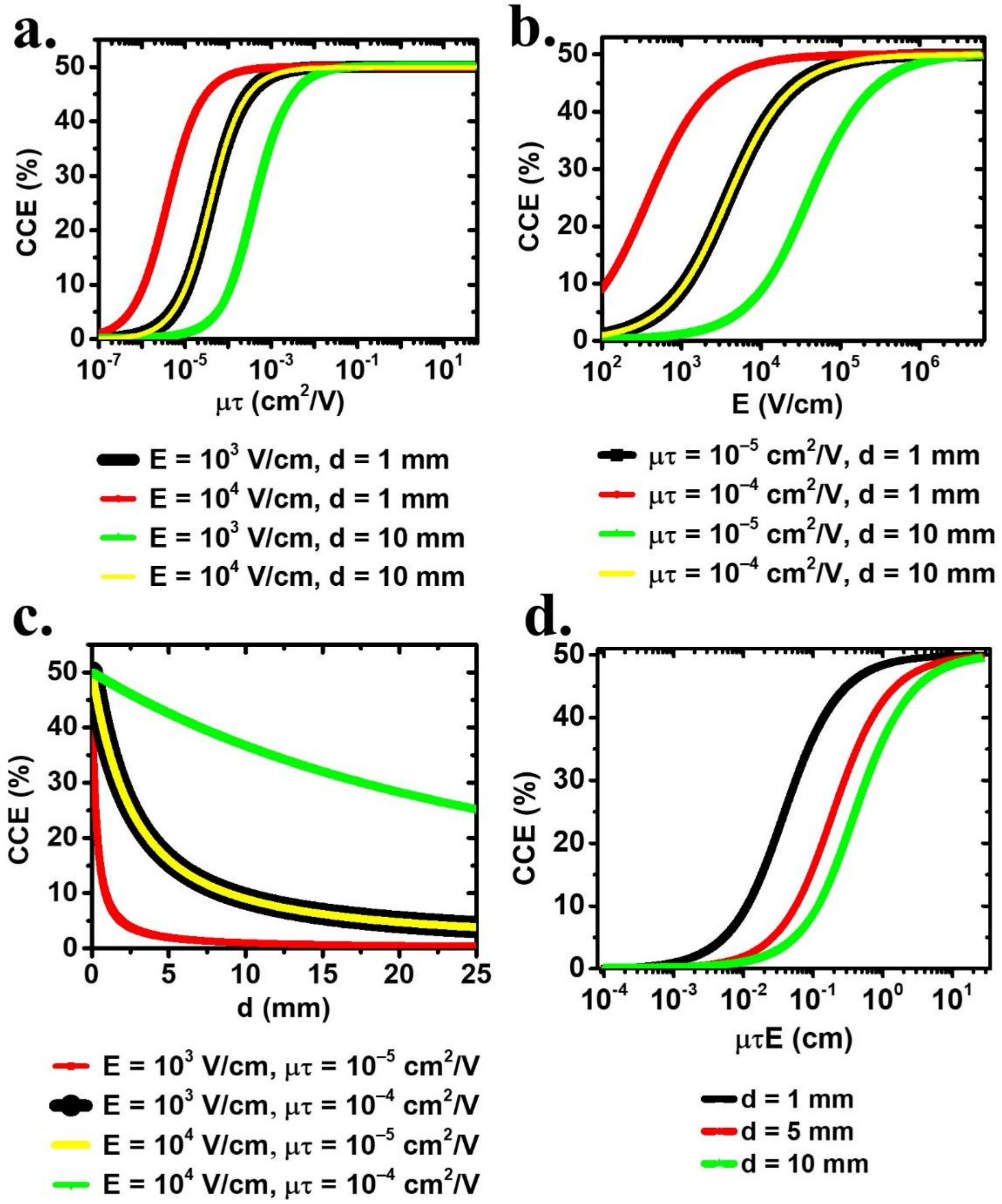

Figure 5. Analysis of CCE for different detector configurations: (a) CCE vs $\mu\tau$ for different detector thicknesses and electric fields; (b) CCE vs electric field for different detector thicknesses and $\mu\tau$ values; (c) CCE vs detector thickness for different electric fields and $\mu\tau$ values; (d) CCE vs charge carrier drift length ($\mu\tau E$) for different detector thicknesses.

In Figure 6, let us assume that the boundary at x on the detector separates two regions: all of the neutrons absorbed to the left of this boundary are detected, whereas all of those absorbed to the right are not because the drift length of the excited charge carriers is too small, i.e., a very small signal below the LLD is generated. In that case, the signal generated by charge carriers excited at x should at least be equal to the minimum CCE ($\mathrm{CCE}_{\mathrm{min}}$), as discussed above. Then, for $\mathrm{CCE}_{\mathrm{min}}$, the expression for x can be written from Equation (2.12) as:

$$x = \mu\tau E \ln\left(1 - \frac{d}{\mu\tau E}\mathrm{CCE}_{\mathrm{min}}\right) + d \tag{2.14}$$

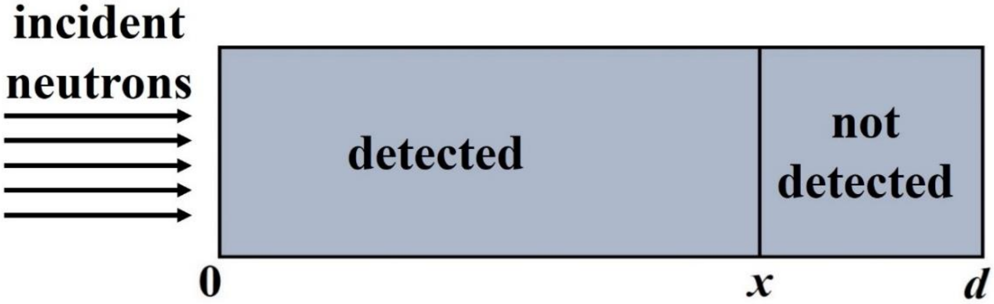

Figure 6. Representation of a detector of thickness d with x as a boundary that separates two regions in the detector: all of the neutrons absorbed to the left are detected while all of those absorbed to the right are not.

Assuming N_0 neutrons are incident on a detector, the total number of neutrons absorbed (N_{abs}) within the thickness x of the detector is given as:

$$N_{\mathrm{abs}} = N_0[1 - \exp(-\Sigma x)] \tag{2.15}$$

The intrinsic detection efficiency (η)—sometimes referred to as simply detection efficiency—of a neutron detector, which is defined as the number of neutrons detected (equal to neutrons absorbed for our case) per incident neutron, is given as:

$$\eta = \frac{N_{\text{abs}}}{N_0} = 1 - \exp(-\Sigma x) \qquad (2.16)$$

Substituting for *x* from Equation (2.14) in Equation (2.16), we get:

$$\eta = 1 - \left(1 - \frac{d}{\mu\tau E}\text{CCE}_{\text{min}}\right)^{-\Sigma\mu\tau E} \exp(-\Sigma d) \qquad (2.17)$$

As seen from Equation (2.17), the intrinsic neutron detection efficiency of a detector depends upon its thickness, macroscopic cross-section area, and charge carrier drift length as well as the minimum CCE required to detect a signal.

The result of setting a minimum CCE (effectively setting the lower level discriminator) is that the detection probability will decrease from 100% proportionately. An example is shown in Figure 7, which shows the detection probability per absorbed neutron of a UO_3 detector as a function of $\mu\tau$; the detector thickness is assumed to be 1 cm and the electric field 1000 V·cm^{-1}. As seen from the figure, if CCE_{min} is set at 1%, the detection probability is close to 100%, whereas it plateaus at ~90% and ~75% for CCE_{min} of 10% and 25%, respectively.

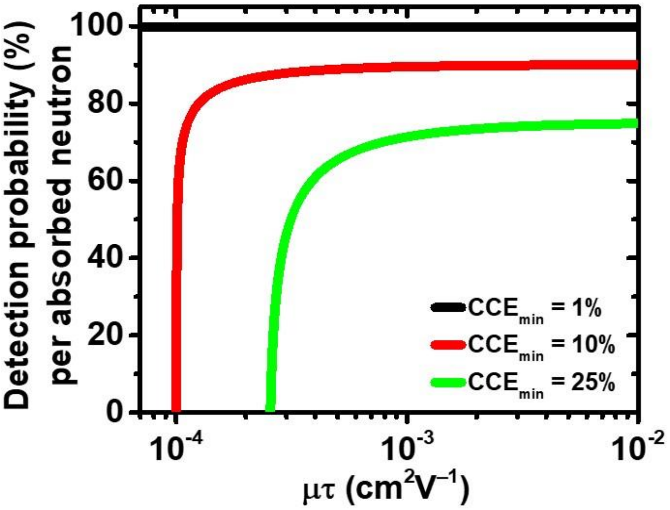

Figure 7. Detection probability per absorbed neutron of a UO_3 detector as a function of charge carrier $\mu\tau$ for 10 MeV neutrons when the minimum charge collection efficiency is set to 1, 10, and 25%. Here we have considered a detector thickness of 1 cm with an electric field set at 1000 V·cm^{-1}.

2.2. Neutron Absorption Probability of Uranium Oxide

We will consider the interaction of uranium nuclei with thermal (energy ∼25 meV) and fast (1 and 10 MeV) neutrons. The fission cross-sections of both ^{238}U and ^{235}U for thermal and fast neutrons are summarized in Table 3; the cross-sections as functions of neutron energies are shown in Figure 1 and Figure 3.

To evaluate the detection efficiency of uranium oxide detectors, we will consider different oxides of various uranium isotopic combinations: ^{238}U, depleted U (99.7% of ^{238}U and 0.3% of ^{235}U), natural U (99.275% of ^{238}U and 0.725% of ^{235}U), 5% enriched U (95% of ^{238}U and 5% of ^{235}U), and ^{235}U. The macroscopic cross-sections (Σ) and mean penetration depths (λ) of thermal and fast neutrons for different oxides of uranium are summarized in Table 4. The probabilities of absorption of thermal and fast neutrons by uranium oxide detectors with thicknesses of 1 and 10 mm are given in Table 5. As seen from Table 4, the absorption probability of neutrons of a certain energy (whether thermal or fast) is higher for ^{235}U-based oxides and lower for ^{238}U-based oxides for detectors of the same thickness (also represented in Figure 8(a), for example). Consequently, the mean penetration depth decreases with increasing ^{235}U content (i.e., more neutrons are absorbed within a smaller distance).

Table 3. Fission cross-sections of ^{238}U and ^{235}U for thermal and fast neutrons. Data taken from [23].

Neutron energy	**Fission cross-section (barns)**	
	^{235}U	**^{238}U**
25 meV	582	1.8×10^{-5}
1 MeV	1.2	10^{-2}
10 MeV	1.7	1

For 10 MeV neutrons, the macroscopic cross-sections are similar for oxides of ^{238}U, depleted U, natural U, and low-enriched U, and slightly higher for ^{235}U. Consequently, the absorption probability values also follow the same pattern (Table 5). The absorption probability values of a 1 cm thick detector are 1.6–2.5% for oxides of ^{238}U, depleted U, natural U, and low-enriched U, and 2.8–4% for oxide of ^{235}U. Therefore,

a detector for 10 MeV neutrons could be made from any of the oxides, however, the detection efficiency will be low in all cases.

For 1 MeV neutrons, only the oxides of ^{235}U show reasonable macroscopic cross-sections, and these are at least an order-of-magnitude higher than for the other isotopic compositions (Table 4). The absorption probability values of oxides of ^{235}U are 2–3% for detectors of thickness 1 cm, as seen from Table 5. Therefore, only the oxides of ^{235}U could be useful for detecting 1 MeV neutrons, however, the detection efficiency would still remain low due to the low absorption probability.

For thermal neutrons, since the microscopic cross-sections of ^{238}U and ^{235}U differ significantly (seven orders-of-magnitude, Table 3), even a small quantity of ^{235}U (e.g., 0.3% in depleted uranium) increases the macroscopic cross-section of uranium oxides appreciably (Table 4). As seen from Table 5, the absorption probabilities of a 1 mm thick detector are ∼1% for oxides of natural U, ∼5% for oxides of low-enriched U, and 62–76% for oxides of ^{235}U, whereas those of a 1 cm thick detector are ∼3% for oxides of depleted U, ∼7% for oxides of natural U, 38–51% for oxides of low-enriched U, and 100% for oxides of ^{235}U. Therefore, thermal neutron detection is conceivable using a depleted uranium oxide, however the detection efficiency would be higher for oxides of natural and enriched U.

Overall, the detectors would need to be thick: (1) thickness on the order of centimeters for fast neutrons, if a few percentages of absorption probability is desired (thickness on the order of millimeters would give less than a percent of absorption probability); (2) thickness on the order of millimeters for thermal neutrons, if a few percentages of absorption probability is desired. If lower absorption probabilities (and ultimately lower detection efficiencies) are acceptable, for example in high flux environments, thinner detectors would work. It should be noted that since uranium is the isotope that interacts with incident neutrons, the absorption probability decreases with O/U ratio in these oxides, i.e., for fixed neutron energy and detector thickness, UO_2 detectors have the highest absorption probability whereas UO_3 detectors have the lowest probability. An example of variation of absorption probability among oxides of natural uranium is shown in Figure 8(b).

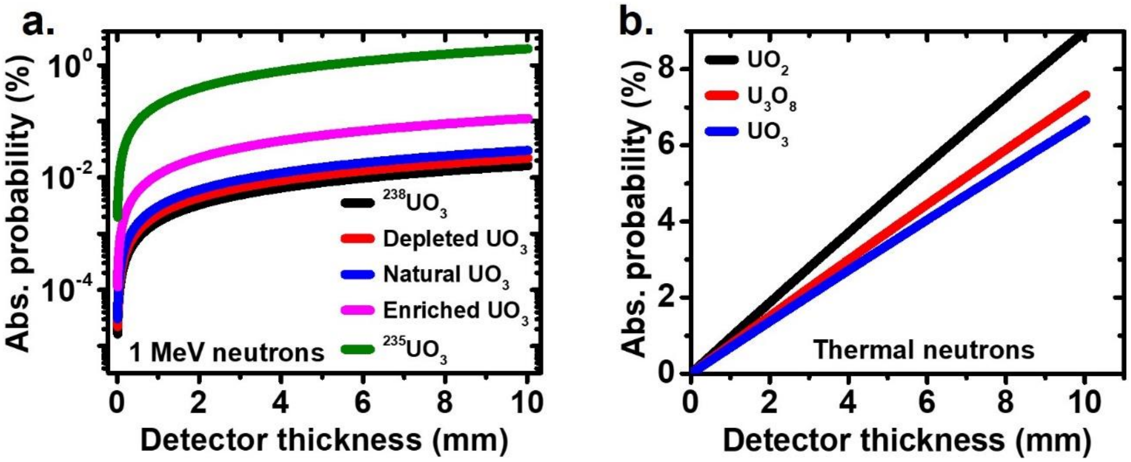

Figure 8. Absorption probability as a function of detector thickness: (a) of 1 MeV neutrons for UO_3 detectors with different ^{235}U content (b) of thermal neutrons for detectors based on different O/U ratios.

Table 4. Macroscopic cross-section (*Σ*) and mean penetration depth (*λ*) of thermal and fast neutrons for different uranium oxides.

Isotope	**Oxide**	**25 meV neutron**		**1 MeV neutron**		**10 MeV neutron**	
		Σ (cm^{-1})	**λ (cm)**	**Σ (cm^{-1})**	**λ (cm)**	**Σ (cm^{-1})**	**λ (cm)**
^{238}U	UO_2	4.4×10^{-7}	2.3×10^{6}	2.4×10^{-4}	4.1×10^{3}	2.4×10^{-2}	41
	U_3O_8	3.2×10^{-7}	3.1×10^{6}	1.8×10^{-4}	5.6×10^{3}	1.8×10^{-2}	56
	UO_3	2.9×10^{-7}	3.4×10^{6}	1.6×10^{-4}	6.1×10^{3}	1.6×10^{-2}	61
Depleted U (0.3% ^{235}U)	UO_2	4.3×10^{-2}	23	3.3×10^{-4}	3.0×10^{3}	2.4×10^{-2}	41
	U_3O_8	3.1×10^{-2}	32	2.4×10^{-4}	4.1×10^{3}	1.8×10^{-2}	56
	UO_3	2.8×10^{-2}	35	2.2×10^{-4}	4.5×10^{3}	1.6×10^{-2}	61
Natural U (0.725% ^{235}U)	UO_2	9.4×10^{-2}	11	4.5×10^{-4}	2.2×10^{3}	2.5×10^{-2}	41
	U_3O_8	7.6×10^{-2}	13	3.3×10^{-4}	2.9×10^{3}	1.8×10^{-2}	55
	UO_3	6.9×10^{-2}	14	3.0×10^{-4}	3.3×10^{3}	1.6×10^{-2}	61
5% enriched U	UO_2	7.1×10^{-1}	1.4	1.7×10^{-3}	5.9×10^{2}	2.5×10^{-2}	39
	U_3O_8	5.2×10^{-1}	1.9	1.2×10^{-3}	8.0×10^{2}	1.9×10^{-2}	54
	UO_3	4.7×10^{-1}	2.1	1.1×10^{-3}	8.8×10^{2}	1.7×10^{-2}	59
^{235}U	UO_2	14	6.9×10^{-2}	2.9×10^{-2}	34	4.2×10^{-2}	24
	U_3O_8	11	9.4×10^{-2}	2.2×10^{-2}	46	3.1×10^{-2}	33
	UO_3	9.6	1.0×10^{-1}	1.9×10^{-2}	51	2.8×10^{-2}	36

Table 5. Absorption probability of thermal and fast neutrons of different uranium oxide detectors 1 and 10 mm thick.

Isotope	**Oxide**	**Absorption probability (%)**					
		1 mm thick detector			**10 mm thick detector**		
		25 meV neutrons	**1 MeV neutrons**	**10 MeV neutrons**	**25 meV neutrons**	**1 MeV neutrons**	**10 MeV neutrons**
^{238}U	UO_2	4.4×10^{-6}	2.4×10^{-3}	0.24	4.4×10^{-5}	2.4×10^{-2}	2.4
	U_3O_8	3.2×10^{-6}	1.8×10^{-3}	0.18	3.2×10^{-5}	1.8×10^{-2}	1.8
	UO_3	2.9×10^{-6}	1.6×10^{-3}	0.16	2.9×10^{-5}	1.6×10^{-2}	1.6
Depleted U (0.3% ^{235}U)	UO_2	0.43	3.3×10^{-3}	0.25	4.2	3.3×10^{-2}	2.4
	U_3O_8	0.31	2.4×10^{-3}	0.18	3.1	2.4×10^{-2}	1.8
	UO_3	0.28	2.2×10^{-4}	0.16	2.8	2.2×10^{-2}	1.6
Natural U (0.725% ^{235}U)	UO_2	0.94	4.6×10^{-3}	0.24	9.0	4.6×10^{-2}	2.4
	U_3O_8	0.76	3.6×10^{-3}	0.18	7.3	3.6×10^{-2}	1.8
	UO_3	0.69	3.0×10^{-3}	0.16	6.6	3.0×10^{-2}	1.6
5% enriched U	UO_2	6.9	1.7×10^{-2}	0.25	51	0.17	2.5
	U_3O_8	5.1	1.2×10^{-2}	0.19	41	0.12	1.8
	UO_3	4.6	1.1×10^{-2}	0.17	38	0.11	1.7
^{235}U	UO_2	76	0.29	0.42	100	2.9	4.1
	U_3O_8	65	0.22	0.31	100	2.2	3.0
	UO_3	62	0.19	0.28	100	1.9	2.8

2.3. Charge Excitation in Uranium Oxide Detectors

Equations (2.1), (2.2), and (2.3) can be used to calculate the charge excited in each uranium oxide detector if we know their band gap. For U_3O_8, taking the band gap as 2.4 eV [70] and using Equation (2.2), the energy required to excite an e–h pair is ∼6.8 eV. Since the energy of the fission fragments is around 165 MeV, the total number of e–h pairs excited in U_3O_8, as given by Equation (2.1), is $\sim 2.4\times 10^7$. Using Equation (2.3), this is equivalent to a charge of 3.9 pC. Similar calculations give a total excited charge of 4.5 pC for both UO_2 and UO_3 detectors, assuming band gaps of ∼2 eV [70], [86].

2.4. Leakage Current: Effect of α-Particle Decay

In order for neutron detection to occur, the charge collection efficiency does not need to be 100%, but should be (at least) above the lower-level discriminator (discussed in **Section 1.4**). There are various factors that can give rise to leakage current or false signal in uranium oxide detectors, which include γ-rays (external, intrinsic, or fission-related), neutrons produced due to fission (spontaneous or neutron-induced), and α-particles due to radioactive decay of uranium.

The fission of uranium by γ-rays (also known as photo-fission) could lead to an unwanted or a false signal, since the signal obtained due to the process would be indistinguishable from that obtained due to neutron-induced fission [20]. The fission cross-sections of ^{238}U and ^{235}U as a function of γ-ray energy are shown in Figure 9. We see from Figure 3 and Figure 9 that the fission cross-section of each uranium isotope for γ-rays with energy above 5.5 MeV is comparable to that of ^{238}U for neutrons above 1

MeV energy. Therefore, the photo-fission of uranium will be a major concern only for γ-rays with energy in excess of 5.5 MeV. Let us look at the scenario for each of background, internal, and fission-related γ-rays. The typical background radiation is caused by isotopes such as potassium, sodium, thorium, bismuth, and uranium. Their radiation spectra consist of γ-rays with mostly ≤ 3 MeV energy [88]–[93]. This is also true of γ-rays emitted from uranium nuclei and their decay products [94]–[96]. The γ-rays emitted due to fission (whether spontaneous or induced) consist significantly of photons with energy less than 5.5 MeV [97]–[101]. Overall, considering such a small presence of γ-rays of higher energy (≥ 5.5 MeV) combined with such a small fission cross-section (a maximum of $\sim$0.3 barn for 13 MeV γ-rays), there is an extremely small chance of obtaining a false signal due to photo-fission of uranium.

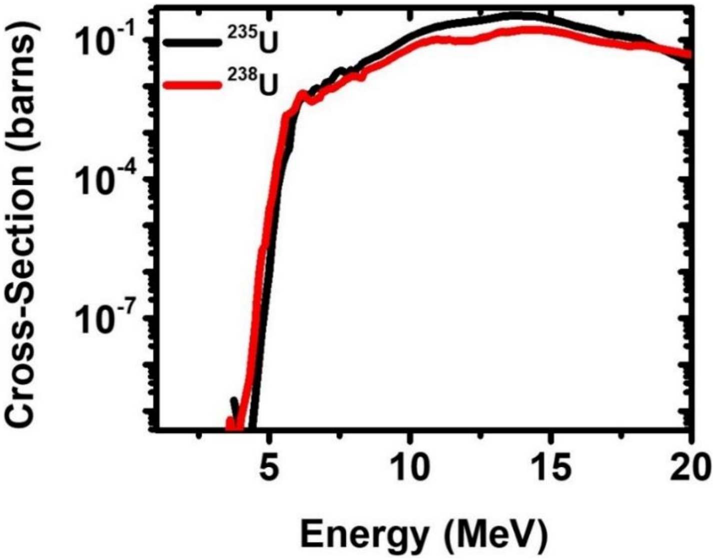

Figure 9. Photo-fission cross-section of ^{238}U and ^{235}U as a function of γ-ray energy. Data taken from [23].

The neutrons produced due to neutron-induced fission of a uranium nucleus can cause fission of additional nuclei, that is, “secondary fission”, giving rise to an unwanted signal. The chances of secondary fission depend on the energy of the fission neutrons as well as the amount and isotope of uranium present in a detector. For example, Kruschwitz *et al.* [20] have reported less than 1% of secondary fissions in a UO_2 detector that contained about 2 grams (0.5 inch in diameter, 1/16 of an inch thick) of depleted uranium. The neutrons produced due to spontaneous fission could also induce another fission, giving rise to an unwanted signal. Neutrons are released at the rate of 3.0×10^{-4} and 1.4×10^{-2} per gram per second due to spontaneous fission from ^{235}U and ^{238}U respectively [102]. Therefore, the total neutron emission rate in a uranium oxide detector depends on the mass and isotope of uranium within the detector. For example, assuming that a detector contains a maximum of 10 g of uranium (UO_2 detector with a cross-sectional area of 1 cm^2 and thickness of 1 cm), the neutron emission rate would be about 1 neutron every 5.5 minutes and 1 neutron every 7 seconds for ^{235}U and ^{238}U respectively. The fission neutrons could have energy anywhere from nearly zero to about 10 MeV with a most likely value of 0.7 MeV [103]. All of these neutrons are capable of inducing fission in uranium, however, not all neutrons cause fission, since the probability will be low due to a small fission cross-section (**Section 2.2**). Therefore, there is a small possibility that a false signal will be obtained due to fission caused by spontaneous fission neutrons.

An important source of noise in these detectors will be the leakage current originating from the intrinsic α-decay of uranium. The α-activity of a material depends on the number of nuclei within it, which in turn depends on the mass of the material, where mass is a function of density and volume. Therefore, the α-activity of a material depends on its volume, i.e., its cross-sectional area and thickness.

Every α-particle excites e–h pairs in the detector, in the same manner as fission fragments excite e–h pairs. Therefore, the charge collected in the external circuit due to each neutron absorption event must exceed that due to α-particles for neutron detection to occur. Overall, we need to take into account both the detector volume and integration time to evaluate the effect of α-decay in these detectors. Let us take the case of ^{238}U, for example, in a $^{238}U_3O_8$ detector. The half-life for the α-decay of ^{238}U is 4.47×10^9 years [102], which corresponds to a specific activity of 1.24×10^4 disintegrations per second per gram. Since the density of U_3O_8 is 8.39 $g\cdot cm^{-3}$ [104], the total mass of a 1 cm thick detector with a cross-sectional area of 1 cm^2 (i.e., a detector volume of 1 cm^3) is 8.39 g; the total ^{238}U content is about 7.11 g. This means that the α-activity of ^{238}U in this detector is about 8.85×10^4 disintegrations per second. Assuming an integration time equal to a charge carrier transit time of 1 ms (estimated based on a mobility value of 1 $cm^2\cdot V^{-1}\cdot s^{-1}$ in U_3O_8 and an electric field of 1000 $V\cdot cm^{-1}$), so that the generated charge may be collected, the number of α-particles produced during this time is ~89. Since each α-particle released from ^{238}U has an energy of 4.27 MeV [102], the total energy of α-decay within the integration time is 380 MeV, which can excite a total charge of about 9 pC in the detector, much higher than the charge generated by the fission fragments (discussed in **Section 2.3**). If the integration time is reduced to 0.1 ms, the number of α-particles generated during the integration time is ~9, which can excite a total charge of about 0.9 pC of charge (on the order of nA's of current) in the detector—slightly less than 25% of the charge excited by fission fragments. The charge excited by α-particles scales with the detector thickness if the integration time is kept constant, since the detector volume also scales with the detector thickness. If the integration time is set equal to the transit time, the charge excited by α-particles scales with the square of the detector thickness, since its volume and the transit time of charge carriers (= integration time), both scale with the detector thickness. In the above example, if the detector is 1 mm thick and the integration time is set equal to the transit time, the amount of charge excited by α-particles within the integration time will reduce by a factor of 100, i.e., ~0.1 pC. On the other hand, the charge excited by α-particles scales with the cross-sectional area of the detector. For example, if the cross-sectional area of the detector is halved, the charge excited by the α-particles within the integration time will be halved (i.e., 0.45 pC in this case).

It should be noted that the integration time does not *need* to be set equal to the transit time of the charge carriers. However, shorter integration times will result in less than full charge collection (on the other hand, if the integration time is set larger than the carrier transit time, the “additional time” does not contribute to the signal). One way of getting around this problem is to increase the charge carrier mobility of the detector material, which decreases the transit time and consequently reduces the integration time required for full charge collection and therefore the number of α-particles emitted within the integration time (assuming integration time = transit time).

If α-particles were the only source of leakage current, then the CCE_{min} would depend on the charge excited by α-particles within the integration time. If the integration time is set equal to the transit time of charge carriers, the CCE_{min} therefore depends on the cross-sectional area of the detector (i.e., scales with the cross-sectional area). An example has been presented in Table 6, which shows the charge excited by α-particles within a given integration time, and the corresponding $\mathrm{CCE}_{\mathrm{min}}$ of uranium oxide detectors with two different values of cross-sectional area (1×1 cm^2 and 0.5×0.5 cm^2). If the integration time is chosen arbitrarily (instead of setting equal to charge carrier transit time), the $\mathrm{CCE}_{\mathrm{min}}$ scales by the same factor as the thickness and cross-sectional area of the detector as well as the integration time.

Since the α-activity and the energy of the emitted α-particles both differ according to the uranium content and isotope present in a detector, the minimum CCE will be different for different detectors. Table 7 shows the charge excited by α-particles for potential integration times of 0.01, 0.1 and 1 ms for detectors assumed to be 1 and 10 mm thick, each with a cross-sectional area of 1 cm^2. As seen from the table, the charge excited by α-particles increases with the increase in amount of ^{235}U. This is because the α-particles are emitted at a faster rate and with a higher energy from ^{235}U (4.68 MeV α-particles at 7.99×10^4 per second per gram) than from ^{238}U (4.27 MeV α-particles at 1.24×10^4 per second per gram) [102].

Table 6. Charge excited by α-particles and corresponding CCE$_{min}$ in uranium oxide with different uranium isotopic compositions for detector areas of 1×1 cm^2 and 0.5×0.5 cm^2. Here we have assumed a charge carrier transit time of 0.1 ms.

Isotope	**Oxide**	**Detector area = 1×1 cm^2**		**Detector area = 0.5×0.5 cm^2**	
		Charge excited by α-particles (pC)	**CCE$_{min}$ (%)**	**Charge excited by α-particles (pC)**	**CCE$_{min}$ (%)**
^{238}U	UO_2	1.39	31	0.348	7.8
	U_3O_8	0.893	23	0.223	5.7
	UO_3	0.936	21	0.234	5.2
Depleted U (0.3% ^{235}U)	UO_2	1.42	32	0.355	7.9
	U_3O_8	0.909	23	0.227	5.8
	UO_3	0.949	21	0.237	5.3
Natural U (0.725% ^{235}U)	UO_2	1.46	32	0.365	8.1
	U_3O_8	0.932	24	0.233	6.0
	UO_3	0.976	22	0.244	5.4
5% enriched U	UO_2	1.82	40	0.455	10
	U_3O_8	1.16	30	0.290	7.4
	UO_3	1.22	27	0.305	6.8
^{235}U	UO_2	9.86	219	2.46	55
	U_3O_8	6.28	161	1.57	40
	UO_3	6.57	146	1.64	36

The underlined values in red mean that the charge excited by α-particles is higher than that excited by fission fragments.

Table 7. Charge excited by *α*-particles in uranium oxides for different isotopes in different integration times in detectors of thicknesses of 1 and 10 mm with cross-sectional area of 1 cm^2.

Isotope	**Oxide**	**Charge excited (pC) by *α*-particles in the material**					
		1 mm thick			**10 mm thick**		
		0.01 ms	**0.1 ms**	**1 ms**	**0.01 ms**	**0.1 ms**	**1 ms**
^{238}U	UO_2	0.013	0.13	1.3	0.13	1.3	13
	U_3O_8	8.4×10^{-3}	0.084	0.84	0.084	0.84	8.4
	UO_3	8.9×10^{-3}	0.089	0.89	0.089	0.89	8.9
Depleted U (0.3% ^{235}U)	UO_2	0.014	0.14	1.4	0.14	1.4	14
	U_3O_8	8.5×10^{-3}	0.085	0.85	0.085	0.85	8.5
	UO_3	9.1×10^{-3}	0.091	0.91	0.091	0.91	9.1
Natural U (0.725% ^{235}U)	UO_2	0.014	0.14	1.4	0.14	1.4	14
	U_3O_8	8.7×10^{-3}	0.087	0.87	0.087	0.87	8.7
	UO_3	9.4×10^{-3}	0.094	0.94	0.094	0.94	9.4
5% enriched U	UO_2	0.017	0.17	1.7	0.17	1.7	17
	U_3O_8	0.011	0.11	1.1	0.11	1.1	11
	UO_3	0.012	0.12	1.2	0.12	1.2	12
^{235}U	UO_2	0.095	0.95	9.5	0.95	9.5	95
	U_3O_8	0.059	0.59	5.9	0.59	5.9	59
	UO_3	0.063	0.63	6.3	0.63	6.3	63

The underlined values in red mean that the charge excited by the *α*-particles is greater than that excited by the fission fragments.

2.5. Transport Properties Requirements

Assuming high enough charge collection efficiency and low enough leakage current, an intrinsic detection efficiency of a few percent should be achievable with detectors of thickness 1 mm to 1 cm for specific neutron energies and isotopic compositions. Let us analyze some charge transport properties required for the detectors.

In order to discuss the required charge transport properties, we will assume that the integration time will be set equal to the transit time of the charge carriers. We will consider a detector that has a cross-sectional area of 1 cm^2 and operates at an electric field of 1000 $\mathrm{V \cdot cm^{-1}}$. For a 1 mm thick detector, the transit times of charge carriers (from Equation (2.6)) are 10^{-4} and 10^{-5} s if the charge carrier mobilities are 1 and 10 $\mathrm{cm^2 \cdot V^{-1} \cdot s^{-1}}$ respectively. On the other hand, for a 1 cm thick detector, the transit times of the charge carriers are 10^{-3} and 10^{-4} s for the same mobility values. Based on our initial assumptions, the integration times can be 10^{-3}, 10^{-4}, or 10^{-5} s depending upon detector thickness. However, as seen from Table 7, an integration time of 10^{-3} s for a 1 cm thick detector is not useful because the charge excited by α-particles decay will be greater than that excited by fission fragments. Therefore, in order to have an integration time less than 10^{-3} s, a charge carrier mobility of more than 1 $\mathrm{cm^2 \cdot V^{-1} \cdot s^{-1}}$ would be required.

The requirement of charge carrier lifetime can be analyzed using Equation (2.13) and the minimum value of CCE discussed in **Section 2.4**. The minimum charge carrier lifetime required would depend on the charge carrier mobility and thickness of the detector, the electric field applied, and $\mathrm{CCE_{min}}$. If we assume the same charge carrier mobility, detector thickness and applied electric field, $\mathrm{CCE_{min}}$ will determine carrier lifetime required. For example, if we consider CCE_{min} as 25% and solve Equation (2.13), we get $\mu\tau E/d = 0.39$. Assuming a detector operating under an electric field of 1000 $V \cdot cm^{-1}$, and a minimum charge carrier mobility of 1 $cm^2 \cdot V^{-1} \cdot s^{-1}$, the carrier lifetime is obtained as 3.9×10^{-5} s for a detector of thickness 1 mm. Similarly, the carrier lifetime required would be 1.1×10^{-5} and 2.7×10^{-5} s for CCE_{min} values of 10 and 20% respectively. Overall, a lower lifetime will be sufficient if the CCE_{min} is lower. Similarly, a lower carrier lifetime will be sufficient for a thinner detector, or a detector with high charge carrier mobility, or if a higher electric field can be applied.

The resistivity requirement depends on the detector design. In any detector, the leakage current needs to be smaller than the signal current. The leakage current depends on the cross-sectional area and resistivity of the detector as well as the electric field. A higher electric field will give rise to a higher leakage current. Consequently, a higher resistivity is required to decrease the leakage current. The leakage current can also be decreased by reducing the cross-sectional area of the detector. For example, if we assume a detector with cross-sectional area of 1 cm^2 operating at an electric field of 1000 $V \cdot cm^{-1}$ and use Ohm's law, we find that a resistivity of about 10^{12} Ω-cm is required in order to limit the leakage current to the order of nA (as discussed in **Section 2.4**). If the detector area is halved, the required resistivity will be on the order of 10^{11} Ω-cm. If the detector is configured in a different heterostructure such as a reverse biased diode or a Schottky diode, the resistivity requirement will be relaxed, since a reverse biased diode is mostly non-conducting (until a breakdown is reached).

2.6. Evaluation of Potential Detector Efficiency

It is obvious that the detection efficiency of uranium oxide-based detectors increases with the absorption probability, which depends on the macroscopic cross-section. As a result, the detection efficiency is maximum for the combination of neutron energy and detector material for which the macroscopic cross-section is maximum, assuming other parameters (e.g., $\mu\tau$, $\mathrm{CCE}_{\mathrm{min}}$, d, E) are the same. So, $^{238}UO_3$-based detectors provide the lowest detection efficiency whereas $^{235}UO_2$-based detectors offer the highest detection efficiency for each of 25 meV, 1 MeV, 10 MeV neutrons.

Table 8 shows the potential detection efficiency of UO_2 detectors with a cross-sectional area of 1 cm^2 for different combinations of detector thickness (1 and 10 mm), charge carrier mobility (1 and 10 $\mathrm{cm}^2\cdot\mathrm{V}^{-1}\cdot\mathrm{s}^{-1}$), and electric field ($10^3$ and 10^4 $\mathrm{V}\cdot\mathrm{cm}^{-1}$) corresponding to thermal and fast neutrons. The charge carrier lifetime is assumed to be 10^{-4} s, the integration time is set equal to the transit time of charge carriers in the detector, and the minimum CCE is set to just overcome the charge excited within the integration time by α-particles. It can be seen that the detection efficiency for thermal neutrons is ~1% for a 1 mm thick detector and increases up to ~9% for a 1 cm thick detector if the charge carrier mobility is 10 $\mathrm{cm}^2\cdot\mathrm{V}^{-1}\cdot\mathrm{s}^{-1}$, assuming an applied electric field of 10^3 $\mathrm{V}\cdot\mathrm{cm}^{-1}$. Similarly, the detection efficiency for 1 MeV neutrons is ~4.5×10^{-3} % for a 1 mm thick detector and increases to 3×10^{-2}–4×10^{-2}% for a 1 cm thick detector. Finally, the detection efficiency for 10 MeV neutrons is 0.24% for a 1 mm thick detector, which increases to ~2% for a 1 cm thick detector.

For detectors with the same macroscopic cross-section and the same applied electric field, a thinner detector can detect even for a lower value of $\mu\tau$; however, a thicker detector can offer a higher detection efficiency if a sufficiently high $\mu\tau$ can be achieved (Figure 10(a), for example). Similarly, for detectors with the same microscopic cross-section and the same thickness, a higher electric field should be applied to achieve a detection if $\mu\tau$ is lower; however, once sufficiently high $\mu\tau$ is achieved, there is a very small difference in the detection efficiency (Figure 10(b), for example).

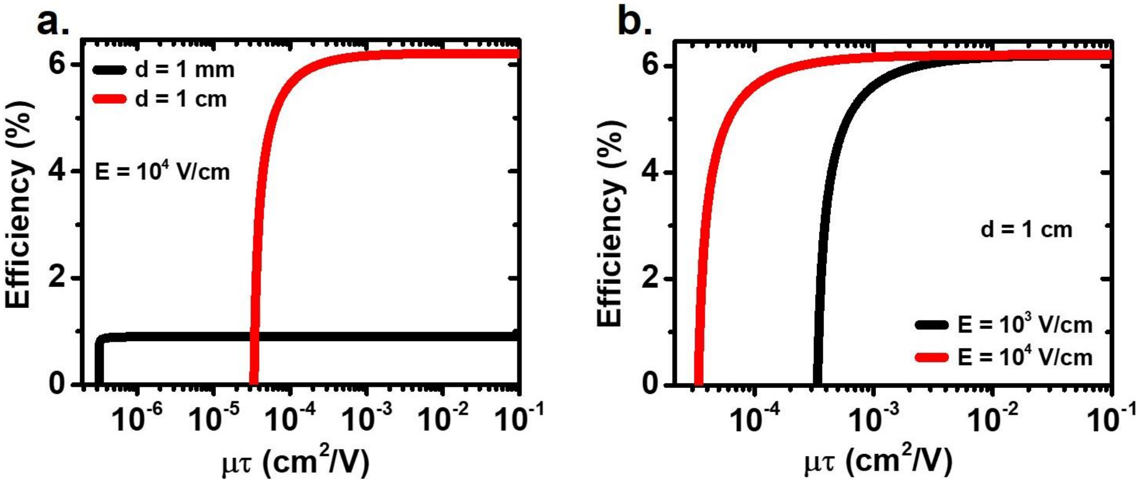

Figure 10. Detection efficiency as a function of charge carrier $\mu\tau$ of natural UO_2 detectors for thermal neutrons: (a) electric field of 10^4 V·cm^{-1} applied across detectors of different thicknesses (b) 1 cm thick detector with different electric fields.

Table 8. Detection efficiency of natural UO$_2$ detectors,1 and 10 mm thick, operating at electric fields of 10^3 and 10^4 V·cm^{-1}, if the charge carrier mobilities are 1 and 10 cm^2·V^{-1}·s^{-1}. Each detector is assumed to have a cross-sectional area of 1 cm^2 and charge carrier lifetime of 10^{-4} s. The integration time is set equal to the charge carrier transit time. The minimum CCE is set equal to the charge excited by α-particles within the integration time. A missing detection efficiency value means that there is no detection because the charge excited by fission fragments is smaller than that by α-particles.

d (mm)	**E (V/cm)**	**μ (cm^2·V^{-1}·s^{-1})**	**Detection efficiency (%)**		
			25 meV neutrons	**1 MeV neutrons**	**10 MeV neutrons**
1	10^3	1	0.91	4.4×10^{-3}	0.24
		10	0.94	4.5×10^{-3}	0.24
	10^4	1	0.94	4.5×10^{-3}	0.24
		10	0.94	4.5×10^{-3}	0.24
10	10^3	1	–	–	–
		10	5.8	2.9×10^{-2}	1.5
	10^4	1	5.8	2.9×10^{-2}	1.5
		10	8.7	4.4×10^{-2}	2.4

2.7. Summary

We have looked at the possibility of fabricating solid-state direct-conversion neutron detectors using oxides of uranium (UO$_2$, U$_3$O$_8$, and UO$_3$) with different isotopic combinations: ^{238}U, depleted U, natural U, low-enriched U, and ^{235}U. For uranium oxide detectors with the same thickness, the absorption probability of neutrons of a fixed energy is the highest for detectors with the highest content of ^{235}U since the fission cross-section of ^{235}U is higher than that of ^{238}U. A comparison of the fission cross-sections shows that the absorption probability of a detector is highest for thermal neutrons, followed by 10 and 1 MeV neutrons respectively. Based on the absorption probability of these materials, thicker detectors (thickness on the order of cm) would be required for fast neutrons whereas thinner detectors (thickness on the order of mm) may work for thermal neutrons, albeit the detection efficiency is likely to be low. For 10 MeV neutrons, the absorption probability values are similar for all oxides. Therefore, a detector could be made from any uranium oxide. A 1 cm thick detector will provide ~1% detection efficiency. For 1 MeV neutrons, only ^{235}U-based oxides could work and would still result in low efficiency, a few hundredth of a percent for a 1 cm thick detector. For thermal neutrons, detection may be possible with depleted uranium oxide with efficiency values ∼1% and ∼2% for detectors with thicknesses 1 and 10 mm respectively. However, the detection efficiency will be slightly higher, ∼1% and ∼6% for detectors of thicknesses 1 and 10 mm respectively, for oxides of natural uranium. The detection efficiency will be further increased, ∼3% for 1 mm and 20–30% for 10 mm detector, for low-enriched uranium.

A neutron absorption event in a detector eventually induces a current at the electrodes, which is integrated for a certain time to collect charge. The charge collected within the integration time must be greater than that collected due to leakage current, which could have various sources such as neutrons, background radiation, defects, free charge carriers, and intrinsic α-particle decay of uranium nucleus. Out of these, the intrinsic α-decay is likely to be the major source of leakage current. Assuming a detector with a thicknesses of 1–10 mm and a cross-sectional area of 1 cm^2 operating under an electric field of 1000 $V \cdot cm^{-1}$, and an integration time set equal to the transit time of charge carriers, a charge carrier mobility of 1–10 $cm^2 \cdot V^{-1} \cdot s^{-1}$ and carrier lifetime of 10^{-4}–10^{-5} s would be required in order to fabricate a uranium oxide neutron detector.

CHAPTER 3. METHODS: THEORY AND EXPERIMENTAL PROCEDURE

In order to study the potential of U_3O_8 and UO_3 for neutron detection, we studied the charge transport properties and other electrical/electronic properties of pressed pellets of these materials fabricated under different conditions (*vide infra*). The pellets were fabricated by uniaxial pressing of uranium oxide powder followed by sintering. The samples were prepared by our collaborators at The University of Tennessee, Knoxville (UTK). Basic characterization (measurement of stoichiometry and density, and identification of phase) was done at UTK, with the exception of acquiring x-ray diffraction data on UO_3, which was done at UMKC. Similarly, electrical measurements were done at UMKC, with the exception of current–voltage measurements on non-stoichiometric U_3O_8. The studies conducted at UTK will be covered in brief, whereas those conducted at UMKC will be explained in detail.

3.1. Fabrication of U_3O_8 Pellets (UTK)

Pellets of U_3O_8 were prepared by uniaxial pressing followed by sintering in a furnace. Batches of two to six pellets were fabricated under varying temperatures and times to allow for destructive testing of duplicate samples. A subset of these samples was characterized to determine grain size, stoichiometry, phase, electrical resistivity, and charge carrier mobility. The steps followed in fabricating these pellets are described in the following sections.

3.1.1. U_3O_8 Powder Preparation

U_3O_8 powder was prepared by heating uranyl acetate dihydrate powder slowly to 650 °C in a tube furnace and heating for 90 minutes. The powder was confirmed as α-U_3O_8 by powder x-ray diffraction (**Section 4.2.3**).

3.1.2. Pressing of U_3O_8 Pellets

The U_3O_8 powder was ground in a zirconia crucible to break apart any large agglomerates and produce roughly uniform particle size. About 600 mg of this powder was loaded in a circular steel die (die A), half an inch in diameter, which was lubricated with graphite. The die was then pressed at 5–8 ksi using a uniaxial press for a minute to obtain a close-packed green pellet. Many pellets fabricated in this way in the first phase were found to be less than pristine (e.g., they exhibited rough, chipped surface and cracks on the edges), attributed to flaws in the die used. Therefore, in the second phase, a new, commercially available die (die B) was used. Additionally, a mineral oil was used as a lubricant instead of graphite to reduce possible carbon contamination of the pellet surface.

3.1.3. U_3O_8 Pellet Sintering

Stoichiometric U_3O_8 pellets, obtained from the process described above, were then sintered on an alumina plate in a furnace at 1350 °C for 1–10 hours. A heating rate of 1.5 °C/min was used to slowly heat the samples up to the target temperature. The samples were then allowed to slowly cool to room temperature at a cooling rate of 3.0 °C/min.

3.1.4. $U_3O_{8\pm x}$ Sample Preparation

Nonstoichiometric samples were prepared by adding conditioning gases to the tube furnace during powder preparation (described in **Section 3.1.1**) as well as pellet sintering steps (**Section 3.1.3**) to alter the available oxygen. The initial hypostoichiometric and hyperstoichiometric samples were made with mixtures of 12% and 30% O_2 as well as air (~21% of O_2). Identical gas mixtures were used for both powder conversion and pellet sintering. The sintering was done at 1000 °C.

3.2. Fabrication of UO_3 Pellets (UTK)

Early UO_3 pellets were fabricated by decomposing uranyl nitrate, as will be described in **Section 3.2.1**. However, the samples prepared using this method were inconsistent. Therefore, commercially available UO_3 powder was used to fabricate pellets, which we describe in **Section 3.2.2**.

3.2.1. UO_3 Powder Preparation by Decomposition of Uranyl Nitrate

3.2.1.1. Theory

Based on existing literature [61], [71], [105], γ-UO_3 can be produced by decomposing uranyl nitrate by heating in air at 400 °C for 60 hours. The conversion process is described by the following decomposition reactions [105]:

$$\mathrm{UO_2(NO_3)_2 \cdot 6H_2O \longrightarrow UO_2(NO_3)_2 \cdot H_2O + 5H_2O}$$

$$\mathrm{UO_2(NO_3) \cdot H_2O + 5H_2O \longrightarrow UO_3 \cdot H_2O + 2NO_2 + \frac{1}{2}O_2}$$

3.2.1.2. Experiment

Uranyl nitrate hexahydrate was heated as described above to produce a rich orange powder, which was then finely ground in a zirconia mortar and pestle. After cooling, the powder was confirmed to be γ-UO_3 via powder x-ray diffraction.

3.2.2. UO_3 Powder Preparation from Commercially Available Material

In early experiments, commercially available UO_3 powder was directly used for pellet fabrication. In the later experiments, the UO_3 powder was conditioned by heating to 200–480 °C in a tube furnace in the presence of a mixture of oxygen and argon, with composition varying between 5–92% O_2/Ar. The powder was conditioned up to 60 hours to evaluate the effect of conditioning time on material properties.

3.2.3. Uniaxial Hot Pressing of UO_3 Pellets

UO_3 powder was loaded in a die, capable of being heated to 250 °C, and then pressed in a uniaxial press, while monitoring the temperature. The temperature was ramped at a rate of 2 °C/minute while applying pressure. The pressure was released during sample cooling after it cooled to below 75% of the set temperature. A load of 2–8 ton was applied to samples prepared without powder conditioning, whereas a load of 4.5–6 ton was applied to samples prepared from conditioned powder.

3.3. Basic Characterization of Pellets (UTK)

The basic characterization of the fabricated pellets included the determination of their crystal structure and phases, density, stoichiometry, and grain size.

3.3.1. Density

The density of the pellets was determined by using the Archimedes' method, using a balance equipped with a density kit. The following equation was used to calculate the density:

$$\rho = \frac{A}{A-B}(\rho_0 - \rho_\mathrm{L}) + \rho_\mathrm{L} \tag{3.1}$$

where ρ is the density, A is the weight of the pellets in air, B is the weight of the samples in an auxiliary liquid, ρ_0 is the density of the auxiliary liquid, and ρ_L is the density of air (taken to be 1.2×10^{-3} g·cm^{-3}).

Deionized water was used as the auxiliary liquid for U_3O_8 pellets. For UO_3 pellets, petroleum ether (density = 0.77 g·cm^{-3} at room temperature) was used as the liquid medium to prevent the formation of a hydrate phase.

3.3.2. Stoichiometry

The stoichiometry of the U_3O_8 samples was measured using a redox titration method adapted from the Davies and Grey method [106]. Similarly, the stoichiometry of UO_3 samples was determined by this same method as well as by inductively coupled plasma mass spectrometry in conjunction with x-ray diffraction.

3.3.2.1. Redox Titration

3.3.2.1.1. Theory

In this method, a known amount of Ce(IV) in solution is added to a dissolving uranium oxide specimen in excess of that needed to oxidize all uranium to U(VI). By titrating a standardized Fe(II) solution, the amount of excess cerium is measured, allowing the starting oxidation state of uranium to be calculated based on specimen weight. The redox reaction can be written as:

$$\mathrm{e^- + Ce^{+4} \longrightarrow Ce^{+3}}$$

$$\mathrm{Fe^{+2} \longrightarrow Fe^{+3} + e^-}$$

The overall redox reaction can be summarized as:

$$\mathrm{Ce^{+4} + Fe^{+2} \longrightarrow Ce^{+3} + Fe^{+3}}$$

If U(IV) or U(V) are present within an acidic solution, they will oxidize prior to a cerium–iron redox reaction. This changes the reaction to the following:

$$\mathrm{U^{+4} \longrightarrow U^{+6} + e^-}$$

$$\mathrm{2e^- + 2Ce^{+4} \longrightarrow 2Ce^{+3}}$$

$$\mathrm{U^{+4} + 2Ce^{+4} \longrightarrow U^{+4} + 2Ce^{+3}}$$

Using these simple reactions, it is possible to determine the U(IV) and U(VI) content within a U_3O_{8-x} sample expressed as a molar ratio. This ratio can then be related to the oxygen content. This process has been documented to give an x ± 0.002 accuracy for the stoichiometry of a hypostoichiometric uranium oxide [107], [108].

3.3.2.1.2. Experiment

The stoichiometry of the $U_3O_{8\pm x}$ samples was initially evaluated using the cerimetry redox titration method. The endpoint was determined by visual inspection of color change of a ferroin indicator. The results were found to be accurate to within 5 μL of titrant. Subsequently, potentiometric titration was used, allowing an accuracy to within 1 μL of titrant.

The stoichiometry of UO_3 was determined by cerimetric titration and inductively coupled plasma mass spectrometry combined with x-ray diffraction. The cerimetric titration method alone was not deemed reliable because the UO_3 pellets would form hydrates easily under ambient conditions and it was unclear if the hydrated compositions would impact the results of this method. Therefore, an additional method was also used in which uranium was directly quantified by inductively coupled plasma mass spectrometry and the result was combined with the results of quantification of hydrate content obtained from x-ray diffraction.

3.3.2.2. Inductively Coupled Plasma Mass Spectrometry

The uranium content of the UO_3 samples was determined by inductively coupled plasma mass spectrometry. Small pieces of UO_3 pellets were dissolved and diluted in stages to concentrations in the parts per billion range in a 2% nitric acid solution for analysis. First, a calibration curve was generated using a commercially available uranium standard (1000 μg/ml prepared in a matrix of 2% nitric acid) after diluting to different concentrations. Then, using the known values from the calibrated standards, ^{238}U intensities were used to determine the starting uranium mass fraction for each sample. Hydrate contribution to mass was estimated from x-ray diffraction data (obtained at UMKC), allowing for the stoichiometry to be calculated (see **Section 5.2.3**).

3.3.3. Phase Determination: X-ray Diffraction

The phase of the U_3O_8 powder was evaluated by x-ray diffraction (PXRD), using a Cu-Kα x-ray source at a scan rate of 10° per minute in the 2θ range of 10–100°. Automated Rietveld refinement tools [109] were used to refine the diffraction patterns.

The phase of a subset of UO_3 pellets (not powder) was determined by grazing incident x-ray diffraction [110] at UMKC, since PXRD could not be done on UO_3 powder due to restrictions on radioactive powder use with the equipment at UTK. The UO_3 pellets were placed on an aluminum sample holder and scanned at a rate of 1° per minute in the 2θ range of 5–65° in a Rigaku Miniflex+ benchtop diffractometer using a Co-Kα x-ray source. Automated Rietveld refinement tools were used to refine the diffraction pattern.

3.3.4. Sample Polishing and Grain Size Measurement

Pellets of U_3O_8 and UO_3 were polished to study their microstructure. The U_3O_8 pellets were first scraped with SiC paper at standard grit increments from 320 to 800 using water as lubricant. Samples were then polished using diamond suspensions from 9 to 3 μm using a nonwoven cloth. A final polishing was done using a 1 μm diamond supension on a napped pad.

The UO_3 pellets were polished in a similar way as U_3O_8; the only difference was the use of an alcohol-based lubricant instead of water in order to avoid the potential hydration of the pellets.

The average grain size of each sample was determined using the Heyn lineal intercept procedure [111] on multiple fields of view for digital micrographs of the sample surfaces.

3.4. Device Fabrication: Contact Deposition and Wiring (UMKC)

In order to study the charge transport properties of the fabricated pellets, it was necessary to fabricate device heterostructures suitable for a variety of different measurements. Various metals, such as copper, gold, and silver, were deposited as contacts depending on the experiment requirement and sample geometry used. Copper was deposited by DC magnetron sputtering whereas gold was evaporated by resistive thermal evaporation. Silver was deposited in the form of fast-drying silver paint and left for a few minutes to air dry. Wiring was done using either gold or copper wires, 20 μm in diameter, purchased from TopLine Corporation. Silver paint was used to connect the wires to the sample as well as to the external circuit.

3.5. Electronic Structure Study: Band Gap (UMKC)

Understanding the electronic structure of uranium oxides will enable us to understand their behavior in charge transport and detection experiments. We evaluated the band gap of UO_3 from diffuse reflectance spectroscopy using Kubelka–Munk theory

[112], [113]. The diffuse reflectance spectroscopy, Kubelka–Munk theory, and the details of our experiment are described below.

3.5.1. Diffuse Reflectance Spectroscopy: Theory

The band gap of thick and opaque materials can be determined by reflection-based techniques. Reflection techniques are mainly categorized into two types: internal and external. The internal reflection method involves the study of the interaction of radiation and the interface between a sample and a medium with a higher refractive index. On the other hand, the external reflection method involves the study of radiation reflected from a sample. The external reflection technique is further divided into two types: specular and diffuse. Specular reflection arises from smooth-polished, mirror-like surfaces whereas diffuse reflection is associated with roughness of a surface and scattering centers beneath it [113].

Diffuse reflection is the uniform reflection of light with no directional dependence for the viewer. It originates from a combination of internal scattering of light (i.e., the light is absorbed and then re-emitted) and external scattering from the rough surface of the object [114], [115]. The chief cause of diffuse reflection is the penetration of the sample by a certain portion of the incident beam. This portion of the incident beam then undergoes partial absorption and multiple scattering at the boundaries of the particles in the interior of the sample and eventually returns to the surface (at which the beam was incident initially) [116].

In diffuse reflection spectroscopy, an incident beam of light undergoes diffuse reflection from a powder or pellet sample, which is then collected by a spectrometer. The spectrum is then analyzed to obtain the band gap of the sample. We rely on Kubelka–Munk theory to determine the band gap.

3.5.2. Kubelka–Munk Theory

According to Kubelka–Munk theory [112], for a sample thick enough such that the light incident at one face is not transmitted through the opposite face, the Kubelka–Munk function, also known as the remission function, $F(R_\infty)$, is given as:

$$F(R_\infty) = \frac{(1 - R_\infty)^2}{2R_\infty} \tag{3.2}$$

where R_∞ is given as:

$$R_\infty = \frac{R_{\text{sample}}}{R_{\text{standard}}} \tag{3.3}$$

Here, R_{sample} and R_{standard} denote the reflectance of the sample and the standard respectively.

For a sample with absorption coefficient α, the Tauc equation [117], relating the band gap of the sample with its absorption coefficient, is given as

$$(\alpha h\nu)^n = C\left(h\nu - E_{\text{g}}\right) \tag{3.4}$$

where $h\nu$ is the incident photon energy and E_{g} is the band gap of the sample. Here, the value of n is ½ for a direct band gap material and 2 for an indirect band gap material.

According to the Kubelka–Munk theory, the absorption coefficient of a sample is related to its Kubelka–Munk function as:

$$F(R_\infty) = \frac{\alpha}{S} \tag{3.5}$$

where S is the scattering coefficient of the sample.

For most practical cases, where the thickness of a sample is much greater than the size of the individual particles in it, the scattering coefficient is constant [118]. So, using Equation (3.5) in Equation (3.4), we have:

$$[F(R_\infty)h\nu]^n = C_1\left(h\nu - E_\mathrm{g}\right) \tag{3.6}$$

A plot of photon energy, $h\nu$, versus $[F(R_\infty)h\nu]^n$, represented in Figure 11, is called Tauc's plot. The value of x at the onset of the linear region of the plot gives the band gap [119].

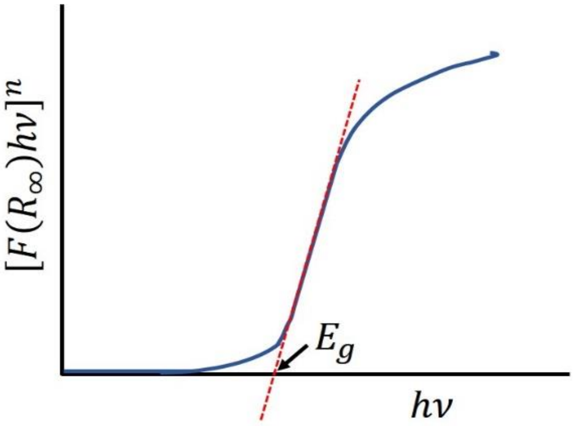

Figure 11. Plot to obtain the band gap of a material using Tauc's method.

3.5.3. Determination of Band Gap: Experiment

A schematic of the experimental set up for the diffuse reflectance spectroscopy experiment is shown in Figure 12. A special cable, consisting of optical fibers in an appropriate arrangement with three different ends is used. One end of the fiber is connected to a spectrometer, a second end is connected to a light source and the third end provides light on the sample at an angle of 45° to the horizontal (or vertical) via a probe holder. Care should be taken to use the "correct end" of the cable at the correct instruments. The optical fiber arrangement at different ends of the cable is shown in Figure 13. The cable end at the source consists of a solitary optical fiber to carry light from the source to the sample. The cable end at the sample consists of the source fiber at the center surrounded by the receptor fibers. These receptor fibers receive the light undergoing diffuse reflectance from the sample and transmit it to the spectrometer. The cable end at the spectrometer consists of the receptor fibers only. The result collected by the spectrometer is displayed as the intensity versus the wavelength of the light reflected from the sample.

In our experiment, we used an Ocean Optics USB 4000 spectrometer, Tunable Powerarc Illuminator light source, and Ocean Optics reflection probe holder. An Ocean Optics polytetrafluoroethylene (PTFE) reflection standard with a reflectivity of >98% was used.

The first step of the data acquisition was to obtain the diffuse reflectance spectrum of the standard. This was followed by acquiring the diffuse reflectance spectrum of a sample. The value of R_∞ was then calculated from Equation (3.4), which was used to find the Kubelka–Munk function and subsequently to obtain a Tauc's plot.

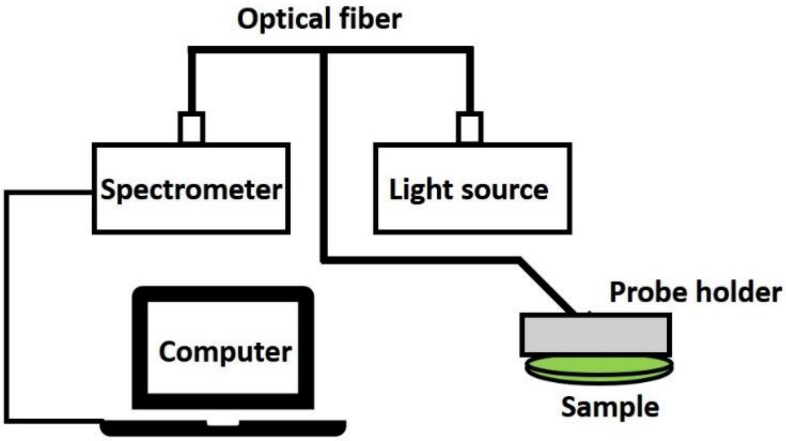
Optical fiber
Spectrometer
Light source
Probe holder
Computer
Sample

Figure 12. Schematic of experimental set up for diffuse reflectance spectroscopy.

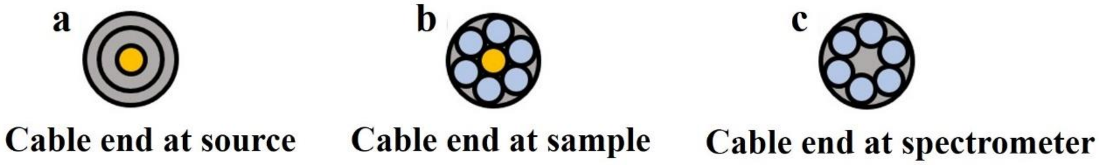
a
b
c
Cable end at source
Cable end at sample
Cable end at spectrometer

Figure 13. Optical fiber arrangement at different instruments.

3.6. Electronic Structure: Computational Studies: Theory (UMKC)

The electronic structure of UO_3 and associated compounds (discussed later in **Section 5.6.1.3**) was calculated using the density functional theory-based Vienna *ab initio* simulation package (VASP).

Electronic structure calculations for a material basically involve solving the Schrödinger equations for a large number of interacting electrons and nuclei.

The time-independent Schrödinger equation is:

$$H\psi = E\psi \tag{3.7}$$

where H is the Hamiltonian operator, E is the total energy of the system, and ψ is the wave function. For any material, the Hamiltonian is essentially the sum of kinetic and potential energies of the nuclear and electronic components, expressed as:

$$H = T_{\mathrm{n}} + T_{\mathrm{e}} + V_{\mathrm{nn}} + V_{\mathrm{ee}} + V_{\mathrm{ne}} \tag{3.8}$$

where, T_{n} and T_{e} are the kinetic energy operators of the nuclei and electrons respectively, and V_{nn}, V_{ee}, and V_{ne} are the electrostatic potentials of nuclei–nuclei, electron–electron, and nuclei–electron interactions respectively.

The Schrödinger equation cannot be solved for a many-body system, since the V_{ee} term does not allow for the wave function to be separated into a set of independent equations. Therefore, for many-body systems, the Born–Oppenheimer approximation [120] is used, which allows the nuclear and electronic terms to be decoupled. In this approximation, only the electrons are considered to be mobile relative to stationary nuclei, since the electrons are much lighter compared to the nuclei while the electrostatic force experienced by them is the same. Therefore, the kinetic energy operator of the nuclei is neglected (considering stationary nuclei) and the potential energy term associated with nuclei–nuclei interactions becomes a constant. The Hamiltonian given in Equation (3.8) then takes the form:

$$H = T_{\mathrm{e}} + V_{\mathrm{ext}}(\vec{R}_{\mathrm{i}}) + V_{\mathrm{ee}} \tag{3.9}$$

Here V_{ext} represents the external potential as “seen” by electrons due to nuclei at positions $\vec{R}_{\mathrm{i}}$.

3.6.1. Density Functional Theory

Density functional theory (DFT) is a method to calculate the electronic structure of a material in which electron density replaces the *N*-electron wave function and the associated Schrödinger equation. This method is based on the idea that the ground-state energy of a system can be obtained from the ground-state charge density. The electron density, $\rho(\vec{r})$, is expressed as:

$$\rho(\vec{r}) = |\psi(\overrightarrow{r_1}, \overrightarrow{r_2}, \dots \dots \dots, \overrightarrow{r_\mathrm{N}})|^2 \tag{3.10}$$

where, $\vec{r}_\mathrm{i}$ represents the position of the i^{th} electron. Thus, the problem reduces from 3*N* degrees of freedom to three spatial coordinates, which makes it solvable.

3.6.2. The Hohenberg and Kohn Theorems

DFT depends on two theorems given by Hohenberg and Kohn [121]. According to the first theorem, the external potential (V_{ext}) is a unique functional of the electron density (ρ); consequently, the ground-state expectation value of any observable is a unique functional of ρ, since V_{ext} is a part of the Hamiltonian (Equation (3.9)). Therefore, all of the ground- and excited-state properties of a system are determined by the electron density.

According to the second theorem, the total energy functional of electron density is given as:

$$E[\rho] = \int \rho(\vec{r}) V_{\mathrm{ext}}(\vec{r}) \mathrm{d}\vec{r} + F[\rho] = E_{\mathrm{ne}}[\rho] + F[\rho] \tag{3.11}$$

where,

$$F[\rho] = T[\rho] + E_{\mathrm{ee}}[\rho] \tag{3.12}$$

Here, the term $F[\rho]$ is known as the Hohenberg–Kohn functional, which comprises the kinetic energy term $T[\rho]$ and the potential energy term $E_{ee}[\rho]$ for electron–electron interactions. The term $E_{ee}[\rho]$ is obtained as:

$$E_{\mathrm{ee}}[\rho] = J[\rho] + E_{\mathrm{ncl}}[\rho] \tag{3.13}$$

where $J[\rho]$ is the Coulomb interaction term, and $E_{ncl}[\rho]$ is called the exchange and correlation contribution. Of all the terms introduced here, only $J[\rho]$ is explicitly known while $T[\rho]$ and $E_{ncl}[\rho]$ are unknown.

3.6.3. The Kohn–Sham Equations

The Kohn–Sham equations [122] provide a basis to obtain an approximate solution to the Schrödinger equation.

Combining Equations (3.11), (3.12), and (3.13), we have:

$$E[\rho] = E_{\mathrm{ne}}[\rho] + T[\rho] + J[\rho] + E_{\mathrm{ncl}}[\rho] \tag{3.14}$$

Of the terms on the right-hand side of Equation (3.14), $E_{ne}[\rho]$ and $J[\rho]$ were defined explicitly by Hohenberg and Kohn (**Section 3.6.2**); however, the remaining functionals were undefined.

The kinetic energy term, $J[\rho]$, depends on the velocity of electrons and therefore has a complicated association with the electron density, since the electron density relates to only the spatial distribution of electrons. Kohn and Sham devised a method to calculate as much kinetic energy as possible in an exact manner and approximated the remainder. In order to obtain the solution, a reference system of non-interacting electrons that has identical electron density as the real solution is used. The reference Hamiltonian is:

$$H_{\mathrm{Ref}} = \sum_{i}^{N} \left[-\frac{\hbar^2}{2m} \nabla_{\mathrm{i}}^2 + V_{\mathrm{Ref}}(\vec{r}_{\mathrm{i}}) \right] \tag{3.15}$$

where, $V_{\mathrm{Ref}}(\vec{r}_{\mathrm{i}})$ is the reference potential that allows for the ground-state electron density to be the same as the true electron density. Therefore, the ground-state energy of the non-interacting system is the same as the ground-state energy of the real system.

Since there are no electron–electron interacting terms, the solution to the reference system can be represented by a Slater determinant consisting of single electron wave functions, Φ_{i}, named Kohn–Sham orbitals. The single particle solutions for the reference system can be found from:

$$\left[-\frac{\hbar^2}{2m} \nabla_{\mathrm{i}}^2 + V_{\mathrm{Ref}}(\vec{r}_{\mathrm{i}}) \right] \phi_{\mathrm{i}} = \epsilon_{\mathrm{i}} \phi_{\mathrm{i}} \tag{3.16}$$

The kinetic energy of the reference system is then given as:

$$T_{\mathrm{Ref}} = -\frac{\hbar^2}{2m} \sum_{i}^{N} \int \phi_{\mathrm{i}}^{*} \nabla^2 \phi_{\mathrm{i}} \mathrm{d}\tau \tag{3.17}$$

The kinetic energy of the reference system, T_{Ref}, will now be introduced to Equation (3.14):

$$E_{\mathrm{KS}} = E_{\mathrm{ne}}[\rho] + T_{\mathrm{Ref}}[\rho] + J[\rho] + T[\rho] - T_{\mathrm{Ref}}[\rho] + E_{\mathrm{ncl}}[\rho] \tag{3.18}$$

Here, the subscript KS on the left-hand side of the equation has been added because the solution approach is based on the Kohn–Sham equation.

At this point, a quantity called the exchange-correlation functional, E_{XC}, is introduced, which is defined as:

$$E_{\mathrm{xc}}[\rho] = T[\rho] - R_{\mathrm{Ref}}[\rho] + E_{\mathrm{ncl}}[\rho] \tag{3.19}$$

The exchange-correlation functional contains the exchange and correlation energies as well as the remainder of the true kinetic energy. Introducing this term to Equation (3.18), we have:

$$E_{\mathrm{KS}} = E_{\mathrm{ne}}[\rho] + T_{\mathrm{Ref}}[\rho] + J[\rho] + E_{\mathrm{xc}}[\rho] \tag{3.20}$$

Now, a reference potential (V_{Ref}) is defined in such a way that it differs from the external potential (V_{ext}) by an additive constant only and produces a non-interacting system with the same electron density as the real system.

$$V_{\mathrm{Ref}}(\vec{r}) = V_{\mathrm{ext}}(\vec{r}) + \int \frac{\rho(\overrightarrow{r'})}{|\vec{r} - \overrightarrow{r'}|} \mathrm{d}\overrightarrow{r'} + V_{\mathrm{xc}}(\vec{r}) \tag{3.21}$$

where, $V_{\mathrm{XC}}(\vec{r})$ is the exchange-correlation potential determined by the functional derivative given as:

$$V_{\mathrm{xc}} = \frac{\delta E_{\mathrm{xc}}}{\delta \rho} \tag{3.22}$$

Therefore, the system is solved by generating an initial set of Kohn–Sham orbitals and using them to calculate a reference potential that can be used to minimize the energy of the Kohn-Sham orbitals within the reference system. The process is repeated until the system gives a self-consistent result.

3.6.4. Approximate Exchange-Correlation Functionals

Since the exchange-correlation term in the Kohn–Sham approach is impossible to solve exactly, an approximation must be used. The two most used approximations for the exchange-correlation functional are the local density approximation and the generalized gradient approximation.

In the local density approximation (LDA), the exchange-correlation functional is defined as [121]:

$$E_{\mathrm{xc}}^{\mathrm{LDA}}[\rho] = \int \rho(\vec{r})\epsilon_{\mathrm{xc}}[\rho]\mathrm{d}\vec{r} \tag{3.23}$$

where, $\epsilon_{\mathrm{XC}}[\rho]$ is the exchange-correlation energy density, i.e., the energy per particle of the uniform electron gas of density ρ.

The assumption made in the LDA is that the exchange-correlation function at a point depends solely on the electron density at that point. Although this may be true for simpler systems, this is not true for strongly correlated systems such as metals and semiconductors. Therefore, other approaches are preferred for strongly correlated systems [123].

An approach, sometimes considered to be better than the LDA, is the generalized gradient approximation (GGA), which takes into account the non-uniform spatial distribution of the electron density by incorporating the gradient of electron density into the exchange-correlation functional [124], [125]. The GGA exchange-correlation functional is generally defined as:

$$E_{\mathrm{xc}}^{\mathrm{GGA}}[\rho] = \int \rho(\vec{r})\epsilon_{\mathrm{xc}}(\rho, |\nabla\rho|)\mathrm{d}\vec{r} \tag{3.24}$$

In the GGA, there are different ways to approximate the exchange functional, such as Becke [126], PW91 [127], PBE [128], and B3LYP [126], [129], [130].

3.6.5. The Hubbard Coefficient (DFT+U)

Despite achieving significant success, DFT alone is insufficient to describe systems with strongly correlated (or localized) *d*- and *f*-electrons. DFT predicts partially filled bands with metallic electronic structure instead of the real properties of high-atomic-number systems, such as transition metal and rare-earth oxides (semiconductors and insulators) [131]. This problem can be papered over by introducing a term, the Hubbard coefficient, that accounts for strong on-site correlation [132]. The Hubbard coefficient depends on two parameters: the effective on-site Coulomb parameter (U) and the effective on-site exchange parameter (J). There are two ways in which the Hubbard coefficient can be introduced to DFT calculations. The first method is Dudarev's scheme [133], in which the individual values of U and J are insignificant, however, the difference between the two is introduced in the calculations. The second method is Liechtenstein's approach [134], in which each of the U and the J terms contribute to correcting the self-interaction error. The values U and J can be obtained from core level scans (*d*- and *f*-orbitals) obtained from x-ray photoelectron spectroscopy (XPS) [135].

3.6.6. Pseudopotentials

It is impractical to express the wave functions of core electrons (of a material) using plane-wave basis sets because this requires a large number of plane waves, since the wave functions of such electrons are highly oscillatory. Therefore, an effective potential, referred to as pseudopotential, replaces the core electrons and the true potential. This treatment is based on the idea that the physical properties of a material are highly influenced by the valence electrons in comparison to the core electrons. The pseudopotential acts on a set of pseudo-wave functions, ψ_{pseudo}, which are the same as the true wave function ψ outside a certain cut-off radius r_c; an illustration is presented in Figure 14 [136]. The introduction of pseudopotentials allows for a system to be described with fewer plane waves.

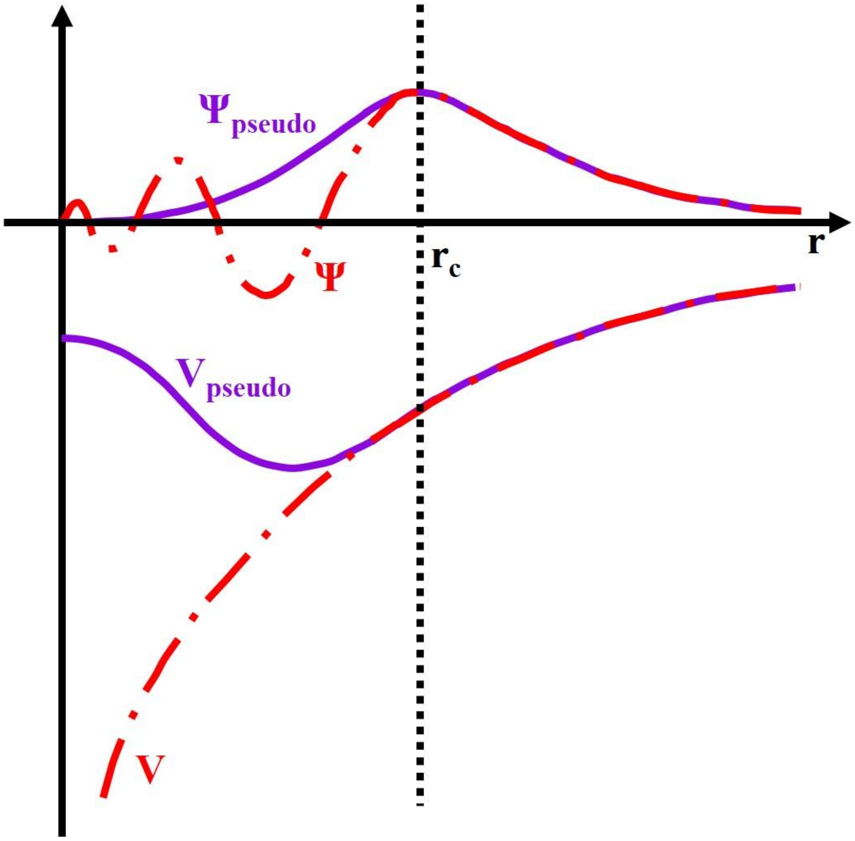

Figure 14. Schematic illustration of an all-electron potential (dashed lines) and a pseudopotential (solid lines) and the associated wave functions; r_c is the cut-off radius [136].

There are different types of pseudopotentials, such as norm-conserving pseudopotentials [137], ultra-soft Vanderbilt pseudopotentials [138], [139], and the projector augmented wave (PAW) pseudopotential [140], [141]. The pseudopotential is chosen depending on the system of interest to improve the efficiency as well as the results of computations [123].

3.6.7. Density of States

The density of states (DOS) of a system is the number of states that electrons can occupy at a particular energy level, i.e., the number of electronic states per unit energy per unit volume. The DOS gives the band structure, which shows all of the available states (whether occupied or unoccupied) arising from the overlap of atomic orbitals in a system [142]. The partial density of state (PDOS) shows the contribution of individual orbitals to the valence and the conduction bands and provides information such as the orbitals contributing to bonding.

3.6.8. Electronic Structure Calculation

The electronic structures of γ-UO_3 and associated compounds (as will be explained in **Section 5.6.1.3**) were calculated using the Vienna *ab initio* Simulation Package (VASP) [143]. The atomic coordinates of a 64-atom UO_3 crystal were given as input to VASP, which geometrically optimized the crystal structure and calculated the PDOS. The input structure of UO_3 was obtained from the crystallographic open database (COD ID 1527741) [82], [144]. To calculate the electronic structures of the mixed compounds, an atom of uranium was replaced with a selected foreign atom in the UO_3 crystal. The same calculation parameters (*vide infra*) were used in all of the calculations.

In these calculations, the exchange correlational function was approximated by the PBE approach [128], and the PAW pseudopotential [140], [141] was used, based on the literature [56], [70], [145]. Dudarev's scheme [133] was applied with *U* and *J* values of 4.50 and 0.54 eV respectively to the *f*-electrons of uranium. The *U* and *J* values, reported in the literature, have been derived for UO_2 from XPS experiments [135]. These values are very likely to depend upon atomic coordination, and thus could be different for UO_3. However, we used these values because there are no experimentally derived values for UO_3 and we adopted the method used in the literature [56], [70], [145]. A plane wave cut-off energy of 500 eV and *k*-point mesh of 6×6×2 was used in our calculations, based on literature parameters [145]. The calculations were done using the computing resources at Research Computing Support Services of the University of Missouri System.

APPENDIX A contains example INCAR, KPOINTS, and POSCAR input files for a 64-atom UO_3 crystal. The INCAR file contains the parameters to control the calculations, the KPOINTS file contains the *k*-points (mesh), and the POSCAR file contains the lattice geometry and initial atomic positions in the crystal.

3.7. Resistivity Measurement (UMKC)

The electrical resistivity of different pellets was measured using a series of different techniques and variations to (a) verify the reproducibility of the results, and (b) determine the most suitable technique from those available.

3.7.1. Four-Point Probe – van der Pauw

3.7.1.1. Theory

The van der Pauw method is suitable for measuring the electrical resistivity of a thin sample of arbitrary shape [146]. In this method, four contacts are fabricated at the edges of a sample (Figure 15 (a)): a current is sourced between two adjacent contacts, and the resulting voltage between the remaining two contacts is measured. Ideally, the contacts should be small and on the edge of the sample. For this reason, a probe system, in which the tip of the probe is extremely small (e.g., tens of micrometers in diameter), is generally used.

In order to find the resistivity of the sample, it is first necessary to find the four resistances: R_{1234}, R_{2341}, R_{3412}, and R_{4123}. The resistance R_{1234} is defined as:

$$R_{1234} = \frac{V_{34}}{I_{12}} \tag{3.25}$$

where V_{34} is the voltage measured between points 3 and 4, and I_{12} is the current sourced between points 1 and 2. Similarly, R_{3412} is given as:

$$R_{3412} = \frac{V_{12}}{I_{34}} \tag{3.26}$$

From the reciprocity theorem, $R_{1234} = R_{3412}$; however, in practice, these quantities differ by a small amount. So, we take the average and denote by R_1,

$$R_1 = \frac{1}{2}(R_{1234} + R_{3412}) \tag{3.27}$$

A similar approach is used to find R_2, where,

$$R_2 = \frac{1}{2}(R_{2341} + R_{4123}) \tag{3.28}$$

The resistivity, ρ, is determined by using the equation:

$$\exp\left(-\frac{\pi t R_1}{\rho}\right) + \exp\left(-\frac{\pi t R_2}{\rho}\right) = 1 \tag{3.29}$$

where t is the thickness of the sample.

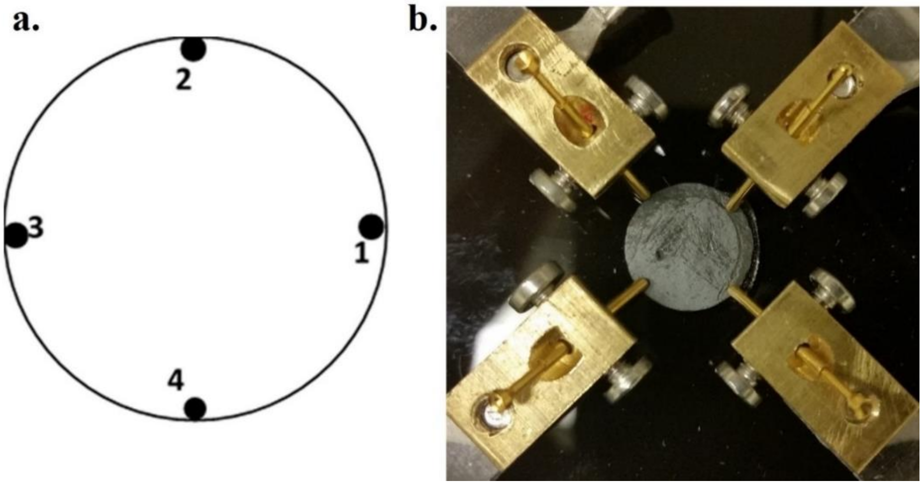

Figure 15. (a) A schematic for a circular sample with four-point contacts for van der Pauw resistivity measurement; (b) A U_3O_8 sample in the van der Pauw probe system.

3.7.1.2. Experiment

A custom-built system with gold/tungsten probes was used to mount the samples, as shown in Figure 15 (b). The current was sourced through a Keithley 2400 sourcemeter from 0–200 μA in steps of 2 μA, and the voltage was measured by a Keithley 2000 multimeter. A LabView-based program was used to control the instruments and to record the data.

3.7.2. Four-Point Probe – Linear

3.7.2.1. Theory

In this method, four probes are placed in a straight line on the surface of a sample (Figure 16 (a)). A current (*I*) is sourced through the outer probes and the potential difference (*V*) across the inner probes is measured [147]. In order to apply this method, the following assumptions must hold: (1) the material has a uniform resistivity (2) the contact surface between the probes and the sample is hemispherical and the contact radii are small relative to the probe spacing (3) the sample surface is flat and the recombination rate is so high that any charge injected from the probes recombines close to the probes [148]. The resistivity of the sample is given as [149]:

$$\rho = 2\pi s \frac{V}{I} F \tag{3.30}$$

where *s* is the probe spacing and *F* is a correction factor. There are various factors that affect the value of *F* [149]. If the sample thickness (*t*) is on the order of probe spacing or less, the correction factor is given as:

$$F_1 = \frac{\frac{t}{s}}{2\ln\left[\frac{\sinh\left(\frac{t}{s}\right)}{\sinh\left(\frac{t}{2s}\right)}\right]} \tag{3.31}$$

If $t \leq s/2$, then equation (3.32) reduces to:

$$F_1 = \frac{\frac{t}{s}}{2\ln(2)} \tag{3.32}$$

For samples of finite diameter, the correction factor is given as:

$$F_2 = \frac{\ln(2)}{\ln(2) + \ln\left[\frac{\left(\frac{D}{s}\right)^2 + 3}{\left(\frac{D}{s}\right)^2 - 3}\right]} \tag{3.33}$$

3.7.2.2. Experiment

We used four silver-painted contact points, about 1 mm in diameter, with a spacing of 2 mm center-to-center, to which gold wires were connected (Figure 16 (b)). Each gold wire was connected to a different metallic pin on a PTFE sample platform. Two metallic pins (connected to inner wires from the sample) were connected to a Keithley 2000 multimeter and the remaining two pins were connected to a Keithley 2400 sourcemeter. Current of 0–200 μA in steps of 2 μA was sourced through the sourcemeter, and the voltage was measured by the multimeter. The voltage was measured again after reversing the current direction. The average of the slope of the current–voltage graph was taken as the average *V*/*I*. The correction factors for finite thickness and diameter were used. At UTK, a commercial probe system was used in which a sample was placed inside the system with four probes touching the surface of the sample.

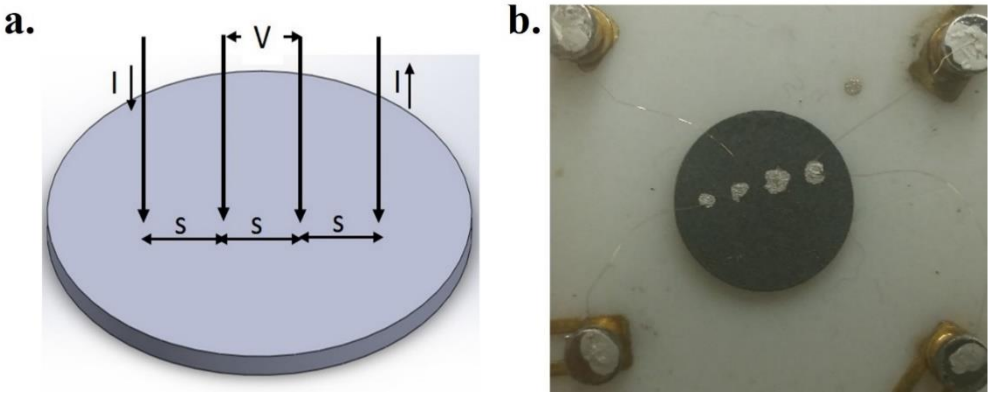

Figure 16. (a) Schematic of linear 4-point probe resistivity measurement (b) a U_3O_8 sample wired for resistivity measurement in a 4-point linear probe configuration.

3.7.3. Metal–Insulator–Metal Heterostructure

For samples with high resistivity ($\geq 10^4$ Ω-cm), the four-point probe methods are more likely to give unreliable results [149]. Therefore, for those samples, the resistivity was determined from current–voltage measurement in a metal–insulator–metal (MIM) geometry. Contacts were prepared on opposite faces of the sample. A potential difference was applied across the contacts, and the resulting current in the circuit was measured. On some samples, a guard ring was incorporated to exclude potential surface current (Figure 17, Figure 18) by applying the same potential to the center contact and the guard ring. A Keithley 2400 sourcemeter was used to source 0–200 V in steps of 1 V and a Keithley 6485 picoammeter was used to measure the resulting current. A LabView-based program was used to control the instruments and record the data.

The resistance (R) of the sample was determined from the slope of its I–V graph, which was used to determine its resistivity (ρ) as:

$$\rho = \frac{RA}{d} \tag{3.34}$$

where A and d are the contact area and thickness of the sample, respectively.

After evaluating various techniques, the resistivity of the U_3O_8 samples was obtained using the four-point method whereas that of the UO_3 samples was determined using the MIM method.

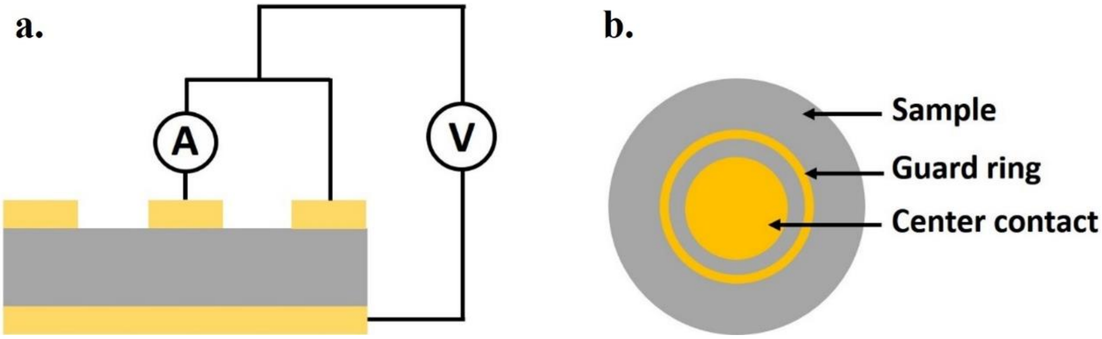

Figure 17. (a) Circuit diagram to measure resistivity in the MIM geometry with a guard ring (b) Representation of top view of a sample in an MIM structure with a guard ring.

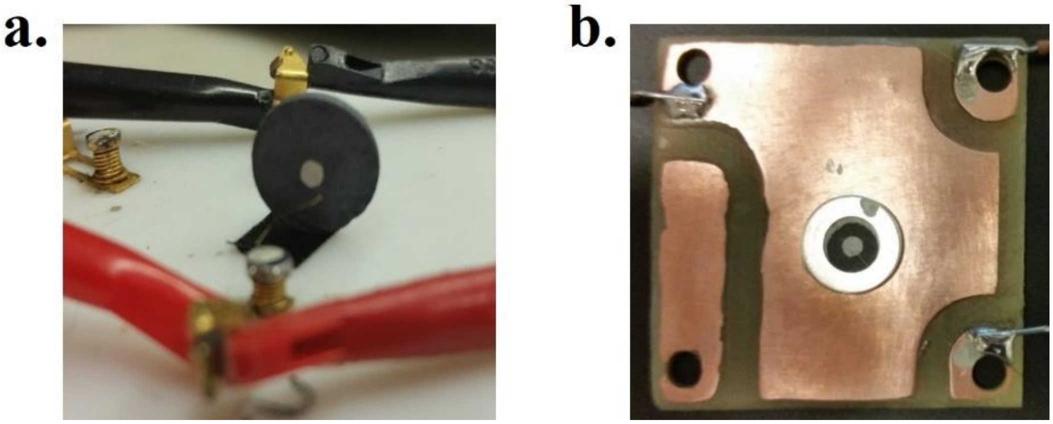

Figure 18. *I–V* measurement in MIM geometry (a) without a guard ring (b) with a guard ring.

3.8. Charge Carrier Mobility Measurements (UMKC)

The charge carrier mobility of a material can be evaluated using different techniques which include Hall effect measurements [149], the dark-injection space-charge-limited current method [150], impedance spectroscopy [151], the steady-state space-charge-limited current method [152], the charge extraction by linearly increasing voltage method [153], and time-of-flight photoconductivity experiments [154]. An overview of each of these methods is given below.

In **DC Hall effect measurements**, a direct current (DC) is sourced through a sample, and a magnetic field is applied perpendicular to the plane of the current. This gives rise to a potential difference, the Hall voltage, across the sample in a direction perpendicular to both the current and the magnetic field. The charge carrier mobility of the sample can be determined from the Hall voltage, provided its resistivity is known.

The DC Hall effect measurement is suitable for materials with charge carrier mobility 1 $cm^2 \cdot V^{-1} \cdot s^{-1}$ and higher. The DC Hall effect method will be described more in **Section 3.8.1**. For materials with a charge carrier mobility of 0.1–1 $cm^2 \cdot V^{-1} \cdot s^{-1}$, an **AC Hall effect measurement** [155] can be used, which consists of sourcing an alternating current (AC) through the sample to obtain the Hall voltage.

In the **steady-state space-charge-limited current** (**SS-SCLC)** method, the current–voltage characteristics of a sample at high voltages are studied. If the sample is subjected to a sufficiently high electric field, the current through it depends on the carrier mobility according to the Mott–Gurney law [152], provided that the contacts employed are carrier-injecting. Thus, the current–voltage graph can be fit to the Mott–Gurney equation to obtain the charge carrier mobility of the sample. Despite the relatively simple experimental setup, the data obtained from this experiment are sometimes difficult to interpret and the carrier mobility may not be obtainable [156]–[158]. The minimum electric field required to set up the space-charge regime in a material is inversely proportional to its resistivity and charge carrier mobility, and directly proportional to its thickness. Therefore, this method may not be useful for thick samples with low charge carrier mobility and/or resistivity, because the electric field required may be too high from an experimental point of view. This method will be described more in **Section 3.8.2**.

In the **dark-injection space-charge-limited current (DI-SCLC) method**, a step voltage that is sufficient to set up a space-charge-limited current is applied to a sample, and its current response it observed. A typical DI-SCLC signal is shown in Figure 19. With the onset of the input pulse, a displacement current is set up in the sample, which decays immediately, provided the *RC* time constant of the experimental circuit (*C* is the capacitance of the sample, *R* is the resistance in series with the sample, i.e., the input impedance of the measurement device) is sufficiently small. Then the current through the sample increases to a maximum value at a time t_0, and gradually decreases to a constant current, which is the steady-state space-charge-limited current. The transit time (t_{tr}) of the charge carriers, defined as the time taken by the charge carriers to travel through the thickness of the sample, is related to t_0 by $t_0 = 0.786\ t_{tr}$. The charge carrier mobility can then be obtained from the transit time, the sample thickness, and the applied voltage.

In order to carry out this experiment, the *RC* time constant of the experimental circuit should be smaller than the transit time of the charge carriers. For thinner films, higher voltages, and/or higher charge carrier mobility materials, the transient peak may be harder to discern, since it is masked by the *RC* effects (i.e., the decay of the displacement current). Therefore, various factors, such as charge carrier mobility and thickness of a sample, as well as the voltage required to set up a space-charge regime in the sample limit the use of this method. Although this method is equally capable, in principle, of measuring high as well as low carrier mobility, it has traditionally been used to measure low charge carrier mobilities (10^{-3}–10^{-6} $\mathrm{cm^2{\cdot}V^{-1}{\cdot}s^{-1}}$). Usually this method is appropriate for samples with thicknesses of 0.2–200 μm [150].

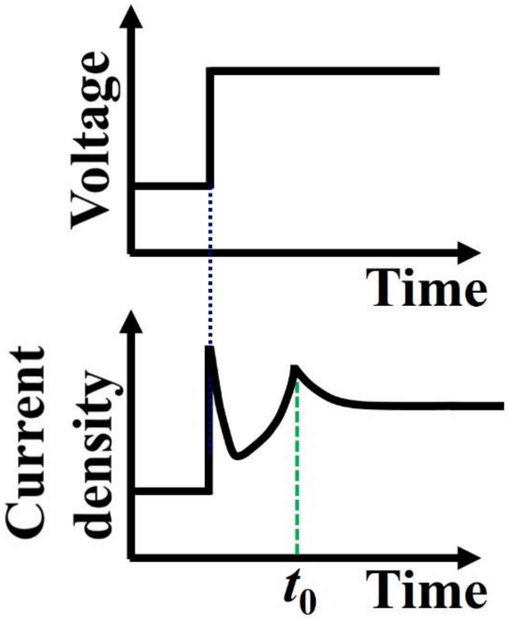

Figure 19. A typical dark-injection space-charge-limited current signal. The top graph represents the applied voltage pulse whereas the bottom graph represents the signal observed.

In the **charge extraction by linearly increasing voltage** (**CELIV) method**, a linearly increasing voltage is applied to a sample and its current response is observed. An ideal signal observed in a CELIV experiment is represented in Figure 20. From the observed signal, the time taken by the current to reach a maximum (t_M) value is obtained, from which the charge carrier mobility of the sample is determined.

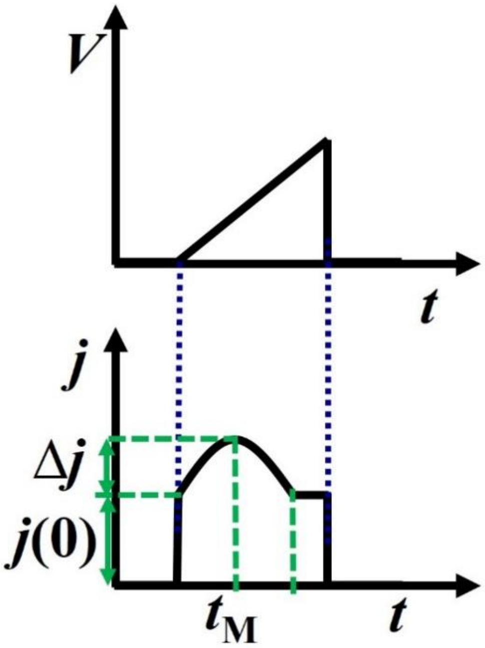

Figure 20. Representation of an ideal transient current obtained in the CELIV experiment. The top graph represents the applied voltage ramp whereas the bottom graph represents the signal observed. Here, *j*(0) is the current due to the capacitance of the sample and Δ*j* is the difference between maximum current density and *j*(0).

The range of mobilities that can be measured with this technique is dependent on the ramp rate achievable from the source, the sample geometry, and the *RC* constant of the measurement circuit (*C* is the capacitance of the sample and *R* is the resistance in series with the sample, i.e., the input impedance of the measurement device). This method cannot be used for materials with charge carrier mobility so low that the extraction maximum can only be achieved after the end of the input pulse. On the other hand, if the charge carrier mobility is too high, t_M is close to the circuit *RC* constant, and ultimately the signal maximum is hard to discern. The lowest value of charge carrier mobility that can be measured by this technique is on the order of 10^{-6} $cm^2 \cdot V^{-1} \cdot s^{-1}$ [159]. The highest value of the charge carrier mobility evaluated with this technique has been found to be 290 $cm^2 \cdot V^{-1} \cdot s^{-1}$ [153], however this method is used mostly to evaluate low charge carrier mobility, since the higher values can be evaluated by much simpler techniques, such as Hall effect measurements.

In **impedance spectroscopy (IS)**, a DC voltage is applied to generate a space-charge-limited current in a sample with the simultaneous application of a much weaker AC voltage. The admittance is measured as a function of AC frequency, from which the transit time of the charge carriers is determined, which can then be used to evaluate the charge carrier mobility [150]. The range of mobilities that can be measured with this method is 10^{-8}–1 $cm^2 \cdot V^{-1} \cdot s^{-1}$ [160], [161]. This method is generally suitable for thin films, and only appropriate for thick samples with high charge carrier mobility. For thick samples with low charge carrier mobility, the transit time may be harder to discern.

In the **time of flight (ToF) photoconductivity** experiment, a sample is irradiated with a pulse of low-intensity light through an optically transparent electrode to excite a sheet of charge in the material just underneath the electrode. The motion of this sheet of charge towards the opposite electrode is observed, from which the transit time of charge carriers can be determined and subsequently the charge carrier mobility obtained. This method is applicable to samples which are thick enough so that the incident pulse is absorbed in a short distance compared to the distance travelled by the excited photoelectrons [159]. In general, the thickness of the sample should be greater than 1 μm in order to have a well-defined flight distance for charge carriers [150]. The ToF photoconductivity method will be described more in **Section 3.8.3**.

After reviewing the criteria for these mobility measurement techniques, and testing a majority of them, the Hall effect measurement was deemed to be the most useful for U_3O_8 samples whereas the SS-SCLC and the ToF photoconductivity methods were deemed to be the most useful for UO_3 samples in general, and will be described in more detail below.

3.8.1. DC Hall Effect Measurement

3.8.1.1. Theory

The DC Hall effect method is a standard technique for measuring charge carrier mobility in a solid. There are different sample geometry and electrode configurations that can be used for this technique [149], out of which the van der Pauw geometry is the most simple and convenient [146] for a flat sample (surface area $\gg$ thickness).

When an electric current is passed through a material and a transverse magnetic field is applied to the sample, a potential difference, referred to as the Hall voltage, is set up in the sample in a direction perpendicular to both the current and the magnetic field. This happens because the charge carriers moving in the magnetic field are deflected due to the Lorentz force, thereby setting up a potential difference. A deflection of mobile charge carriers occurs until the Hall voltage is sufficient to oppose the deflection [162].

A schematic of the Hall effect for an *n*-type semiconductor is shown in Figure 21. In the figure, B represents the magnetic field directed towards the observer, and 1, 2, 3, and 4 represent the four contact points along the edge of the sample. The direction of the arrow shows the direction of deflection of the electrons.

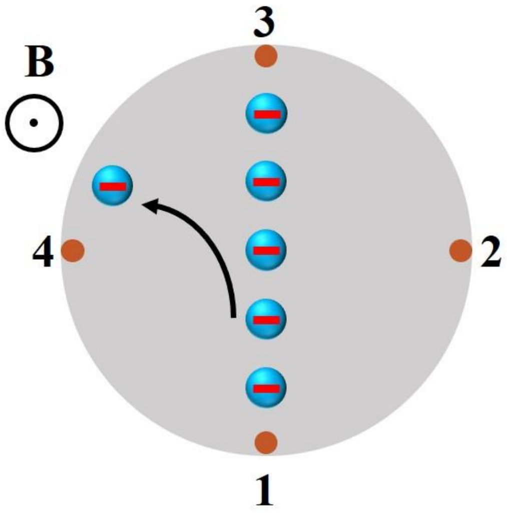

Figure 21. A schematic of the Hall effect for an *n*-type semiconductor.

In this experiment, the current is sourced between opposite points (e.g., 1 and 3 in Figure 21), and the voltage between the other two points is measured; the magnetic field is applied perpendicular to the plane of the sample.

The Hall voltage (V_H) is the difference between the voltage in the presence and absence of the magnetic field.

$$V_\mathrm{H} \equiv V_\mathrm{N} - V_0 = V_\mathrm{S} - V_0 \qquad (3.35)$$

$$2V_\mathrm{H} = (V_\mathrm{N} - V_\mathrm{S}) \qquad (3.36)$$

where V_0 is the voltage in the absence of a magnetic field (which is ideally zero), V_N is the voltage when the north pole of the magnet faces upwards from the sample, and V_S is the voltage when the south pole of the magnet faces upwards from the sample. A graph of sourced current versus $2V_{\mathrm{H}}$ is plotted, which should be a straight line. The slope (m) of this line is used to find the Hall coefficient (R_{H}) as:

$$R_{\mathrm{H}} = \frac{m}{2}\frac{t}{B} \tag{3.37}$$

where t is the sample thickness and B is the magnitude of the magnetic field. The Hall coefficient can be used to obtain the mobility (μ), concentration (n), and type (electron/hole) of charge carriers in the sample, as given by the following equations:

$$\left.\begin{aligned} \mu &= \frac{R_{\mathrm{H}}}{\rho} \\ n &= \frac{1}{R_{\mathrm{H}}e} \end{aligned}\right\} \tag{3.38}$$

3.8.1.2. Experiment

We used a custom-built probe system with gold/tungsten probes (**Section 3.7.1**) to mount the samples. A current of 0–200 μA in steps of 2 μA was sourced through the sample with a Keithley 2400 sourcemeter and the resulting voltage was measured with a Keithley 2000 multimeter. The probe system (with the sample) was placed between the poles of a Varian electromagnet system (Figure 22), and a magnetic field of 2T was used. Two LabView-based programs were used: one to control the electromagnet (such as changing the magnitude and direction of magnetic field) and the other to control the other instruments (sourcemeter and voltmeter) and acquire the data.

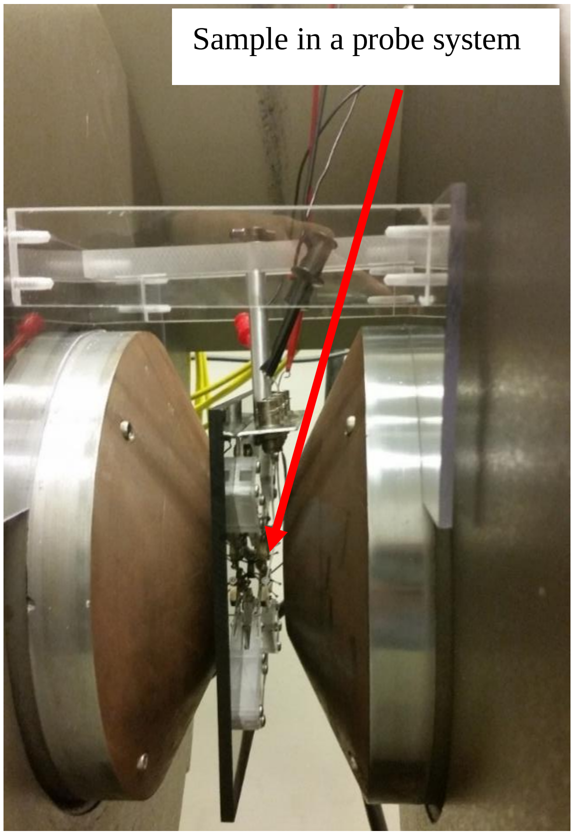

Figure 22. U_3O_8 sample in van der Pauw geometry placed in a magnetic field.

3.8.2. Steady-State Space-Charge-Limited Current

3.8.2.1. Theory

As described above, the current–voltage behavior of a sample at high voltage is used to evaluate the charge carrier mobility of the sample using the steady-state space-charge-limited current technique. Assuming that a semiconductor has only one type of charge carrier and injecting contacts, the number of charge carriers entering the semiconductor from the contacts increases with increasing bias voltage. When the voltage is so high that the concentration of the injected charge carriers just exceeds that of the free charge carriers in the semiconductor, the semiconductor is said to be in a space-charge regime. At this point, the current through the semiconductor is independent of its resistivity; instead it depends on its charge carrier mobility (μ) as given by the Mott–Gurney law [152]:

$$J = \frac{9}{8}\epsilon\mu\frac{E^2}{d} \tag{3.39}$$

where J is the current density through the sample, ϵ is the permittivity of the sample, d is the thickness of the sample, and E is the applied electric field.

The minimum voltage required across a semiconductor to transition from the ohmic to the space-charge region is given as [152]:

$$V = \frac{d^2}{\epsilon\mu\rho} \tag{3.40}$$

where ρ is the resistivity of the semiconductor.

In terms of current (I) and voltage (V), Equation (3.39) can be written as:

$$I = \frac{9}{8}\,\epsilon\mu A\frac{V^2}{d^3} \tag{3.41}$$

where, A is the cross-sectional area of the semiconductor.

Taking the logarithm on both sides of Equation (3.41) and rearranging, we have:

$$\log I = 2\log V + \log\left(\frac{9\epsilon\mu A}{8d^3}\right) \tag{3.42}$$

Thus, a double log plot of current vs voltage across a semiconductor at high voltage in the space-charge regime should yield a straight line with slope 2. From the y-intercept of this line, the charge carrier mobility can be evaluated.

3.8.2.2. Experiment

We designed a voltage divider circuit, as shown in Figure 23, and wrote a LabView-based program to safely acquire *I*–*V* measurements in the high voltage region. The voltage (V_s) was sourced with a Bertan Associates Inc. Model 210-10R High Voltage Power Supply, which was operated through an Arduino integrated with a LabView-based program. The voltage (V_2) across the resistor R_2 was measured with a Keithley 2000 Multimeter, operated by the LabView-based program. The sample was prepared in a metal–insulator–metal geometry as described in **Section 3.7.3.**

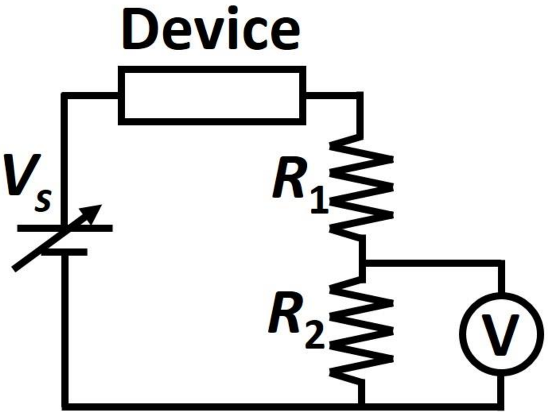

Figure 23. Circuit for high-voltage *I*–*V* measurements.

The current in the circuit was obtained from V_2 and R_2 using Ohm's law:

$$I = \frac{V_2}{R_2} \tag{3.43}$$

The voltage (V_1) across the resistor R_1 was obtained from:

$$V_1 = V_2 \frac{R_1}{R_2} \tag{3.44}$$

Finally, the voltage (V_D) across the sample was obtained by subtracting V_2 and V_1 from V_s as:

$$V_D = V_S - V_2 \left(\frac{R_1}{R_2} - 1 \right) \tag{3.45}$$

For convenience, R_1 and R_2 were chosen as 10 and 1 kΩ respectively.

3.8.3. Time of Flight Photoconductivity

In this experiment, a sample is irradiated with a pulse of low-intensity light through an optically transparent electrode to excite a sheet of charge in the material just beneath the electrode. The sheet of charge moves towards the opposite electrode under the effect of applied voltage, provided the biasing is correct in polarity. The motion of the charged sheet is displayed in an oscilloscope. A schematic of the experimental set-up is shown in Figure 24, and a typical transient photocurrent signal is shown in Figure 25. The photocurrent signal behaves in this way because when the photo-excited sheet of charge begins to move, a current, called a photocurrent, is induced at the contacts, which reduces to zero after the carriers reach the collecting electrode [159].

The transit time (t_{tr}), defined as the time taken by the photo-excited sheet of charge to cross the sample, can be determined from the signal observed in the oscilloscope. Then the charge carrier mobility can be determined as:

$$\mu = \frac{d^2}{V t_{\mathrm{tr}}} \tag{3.46}$$

where, d is the sample thickness (i.e., the distance between the two electrodes) and V is the applied voltage.

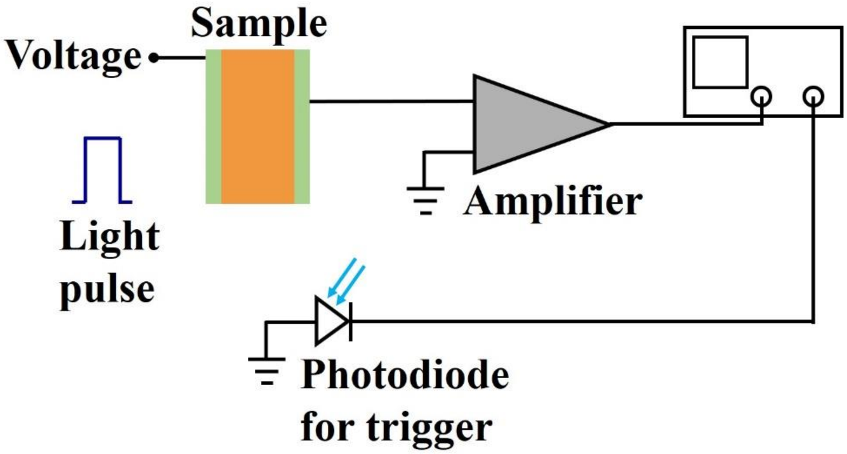
Sample
Voltage
Light pulse
Amplifier
Photodiode for trigger

Figure 24. A schematic of the ToF photoconductivity experiment.

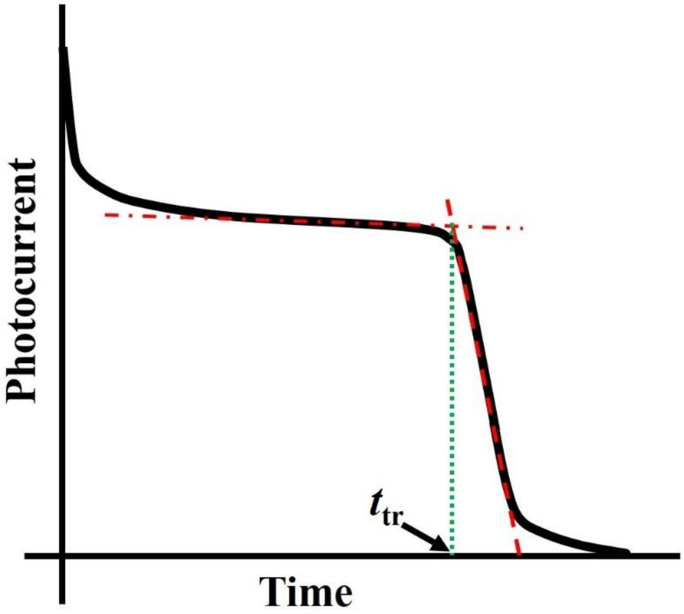

Figure 25. A typical signal obtained from a ToF photoconductivity experiment.

3.8.3.1. Requirements for the ToF Photoconductivity Experiment

There are two major requirements that must be met to carry out the ToF photoconductivity experiment: (1) the sample should be thick enough so that the light pulse is absorbed in a very short distance relative to the distance travelled by the photo-excited charge carriers, and (2) the transit time (t_{tr}) should be smaller than the dielectric relaxation time (t_d), i.e., $t_{tr} < t_d$. For a material with a high resistivity and reasonably high carrier mobility, the second condition is relatively easy to achieve, whereas for a material with a high resistivity and low carrier mobility, achieving both of the conditions simultaneously is usually difficult. If the sample is too thick, the first condition will be fulfilled; however, this will lead to the possibility of the transit time exceeding the dielectric relaxation time. On the other hand, if the sample is thin, the second condition is easier to achieve but the first condition may not be met.

3.8.3.2. Choice of Electrodes

The choice of electrodes is an important aspect for photoconductivity experiments. The results of a ToF photoconductivity experiment are more reliable if the photo-excited sheet of charge carriers is thin. This can be achieved by avoiding any effect that tends to broaden the sheet of charge carriers, which arises mainly when excess charge is injected from the electrodes. Therefore, blocking electrodes should be used. Overall, one of the electrodes should be transparent (at least partially) and block the injection of charge carriers under study [163].

It is a challenge to obtain an electrode that is both conducting and optically transparent. To choose a proper conducting material, which also acts as a carrier blocking electrode is an additional challenge. A metal with a work function lower than that of an *n*-type semiconductor can be expected to form a blocking contact for electrons (at least theoretically; experimentally the metal–semiconductor interface is extremely complicated and there are several factors that can alter the interface characteristics) [149]. An extremely thin layer of metal can be used as a reasonably transparent electrode. However, a thin layer of metal will have a high resistance [164], [165]. Overall, if the metal layer is too thick, it is conductive but not sufficiently transparent, whereas if the layer is too thin, it is transparent enough but not sufficiently conductive. So, a trade-off needs to be found such that the electrode is sufficiently transparent as well as conductive.

We chose to use gold as a transparent blocking contact. The band gap of UO_3 can be taken as ∼2 eV on average from the results of our experiments (**Section 5.3**). The electron affinity of UO_3 is 2.1 eV [166]. Since UO_3 is an *n*-type semiconductor, we can assume that its Fermi level is slightly (∼0.1 eV) above the center of its band gap. The work function of gold is 5.1 eV [167]. The band line up analysis of UO_3 and gold suggests that a Schottky contact is formed, as shown in Figure 26. The formation of a Schottky barrier between gold and UO_3 has also been supported in the literature (Figure 27).

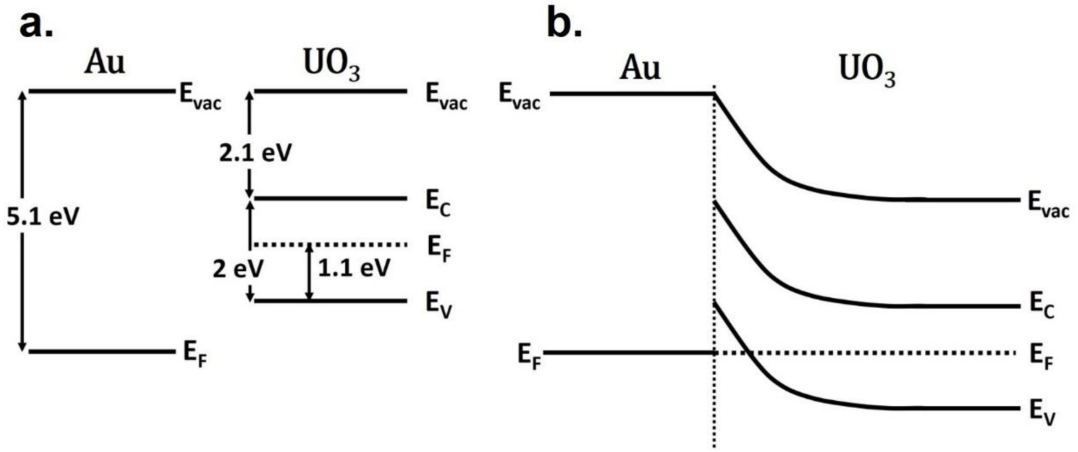

Figure 26. Band line up of gold and UO_3 (a) when they are apart, and (b) when they are in contact.

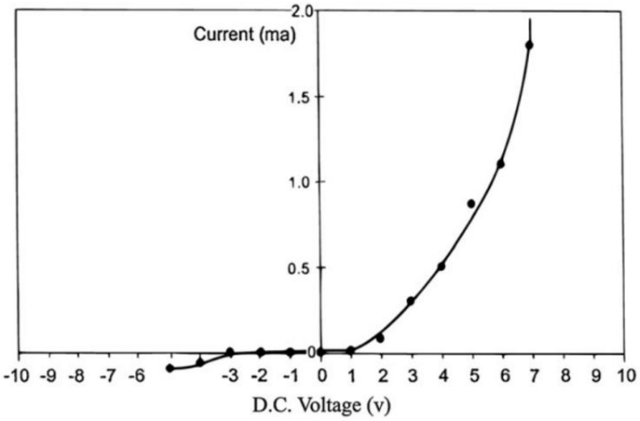

Figure 27. *I–V* characteristics of a Schottky diode made from UO_3 using gold as contacts [168] (Reprinted from Vacuum, 83/1, T.T. Meek and B. von Roedern, Semiconductor devices fabricated from actinide oxides, 226–228, Copyright (2008), with permission from Elsevier)

It has been reported in the literature that gold films that are sufficiently thin (nm in thickness) exhibit some optical transparency (Figure 28) [169]. Gold films of different thicknesses (a few tens of nm) were deposited on a glass substrate by evaporation, and their transmittance and resistivity were determined to find an appropriate trade-off between these two quantities. The best combination was found for a gold film of 25 nm thickness, which showed a transmittance of about 13% (Figure 29) at 351 nm (wavelength of light used for the experiment) with a resistance of 5 Ω, measured diagonally on the surface.

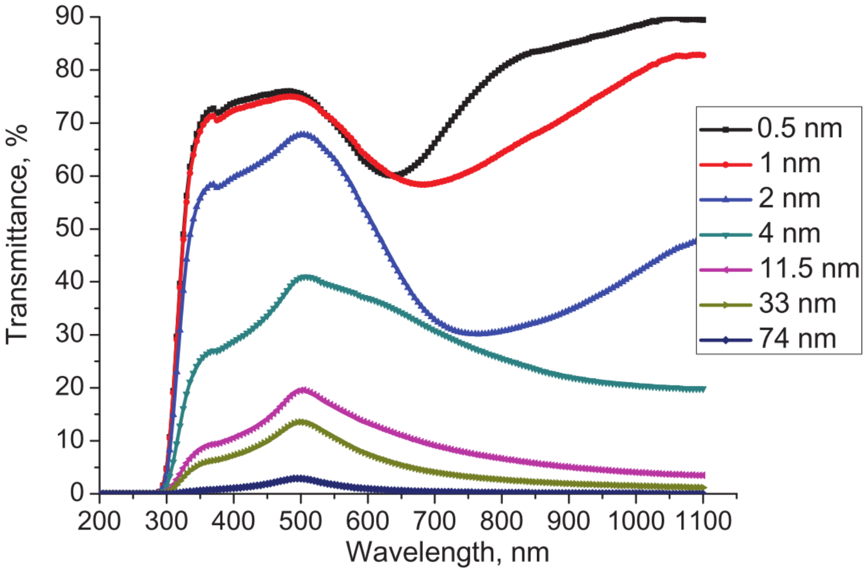

Figure 28. Transmittance of thin gold films deposited by thermal evaporation [169] (Reprinted from Physics Procedia, 32, A. Axelevitch, B. Gorenstein, and G. Golan, Investigation of Optical Transmission in Thin Metal Films, 1–13, Copyright (2012), with permission from Elsevier)

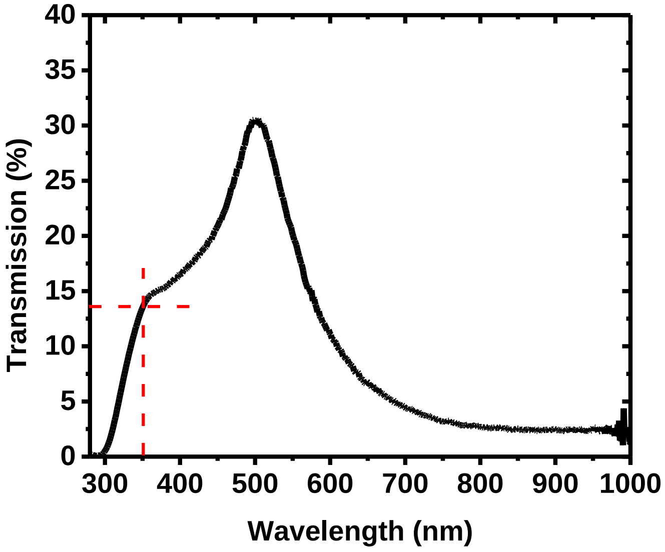

Figure 29. Transmittance of a 25 nm thick gold film deposited by resistive heating.

3.8.3.3. ToF Photoconductivity Experiment

A COMPexPro 100 pulsed laser source (351 nm wavelength) was used to generate pulses of 20 ns duration at a frequency of 1 Hz. A sample was mounted in a sample holder and covered with a lid that had a small hole for the laser to pass through. The sample holder was placed in the path of the laser on an optical post. The bias voltage to the sample was provided with a Bertan Associates Inc. Model 210-10R High Voltage Power Supply from a few hundred volts to a few kilovolts in steps of 100 V. The photocurrent signal obtained from the sample was processed with an R&S HMO 1202 oscilloscope after using a Femto DHPCA-100 transimpedance amplifier to enhance the signal.

3.9. Mobility–Lifetime Measurements (UMKC)

Mobility–lifetime ($\mu\tau$) values can be obtained through a Hecht analysis of the data obtained from two experiments: steady-state photoconductivity and ToF photoconductivity.

3.9.1. Theory

At a certain applied voltage, a semiconductor shows some finite current in the dark. The current increases when the sample is irradiated with light of suitable wavelength since it causes excitation of additional charge carriers in the semiconductor. The difference in the current through the material in the presence and absence of light gives the photocurrent. When the electric field applied across the material is low, the excited charge carriers get trapped before travelling sufficient distance, and hence the photocurrent is low. As the electric field is increased, the excited charge carriers travel longer distances before being trapped, and hence the photocurrent increases linearly with electric field up to a certain value. Finally, when the electric field becomes high enough to sweep away the maximum number of charge carriers before being trapped, the photocurrent saturates [170]. The current profile is described by the Hecht equation [171]:

$$I = I_0 \frac{\mu\tau V}{d^2}\left[1 - \exp\left(-\frac{d^2}{\mu\tau V}\right)\right] \tag{3.47}$$

where, I_0 is the maximum photocurrent, V is the applied voltage and d is the thickness of the sample.

A plot of applied voltage and the resulting photocurrent is fitted to Equation (3.47) to obtain $\mu\tau$. There are two ways of obtaining the data for this analysis: ToF photoconductivity and steady-state photoconductivity. A schematic of the experimental set up for the steady-state photoconductivity experiment is shown in Figure 30.

3.9.2. Mobility–Lifetime from ToF Photoconductivity: Theory

The transient current data obtained from the ToF photoconductivity experiment (described in **Section 3.8.3**) can be integrated over the transit time to obtain the total charge (Q) collected during that period. The process can be repeated for a series of measurements corresponding to different voltages, which will give the total charge collected as a function of applied biasing voltage. The data can then be fitted to Hecht's charge equation:

$$Q = Q_0 \frac{\mu\tau V}{d^2}\left[1 - \exp\left(-\frac{d^2}{\mu\tau V}\right)\right] \tag{3.48}$$

where, Q_0 is the maximum charge collected.

3.9.3. Mobility–Lifetime from Steady-State Photoconductivity: Experiment

The experiment was done by measuring the current through a sample as a function of voltage with and without light in alternate steps. An OBB Powerarc light source was used to irradiate the sample with a white light. The sample was prepared by depositing a transparent gold contact (and a non-transparent gold contact) and mounting in a sample holder with a cover that had a small hole to allow light to pass through. A LabView-based program was used to acquire data in the dark and in the light at each individual voltage step. For the voltage range 0–200 V, a Keithley 2400 sourcemeter was used to source the voltage across the sample and the resulting current was measured with a Keithley 6485 picoammeter. For higher voltage measurements, the circuit and devices described in **Section 3.8.2** were used.

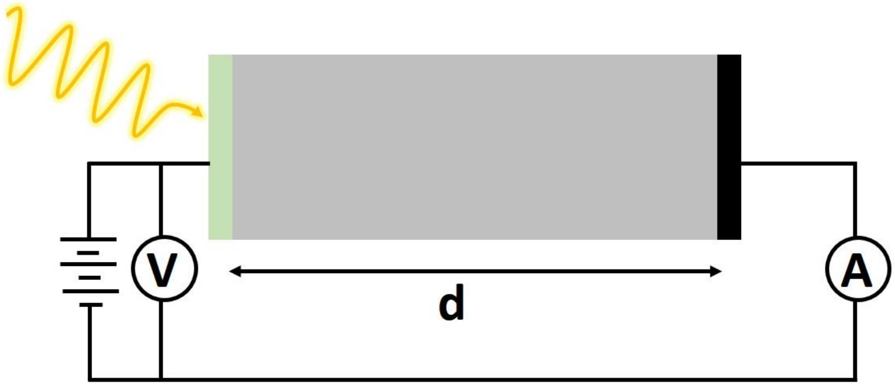

Figure 30. Schematic of the experimental set-up for steady-state photoconductivity.

CHAPTER 4. RESULTS AND DISCUSSIONS: U_3O_8

One of the objectives of this work was to fabricate samples of U_3O_8 and study their basic physical/chemical and electrical properties as a function of fabrication conditions. The goal was to alter the electrical properties of U_3O_8 by changing the sample fabrication conditions to explore the possibility of tuning those properties. As a starting point, the most practical option of obtaining the samples was to fabricate pressed pellets of U_3O_8, since it is easier to fabricate pellets compared to other sample forms such as thin films and single crystals.

The resistivity of U_3O_8 has been reported to be in the range of 10^3–10^5 Ω-cm [66] and the charge carrier mobility has been reported to be on the order of 1 $cm^2 \cdot V^{-1} \cdot s^{-1}$ [65], [67]. Our goal was to first reproduce these results on our samples and then optimize these properties. Here, we will discuss the results of our experiments and other relevant information on U_3O_8.

4.1. Stoichiometric U_3O_8 Sample Preparation

U_3O_8 powder was prepared from uranyl acetate dihydrate by heating to 650 °C for 90 minutes in a tube furnace. The powder was then loaded into a die (die A) and pressed using a uniaxial press at 5–8 ksi for 1 minute to obtain pellets, which were then sintered at 1350 °C for 1–20 hours, to obtain stoichiometric samples. Most pellets fabricated in this way lacked a consistently smooth surface, attributed to the faults of the die. Therefore, a different die (die B) was used, which overcame the deficiencies of die

A, and samples with smooth surfaces were obtained. The sintering times and densities of samples fabricated using dies A and B are shown in Table 9 and Table 10 respectively. The sintered pellets were approximately 1 mm thick with a 9.5–11 mm diameter.

Table 9. Sintering time and density of stoichiometric U_3O_8 pellets fabricated using die A.

Sample	**Sintering time (hours)**	**Density ($g \cdot cm^{-3}$)**	**% Theoretical Density**
A0101	1	–	–
A0102	1	–	–
A0103	1	7.80	94.0
A0104	1	8.04	96.9
A0105	1	7.84	94.5
A0401	4	7.58	91.3
A0402	4	7.71	92.9
A0403	4	7.77	93.6
A0601	6	7.64	92.0
A0602	6	7.42	49.4
A0603	6	7.71	92.9
A0604	6	7.66	92.3
A0801	8	6.74	81.2
A0802	8	7.87	94.8
A0803	8	7.62	91.8
A0804	8	7.89	95.1
A0804	8	7.89	95.1
A1001	10	7.69	92.7
A1002	10	7.57	91.2

Sample	Sintering time (hours)	Density ($g \cdot cm^{-3}$)	% Theoretical Density
A1003	10	7.48	90.1
A1004	10	7.55	91.0
A1201	12	7.89	95.1
A1202	12	7.81	94.1
A1203	12	7.75	93.4
A1204	12	8.10	97.6
A1205	12	8.16	98.3
A1206	12	7.98	96.1
A1207	12	8.10	97.6
A2001	20	–	–
A2002	20	7.93	95.5
A2003	20	–	–

Table 10. Sintering time and density of stoichiometric U_3O_8 pellets fabricated using die B.

Sample	**Sintering time (hours)**	**Density ($g{\cdot}cm^{-3}$)**	**% Theoretical Density**
101	1	7.99	96.3
102	1	8.12	97.8
103	1	8.07	97.3
104	1	7.99	96.4
201	2	7.96	95.9
202	2	7.84	94.5
203	2	–	–
204	2	8.10	97.6
301	3	7.91	95.3
302	3	8.03	96.8
401	4	8.00	96.4
402	4	8.14	98.0
403	4	8.18	98.6
404	4	8.16	98.3
501	5	7.96	96.0
502	5	8.08	97.3
503	5	–	–
504	5	8.05	96.9
602	6	–	–
603	6	–	–
701	7	7.41	89.3
702	7	7.83	94.3
703	7	8.16	98.3

Sample	**Sintering time (hours)**	**Density ($g \cdot cm^{-3}$)**	**% Theoretical Density**
704	7	8.04	96.9
801	8	7.98	96.2
802	8	–	–
803	8	–	–
804	8	–	–
901	9	8.00	96.4
902	9	8.06	97.1
903	9	8.10	97.5
904	9	–	–
1001	10	7.96	95.9
1002	10	7.94	95.7
1003	10	7.73	93.2
1004	10	8.06	97.1

4.2. Basic Characterization

4.2.1. Density of Stoichiometric U_3O_8 Samples

The density of stoichiometric U_3O_8 samples was determined by measuring the relative change in the weight of the samples in air versus deionized water. The percentage theoretical density of each U_3O_8 sample was determined based on the theoretical density of the α-U_3O_8 phase, i.e., 8.30 $g \cdot cm^{-3}$ [104]. The density of pellets before sintering was 45–50% of the theoretical density of α-U_3O_8. The pellets achieved a near full densification (∼95% of theoretical density) upon sintering at 1350 °C for as little as one hour. No trends were observed between sintering times and density of the U_3O_8 samples, as shown in Figure 31. The error bars represent the standard deviation of the density values of the samples sintered for the same duration.

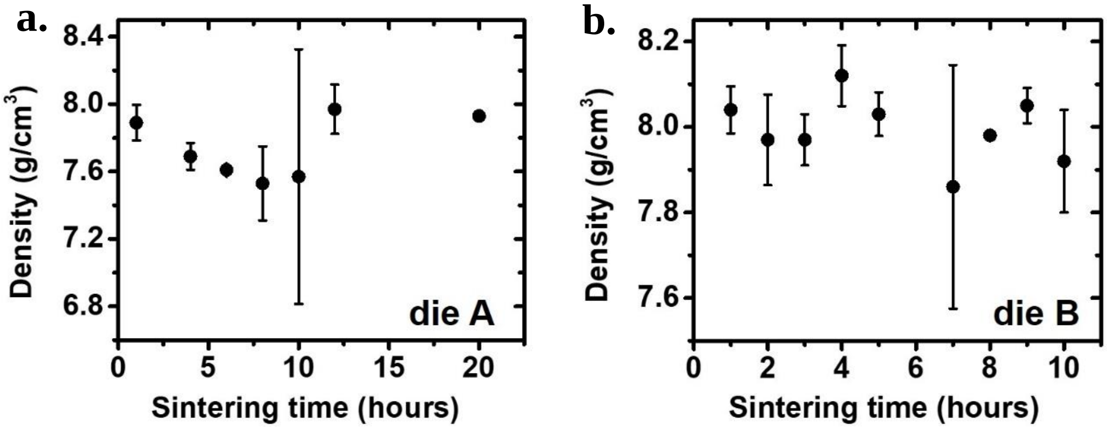

Figure 31. Density of the stoichiometric U_3O_8 samples as a function of sintering times (a) pellets fabricated with die A (b) pellets fabricated with die B.

4.2.2. Microstructure of Stoichiometric U_3O_8 Samples

Since charge carriers can be scattered by boundaries, the grain sizes present within samples can have a significant influence on electrical resistivity and charge carrier mobility in a polycrystalline semiconductor [32]. The microstructure of the U_3O_8 pellets was studied by the Heyn lineal intercept procedure on multiple fields of view for digital micrographs of the sample surfaces.

Figure 32 illustrates the correlation between grain size and sintering times, with average grain size increasing from $\sim 23\ \mu$m to $\sim 40\ \mu$m for sintering times between 1 and 10 hours. The error bars represent the standard deviation of the grain size values obtained from different micrographs of a particular sample.

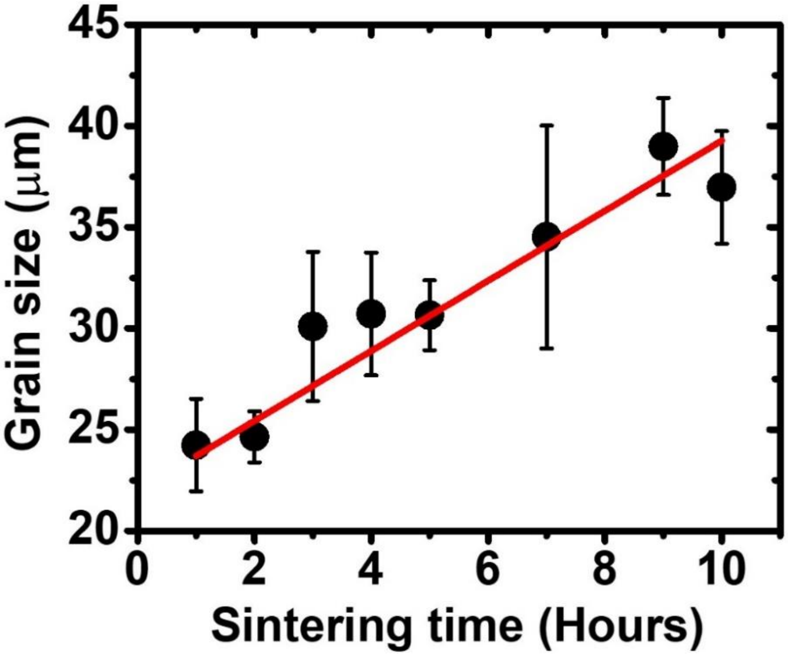

Figure 32. Average grain size of stoichiometric U_3O_8 pellets as a function of sintering time.

4.2.3. X-ray Diffraction of Stoichiometric U_3O_8 Samples

The U_3O_8 powder obtained by heating uranyl acetate dihydrate was verified as α-U_3O_8 by powder x-ray diffraction. Additionally, the x-ray diffraction analysis performed on a test sample (pellet) of U_3O_8 was found to be consistent with the α-U_3O_8 phase (Figure 33).

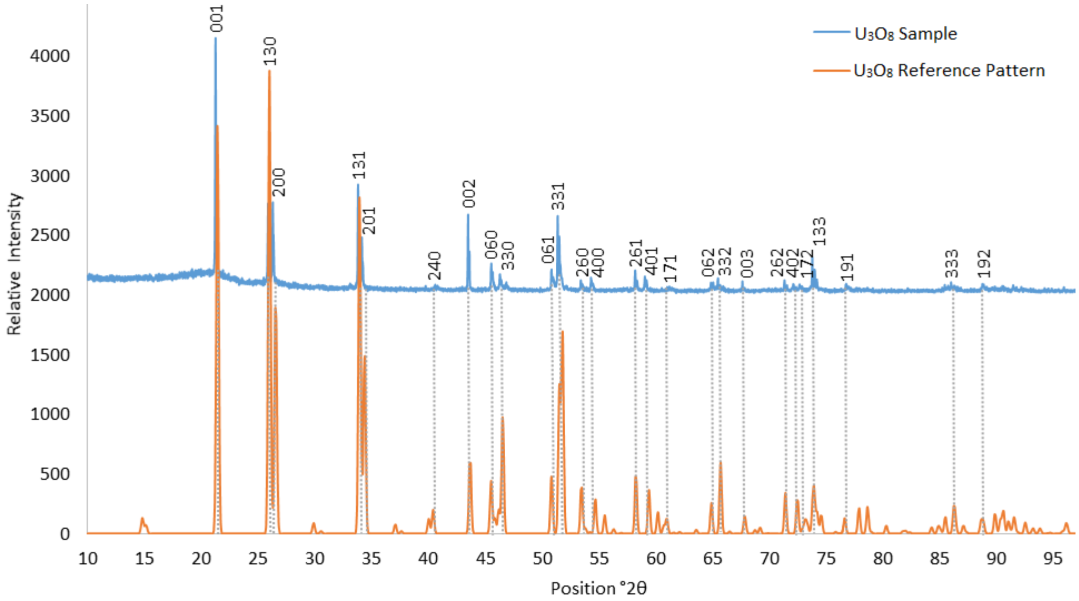

Figure 33. X-ray diffraction spectra for a stoichiometric U_3O_8 pellet sintered at 1350 °C for 12 hours.

4.3. Resistivity of Stoichiometric U_3O_8 Samples

The resistivity values of the U_3O_8 samples were measured by current–voltage measurements using different methods including van der pauw, four point linear, and metal–insulator–metal configurations. These experiments were done on a subset of the samples with slight variations to verify the reproducibility of the data and identify the most suitable method. A summary of all of the resistivity measurements on the U_3O_8 samples is given in Table 11. The resistivity values obtained from van der Pauw measurements using different probe configurations (tungsten probes, gold probes, or gold probes contacted to silver paint dots) are very close. Further, the resistivity value measured by the linear four-point method for sample A1203 is also close to that measured by the van der Pauw method. Metal–insulator–metal (MIM) measurements completed with a dielectric test fixture yielded resistivity values higher than for the other methods, owing we believe to the parallel plate electrodes not making complete contact to the rough surfaces of the pellets, thereby leading to an overestimation of resistivity. Therefore, although this is an efficient non-destructive measurement method, it is likely unreliable. MIM measurements done with a guard ring structure were within an order of magnitude (both higher and lower) of those done without the guard ring, which suggests a possible, though small, surface current contribution. Overall, the measurements are generally consistent and reproducible, other than those performed with the dielectric test fixture.

The *I*–*V* measurements yielded straight lines, indicating ohmic injection for the various contacts used, at least at low-to-moderate electric field values, as shown in Figure 34. Additional *I*–*V* plots of the U_3O_8 samples are provided in APPENDIX B. The overall resistivity was found to be on the order of 10^2–10^4 Ω-cm, which agrees with the literature [66]. No clear correlation between resistivity and pellet properties (e.g., sintering time, density, grain size) was observed, as shown in Figure 35 and Figure 36. For Figure 36, the error bars represent the standard deviation of the resistivity values of the samples sintered for the same duration.

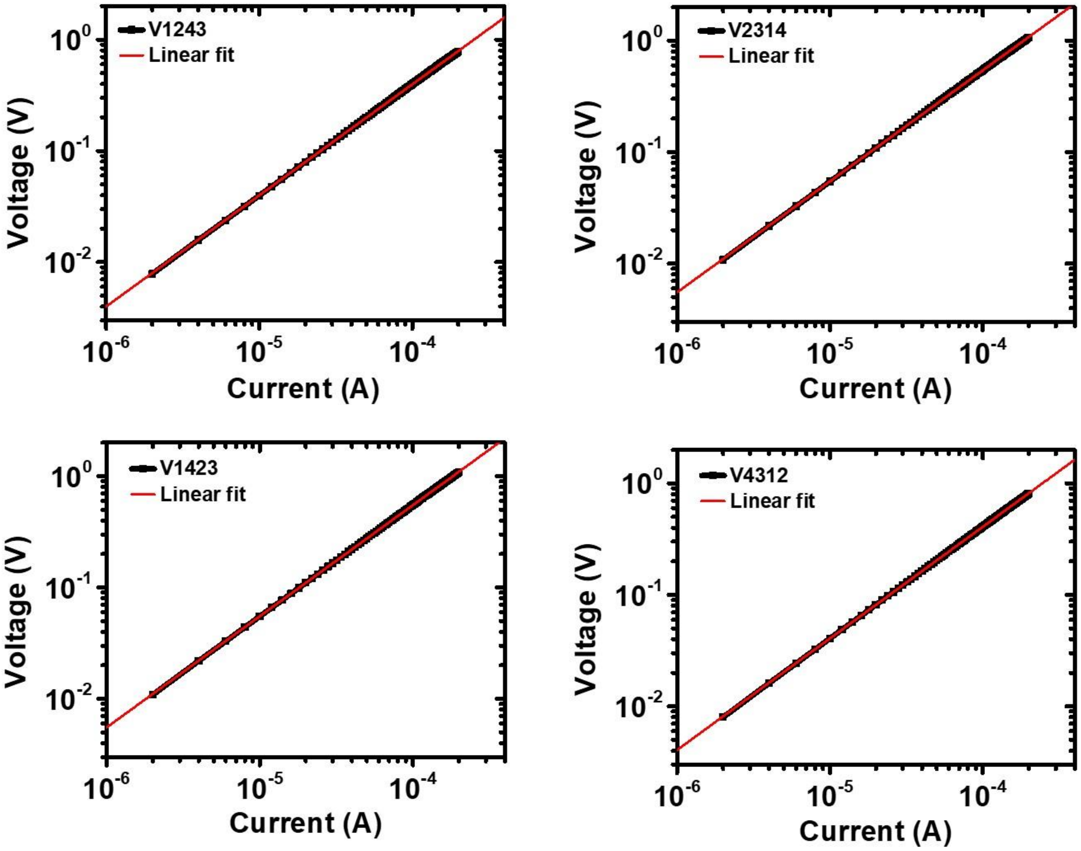

Figure 34. Results of 4-point *I*–*V* measurements on sample A0403.

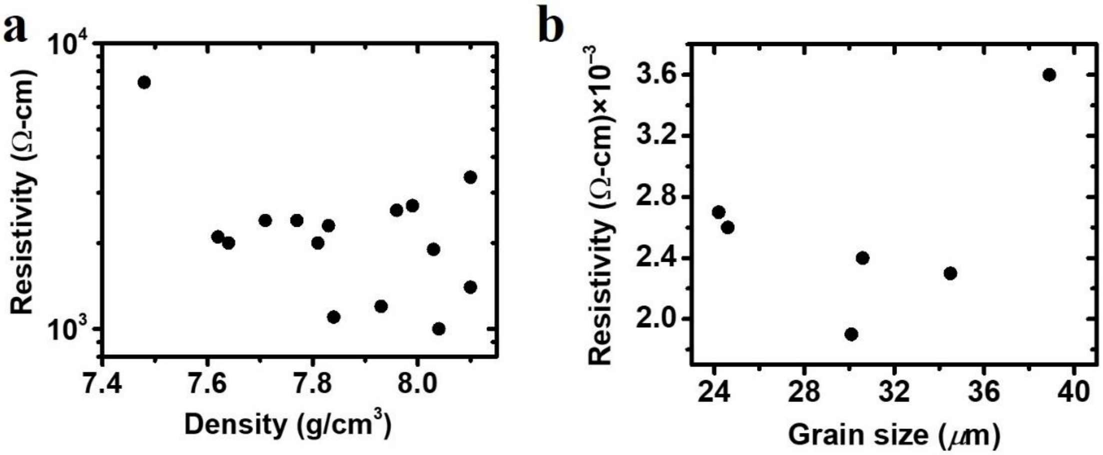

Figure 35. Resistivity of stoichiometric U_3O_8 samples (a) as a function of density (b) as a function of grain size.

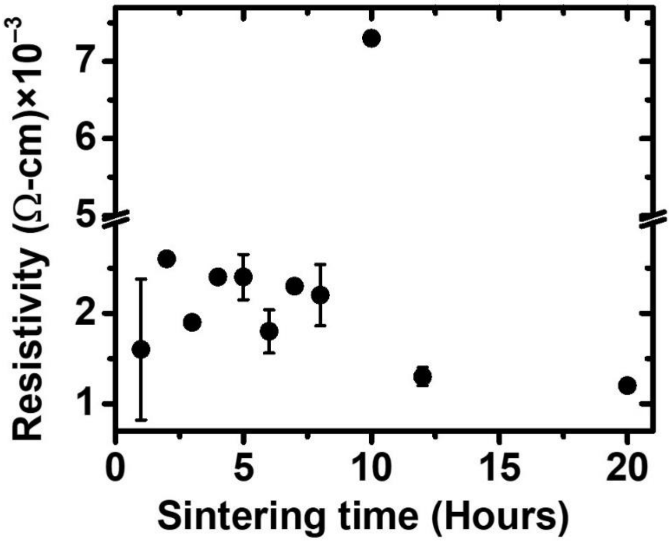

Figure 36. Resistivity of stoichiometric U_3O_8 samples as a function of sintering time.

Table 11. Resistivity of stoichiometric U_3O_8 samples.

Sample	Resistivity (Ω-cm)					
	1	2	3	4	5	6
A0101	4.2×10^{2}	–	–	–	1.8×10^{4} *	2.3×10^{4}
A0102	–	–	–	–	1.7×10^{5} *	–
A0103	5.4×10^{2}	–	–	–	1.3×10^{4} *	1.0×10^{4}
A0104	–	–	1.0×10^{3}	–	–	–
A0105	–	–	1.1×10^{3}	–	–	–
A0402	–	–	2.4×10^{3}	–	1.5×10^{4} **	8.4×10^{3}
A0403	2.9×10^{3}	–	2.4×10^{3}	–	–	–
A0601	–	–	2.0×10^{3}	–	1.2×10^{4}	6.1×10^{3}
A0603	2.2×10^{3}	–	–	–	–	–
A0803	–	–	2.1×10^{3}	–	2.9×10^{3} **	5.3×10^{3}
A0804	1.8×10^{3}	–	–	–	–	–
A1003	–	–	7.3×10^{3}	–	–	–
A1004	8.3×10^{2}	–	–	–	–	–
A1202	–	–	2.0×10^{3}	–	–	–
A1203	5.4×10^{2}	5.4×10^{2}	–	6.5×10^{2}	1.8×10^{3} **	1.3×10^{4}
A1207	–	–	1.4×10^{3}	–	–	–
A2002	–	–	1.2×10^{3}	–	–	–
104	–	–	2.7×10^{3}	–	–	–
203	–	–	2.6×10^{3}	–	–	–
302	–	–	1.9×10^{3}	–	–	–
501	–	–	2.6×10^{3}	–	–	–
503	–	–	2.1×10^{3}	–	–	–
702	–	–	2.3×10^{3}	–	–	–

Sample	**Resistivity (Ω-cm)**					
	1	**2**	**3**	**4**	**5**	**6**
802	–	–	1.9×10^3	–	–	–
804	–	–	2.7×10^3	–	–	–
903	–	–	3.4×10^3	–	–	–
904	–	–	3.9×10^3	–	–	–
602	–	–	1.7×10^3	–	–	–
603	–	–	1.5×10^3	–	–	–

1. van der Pauw with gold probes; 2. van der Pauw with silver paint and gold probes; 3. van der Pauw with tungsten probes; 4. four-point collinear; 5. MIM; 6. MIM with guard ring; * using dielectric fixture; ** using silver paint.

4.4. Nonstoichiometric U_3O_8 Sample Preparation

Nonstoichiometric U_3O_8 (i.e., $U_3O_{8\pm x}$) samples were obtained by altering the oxygen available in the tube furnace during powder preparation and subsequently while sintering the pellets. The oxygen concentrations used were ~21% (air), 12%, and 30%. The latter two oxygen environments were provided by supplying a gas mixture of O_2 and Ar. The pressed pellets were again exposed to the same oxygen environment during sintering. The sintering was carried out at 1000 °C due to temperature limitations in the tube furnace (different from the one used for the stoichiometric sample). A small variation was observed in the stoichiometry of the samples as a function of the oxygen environment (**Section 4.5.3**). The fabrication conditions and the properties of nonstoichiometric samples are listed in Table 12.

Table 12. Resistivity and stoichiometry of non-stoichiometric U_3O_8 sintered at 1000 °C in varying oxygen environment.

Sample	**Time (Hours)**	**% O_2**	**Stoichiometry ($U_3O_{8\pm x}$) x =**	**Density (g.cm^{-3})**	**% Theoretical density**	**Grain size (μm)**	**Resistivity (Ω-cm)**
N04A01	4	Air	< ±0.001	7.13	85.9	4.2	9.8×10^{2}
N08A01	8	Air		6.89	83.0	5.4	1.0×10^{3}
N20A01	20	Air		7.68	92.5	–	7.2×10^{2}
N20A02	20	Air		7.71	92.9	8.3	7.2×10^{2}
N20A03	20	Air		7.74	93.2	–	6.7×10^{2}
N041201	4	12	–0.0081±0.0004	7.76	93.5	2.7	6.1×10^{2}
N041202	4	12		8.02	96.7	–	6.6×10^{2}
N081201	8	12		7.92	95.4	3.4	6.6×10^{3}
N081202	8	12		6.45	77.7	3.1	8.8×10^{2}
N201201	20	12		7.96	95.9	8.5	7.0×10^{2}
N201202	20	12		7.90	95.2	–	5.1×10^{2}
N201203	20	12		7.91	95.3	8.6	5.9×10^{2}
N043001	4	30	0.0091±0.0010	7.68	92.5	–	6.9×10^{2}
N043002	4	30		7.88	95.0	–	6.9×10^{2}
N043003	4	30		7.72	93.0	4.6	7.3×10^{2}
N083001	8	30		8.01	96.5	4.0	7.8×10^{2}
N203001	20	30		8.00	96.3	9.0	4.6×10^{2}

4.5. Basic Characterization

4.5.1. Density of Non-Stoichiometric U_3O_8 Samples

The density of nonstoichiometric U_3O_8 samples was measured in the same way as that of stoichiometric samples. The density values of the non-stoichiometric U_3O_8 samples are listed in Table 12. Figure 37 shows the density of the samples sintered with and without oxygen conditioning. It is evident that without oxygen conditioning, the lower sintering temperature does not yield fully dense (~95% theoretical density) samples as in the case of stoichiometric samples (**Section 4.2.1.**), although the density does approach close to this value with longer sintering times. Oxygen conditioning, however, yielded much higher density pellets (~95% theoretical density) even for short sintering times. The difference in the sintering behavior of these pellets could potentially be due to the presence of the inert environment during oxygen conditioning (i.e., not containing moisture and other gases). The samples prepared in air should in theory show the same characteristics as the stoichiometric samples (due to sample preparation/sintering without oxygen conditioning) and sinter to near full densities in a much shorter duration. However, we do not observe this which could potentially be due to the lower sintering temperature of these samples.

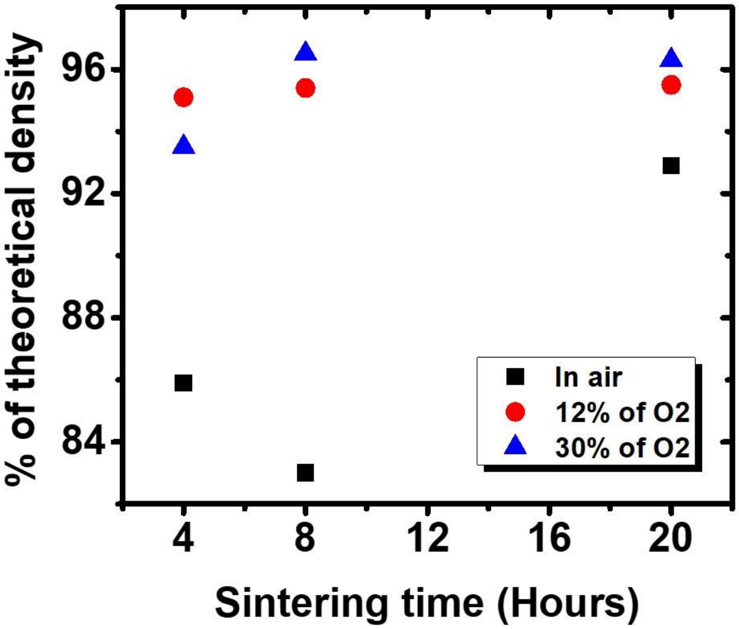

Figure 37. Density of $U_3O_{8\pm x}$ sintered at 1000 °C for different durations

4.5.2. Microstructure of Non-Stoichiometric U_3O_8 Samples

The $U_3O_{8\pm x}$ pellets were polished as described in **Section 3.3.4** and the microstructure was studied in the same way as for stoichiometric U_3O_8.

Table 12 shows the grain size of nonstoichiometric $U_3O_{8\pm x}$ as a function of sintering time for different oxygen environments during sintering. It is seen that the grain sizes generally increase with sintering time. For lower sintering times (4 and 8 hours), the grain size of the samples sintered in different oxygen environments differ noticeably whereas for 20 hours of sintering time, the grain sizes are almost the same regardless of the oxygen environment. It is seen that the grain size values of the samples prepared in air are significantly smaller that those described in **Section 4.2.2**. This is likely due to the lower sintering temperatures used. This suggests that both sintering time and temperature influence the grain size.

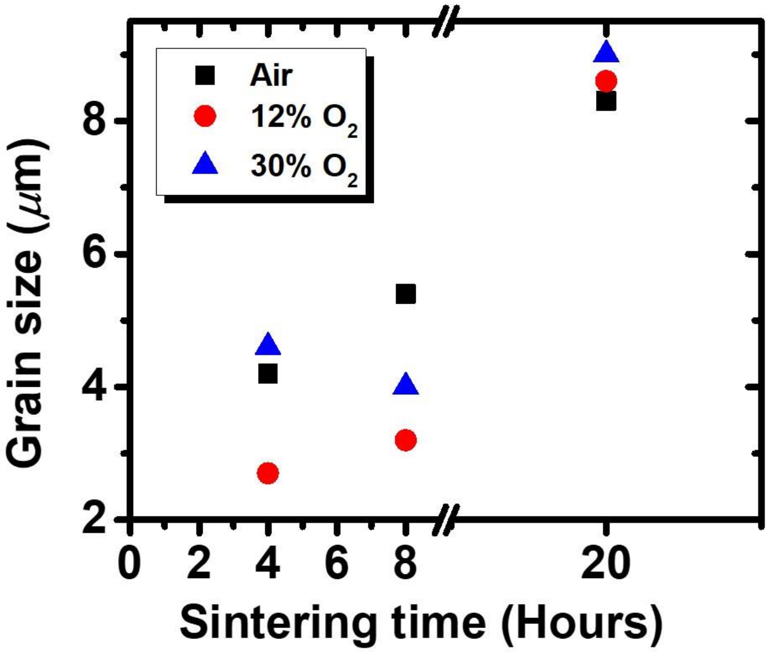

Figure 38. Grain size of nonstoichiometric $U_3O_{8\pm x}$ as a function of sintering time for different oxygen environments.

4.5.3. Stoichiometry of Non-Stoichiometric U_3O_8 Samples

The stoichiometry of the $U_3O_{8\pm x}$ samples was measured using potentiometric titration as described in **Section 3.3.2.1**. The stoichiometry values of the $U_3O_{8\pm x}$ samples are listed in Table 12. It was found that the pellets sintered using 12% O_2 exhibited a composition of $U_3O_{8\pm x}$ with $x = -0.0081 \pm 0.0004$ (hypostoichiometric samples) and those sintered using 30% O_2 exhibited $U_3O_{8\pm x}$ with $x = 0.0091 \pm 0.0010$ (hyperstoichiometric samples). On the other hand, pellets sintered in air (~21% O_2)

showed no measurable deviation from stoichiometry (i.e., they were stoichiometric samples). As expected, the stoichiometry of the pellets varied depending on the amount of oxygen available during sample preparation.

4.5.4. Resistivity of Non-Stoichiometric U_3O_8 Samples (UTK)

The resistivity of the $U_3O_{8\pm x}$ samples was evaluated at UTK using a commercial linear four-point probe system. Each sample was placed inside the probe system with the four probes of the system touching the surface of the sample. Then current was sourced from the outer probes and the voltage across the inner probes was measured. The resulting current–voltage graph was used to determine the resistivity values, which are shown in Table 12. No discernible trend was observed between resistivity and the grain size (Figure 39).

The resistivity values of nonstoichiometric samples were found to be on the order of 10^2–10^3 Ω-cm, similar to the values obtained for stoichiometric samples. The samples that were exposed to air during sintering have resistivity values 6.7×10^2–1.0×10^3 Ω-cm, those exposed to 30% of oxygen have resistivity values 4.6×10^2–7.8×10^2 Ω-cm, and most of those exposed to 12% of oxygen have resistivity values 5.1×10^2–8.8×10^2 Ω-cm, with one outlier sample (N081201) exhibiting a resistivity of 6.6×10^3 Ω-cm. No obvious trend was observed between the resistivity and stoichiometry of these samples, when the resistivity values of all of the samples were considered, as shown in Figure 40 (a). However, if we omitted the resistivity value of the outlier sample, we saw that any deviation from stoichiometry (whether hypo- or hyper-) tends to decrease the resistivity of these samples, as shown in Figure 40 (b). The decrease in resistivity of hypostoichiometric U_3O_8 has also been reported in the literature [67]. However, since our sample size is small and the variations in the resistivity are within the error, additional studies will be required to validate this observation. The error bars represent the standard deviation of the resistivity values measured on multiple samples prepared under identical conditions.

The correlation between the resistivity and the stoichiometry of U_3O_8 is in complete contrast to the case of UO_2, in which the resistivity increases for both hyperstoichiometric and hypostoichiometric sample [36], [42], [44]. Similarly, the (lack of) correlation between the resistivity and the grain size of U_3O_8 is also in contrast with the case of UO_2, in which the resistivity is affected significantly by its grain size [45].

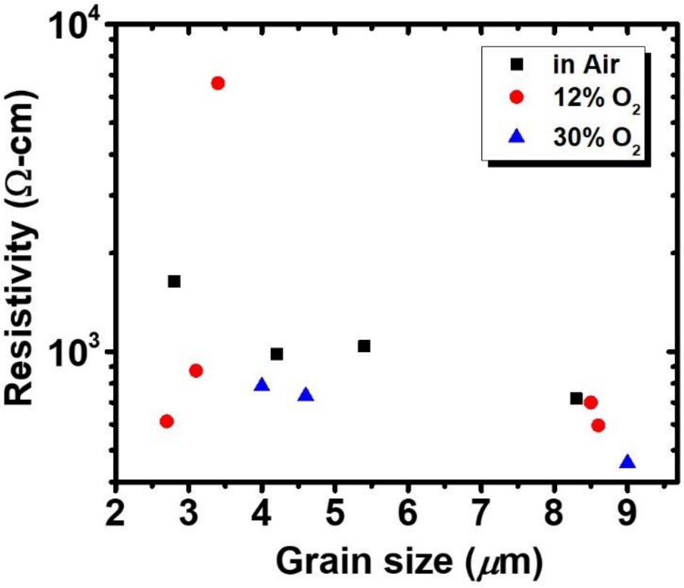

Figure 39. Resistivity of $U_3O_{8\pm x}$ samples as a function of grain size.

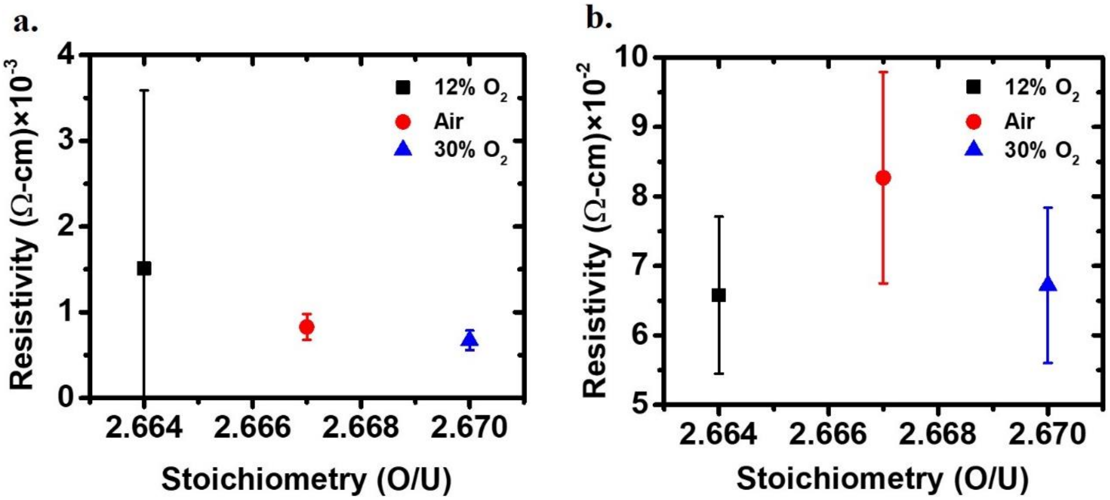

Figure 40. Resistivity as a function of stoichiometry of nonstoichiometric $U_3O_{8\pm x}$ samples: (a) when all the resistivity values are considered. (b) when the outlier value of resistivity is left out.

4.6. Charge Carrier Mobility: Hall Effect Measurements

Our attempts to measure the charge carrier mobility of the U_3O_8 samples by the Hall effect method were not successful due to a lack of discernible Hall voltage. The experiment was tried on more than 15 samples, but none resulted in a measurable signal. The results of the Hall effect measurements on two representative samples are shown in Figure 41 and the remaining results are shown in APPENDIX C. Based on the lack of signal, we can estimate the charge carrier mobility to be less than 1 $cm^2 \cdot V^{-1} s^{-1}$, since this represents the lower limit of mobility that can be measured with this technique. The value of charge carrier mobility of less than 1 $cm^2 \cdot V^{-1} \cdot s^{-1}$ agrees with the literature reported values [65], [67].

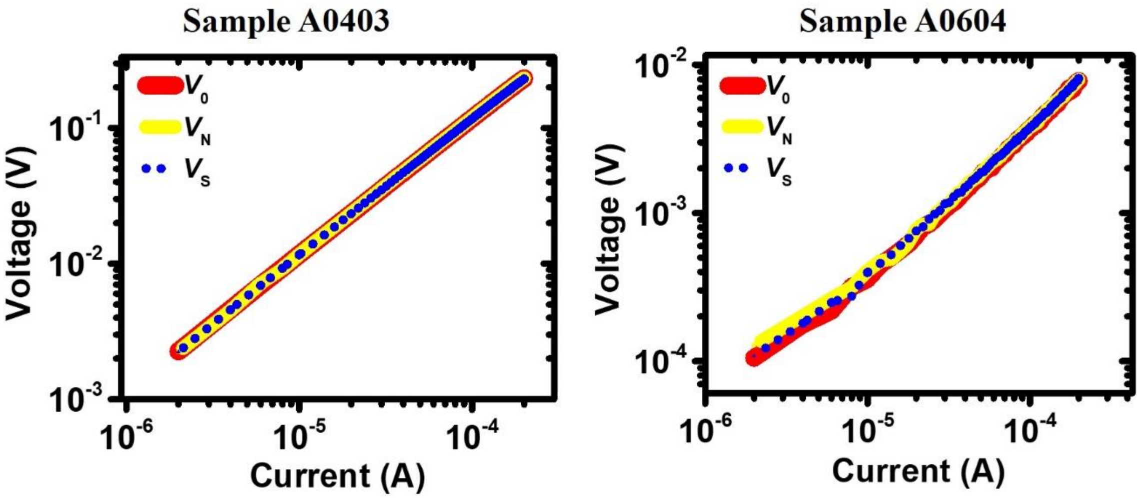

Figure 41. Results of Hall effect measurements showing no discernible Hall voltage.

4.7. Summary

Stoichiometric α-U_3O_8 pellets were prepared by uniaxial hot pressing of U_3O_8 powder followed by sintering at 1350 °C. The resistivity values of these pellets were found to be on the order of 10^2–10^4 Ω-cm, with no clear correlation between the resistivity and the sample properties and/or fabrication conditions. The values of average grain size of these pellets were found to increase with sintering time.

Non-stoichiometric U_3O_8 pellets were prepared by exposing U_3O_8 powder to different oxygen environment and sintering the pellets in the same oxygen environment. It was found that the pellets processed in 12% of O_2 produced hypostoichiometric samples (O/U = 2.664), the pellets processed in 30% of O_2 produced hyperstoichiometric samples (O/U = 2.670), and the pellets processed in air showed no measurable variation of stoichiometry (O/U = 2.667). The overall resistivity values of the hyperstoichiometric samples were on the order of 10^2 Ω-cm and those of the stoichiometric samples were on the order of 10^2–10^3 Ω-cm. The resistivity values of the hypostoichiometric samples were mostly on the order of 10^2 Ω-cm with one outlier sample having a resistivity of 6.6×10^3 Ω-cm. If we left out the outlier sample, we saw that the resistivity of the nonstoichiometric U_3O_8 sample is smaller than that of the stoichiometric sample.

The charge carrier mobility measurement experiments using the DC Hall effect method showed no measurable Hall voltage. Based on the lack of a measurable signal, the charge carrier mobility was estimated to be less than 1 $cm^2 \cdot V^{-1} \cdot s^{-1}$. Since the initial goal was to maximize the resistivity of U_3O_8 and the overall resistivity was found to be low, further study of U_3O_8 was suspended.

Since both the resistivity and the charge carrier mobility of U_3O_8 are below the “target” values, they must be improved to consider it for direct-conversion neutron detection. In addition, other charge transport properties such as lifetime, and mobility–lifetime of charge carriers should be determined. Future studies should explore ways to increase both the charge carrier mobility and resistivity by using methods such as doping and specialized sample fabrication techniques. Samples should be fabricated with wider variations in stoichiometry and/or microstructure to study their effects on the electrical properties. Additionally, the characteristics/structure of the metal–U_3O_8 interface should be studied, which will be essential for semiconductor device fabrication.

CHAPTER 5. RESULTS AND DISCUSSIONS: UO_3

We shifted our focus towards the study of UO_3 after the research on U_3O_8 was suspended. Due to a lack of established method to fabricate UO_3 samples, we planned to fabricate pellets of UO_3 as a first step.

We explored different ways to fabricate the pellets of UO_3, which included heating UO_3 powder and hot-pressing the powder to obtain pellets. Several trial and errors were required to figure out the correct range of temperatures for both heating the powder and pressing the pellets. The pellets thus fabricated were studied for basic properties as well as electrical and electronic properties. Here, we will discuss the results of our experiments and other relevant information on UO_3.

5.1. UO_3 Sample Preparation

In early experiments, UO_3 pellets were fabricated by uniaxial hot pressing of UO_3 powder, obtained by heating uranyl nitrate hexahydrate at 400 °C for 60 hours. A load of 2–4 tons was applied for 10–30 minutes during pellet pressing. The UO_3 powder obtained from uranyl nitrate hexahydrate was confirmed to be γ-UO_3 from powder x-ray diffraction (PXRD), however, the pellets fabricated from this powder were of low quality (such as low density, and forming hydrates rapidly), potentially due to impurities present in trace quantities, which went undetected in the PXRD results. Therefore, commercially available UO_3 powder was used in the next phase.

UO_3 pellets were fabricated from commercial UO_3 powder with and without powder conditioning. The powder was conditioned by heating to 200–480 °C for 1–60 hours in the presence of gas mixtures consisting of 5–92% oxygen/argon. The conditioned powder generally became orange in appearance at temperatures below 400 °C, consistent with the literature [74], [172]. When heated to 480 °C, a brown colored powder was observed, likely indicating a change in the UO_3 phase or phases present. The pellets that were fabricated without powder conditioning were pressed at 200–250 °C for 10–20 minutes with 2– 8 tons of load, whereas those fabricated from conditioned powder were pressed at 180–200 °C for 10–45 minutes with 4.5–6 tons of load. The fabrication conditions and the properties of the UO_3 samples are listed in Table 13.

Table 13. Processing conditions and properties of UO_3 samples.

Sample	**Powder conditioning**			**Hot pressing conditions**			**Density ($g\cdot cm^{-3}$)**	**% of theoretical density (1)**	**% of theoretical density (2)**	**Grain size (μm)**	**O:U (3)**	**O:U (4)**
	% O_2	**Temp. (°C)**	**Time (Hrs)**	**Temp. (°C)**	**Time (min)**	**Load (tons)**						
100.10.2	–	–	–	100	10	2	–	–	–	–	–	–
250.10.2	–	–	–	250	10	2	–	–	–	–	–	–
100.10.8	–	–	–	100	10	8	–	–	–	–	–	–
250.10.8	–	–	–	250	10	8	–	–	–	–	–	–
201	–	–	–	250	10	4	7.40	96.7	99.9	–	–	–
203	–	–	–	240	10	4	–	–	–	–	–	–
204	–	–	–	200	10	6	5.80	75.8	78.3	–	–	–
205	–	–	–	250	10	2	5.33	69.7	71.9	–	–	–
219	–	–	–	250	10	8	5.59	73.1	75.4	–	–	–
221	–	–	–	250	10	8	5.42	70.8	73.1	–	–	–
223	–	–	–	250	10	6	5.75	75.2	77.6	–	–	–
226	–	–	–	250	10	6	5.62	73.5	75.8	–	–	–
328	–	–	–	250	20	6	5.89	77.0	79.5	–	–	–
404	80	400	2	200	10	6	5.99	78.3	80.8	–	–	–

Sample	Powder conditioning			Hot pressing conditions			Density (g·cm^{-3})	% of theoretical density (1)	% of theoretical density (2)	Grain size (μm)	O:U (3)	O:U (4)
	% O_2	Temp. (°C)	Time (Hrs)	Temp. (°C)	Time (min)	Load (tons)						
406	92	400	2	200	10	6	5.61	73.3	75.7	–	–	–
410	70	400	2	200	10	6	6.13	80.1	82.7	–	–	–
411	5	200	2	200	10	6	6.60	86.3	89.1	–	–	–
412	15	200	2	200	10	6	6.78	88.6	91.5	1.77	2.87	2.89
418	5	200	1.5	200	10	6	6.61	86.4	89.2	1.58	–	–
419	5	200	1	200	10	6	6.82	89.2	92.0	1.52	2.81	2.88
420	21	200	2	200	10	6	6.98	91.2	94.2	1.51	2.99	2.98
421	21	200	2	180	10	4.5	6.46	84.4	87.2	1.68	–	–
422	5	200	1	180	10	4.5	6.81	89.0	91.9	1.60	–	–
423*	92	480	1	180	10	4.5	7.46	89.4*	92.9*	1.48	3.03	3.09
424*	21	480	1	180	10	4.5	8.05	96.5*	100*	1.40	2.95	2.99
425	50	300	1	180	10	4.5	6.34	82.9	85.6	–	–	2.97
427	30	300	1	180	10	4.5	6.39	83.5	86.2	1.65	2.90	2.96
429	80	200	60	180	10	4.5	6.85	89.5	92.4	1.80	–	–
430	80	200	60	180	10	4.5	6.96	91.0	93.9	–	–	2.99

Sample	Powder conditioning			Hot pressing conditions			Density (g·cm^{-3})	% of theoretical density (1)	% of theoretical density (2)	Grain size (μm)	O:U (3)	O:U (4)
	% O_2	Temp. (°C)	Time (Hrs)	Temp. (°C)	Time (min)	Load (tons)						
501	80	200	20	180	10	4.5	6.91	90.3	93.3	1.75	–	–
503	80	200	20	180	10	4.5	6.61	86.4	89.2	1.72	–	–
504	80	200	40	180	10	4.5	6.86	89.7	92.6	1.80	–	–
505	80	200	40	180	20	4.5	7.02	91.8	94.7	1.56	–	3.00
506	10	200	60	180	10	4.5	7.13	93.2	96.2	1.43	–	2.88
508	10	200	60	180	20	4.5	7.02	91.8	94.7	1.48	–	2.91
515	5	200	20	180	30	4.5	6.65	86.9	89.7	1.47	–	–
517	5	200	20	180	10	4.5	6.92	90.5	93.4	–	–	–
518	5	200	20	180	45	4.5	6.56	85.8	88.5	1.52	–	–
519	5	200	20	180	30	4.5	6.65	86.9	89.7	1.71	–	–
521	5	200	20	180	45	4.5	6.98	91.2	94.2	1.67	–	–

(1) Average theoretical density of γ-UO_3 = 7.65 g·cm^{-3} [61], [82]; (2) Composite density of 7.41 g·cm^{-3} calculated with an estimated 90% of γ-UO_3 and 10% hydrated phase $UO_2(OH)_2$ with a density of 5.24 g·cm^{-3} [173]; (3) Data obtained by titration; (4) Data obtained by ICP-MS; * samples designated as α-UO_3–$UO_2(OH)_2$ and their densities compared to theoretical density of α-UO_3 and that of the corresponding hydrate.

5.2. Basic Characterization

5.2.1. Density of UO_3 Samples

The density of the UO_3 samples was determined by measuring the relative change in the weight of the sample in air versus petroleum ether. The density of most pellets prepared without powder conditioning was 5.3–5.9 $g\cdot cm^{-3}$, which is ∼70% of the theoretical density of γ-UO_3, taken as 7.65 $g\cdot cm^{-3}$ [61], [82]. The pellets fabricated after powder conditioning achieved a higher densification (85–90% of theoretical density) with density values 6.5–7.0 $g\cdot cm^{-3}$. The densities of the UO_3 pellets are listed in Table 13. The density values are also compared to a composite phase calculated for an "average" hydrated composition, consisting of 10% $UO_2(OH)_2$ and 90% γ-UO_3. Samples 423 and 424, as noted, were identified as α-UO_3–$UO_2(OH)_2$ (**Section 5.2.4**) and had slightly higher densities. The higher density values of the α-UO_3 samples agree with the literature value of 8.34 $g\cdot cm^{-3}$ [61], [174]. The density of the pellets that were assigned as γ-UO_3 was found to decrease linearly with the powder conditioning temperature, as shown in Figure 42. The error bars represent the standard deviation of the density values of multiple pellets prepared from powder conditioned at the same temperature. No other trend was observed. An example is shown in Figure 43, which shows the variation of density of the UO_3 pellets as a function of their press times. All of the pellets were pressed with a load of 4.5 ton at 180 °C. The error was determined in the form of standard deviation of the density values of multiple pellets pressed for the same length of time.

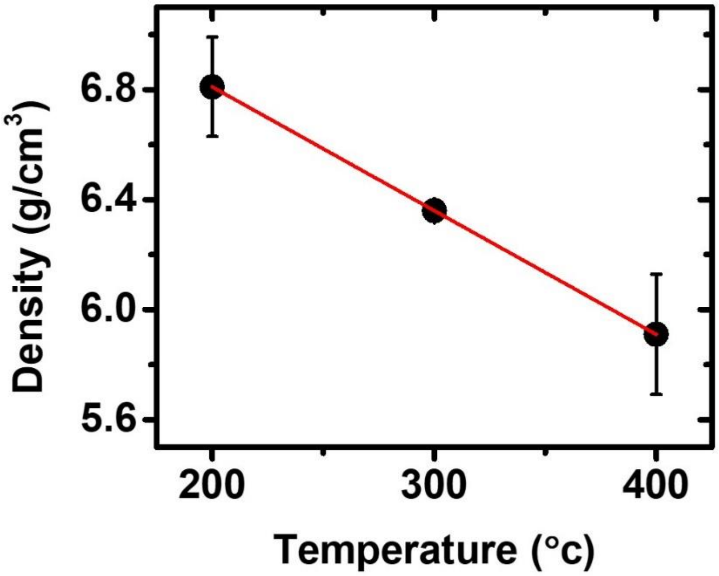

Figure 42. Density of the pellets that were assigned as *γ*-UO_3 as a function of powder conditioning temperature.

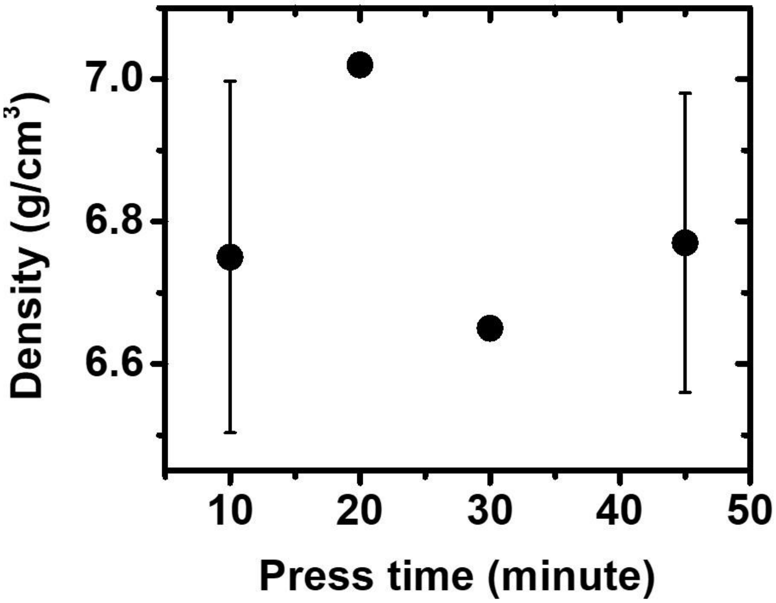

Figure 43. Density of the UO_3 pellets as a function of their press time for pellets that were pressed at 180 °C with a load of 4.5 ton.

5.2.2. Microstructure of UO_3 Samples

The grain size of the UO_3 pellets was measured in the same way as the grain size of U_3O_8. The samples were found to have grain size values of 1.47–1.80 μm (Table 13). No correlation was found between grain size and pellets processing conditions. An example is shown in Figure 44, which shows the grain size of the UO_3 pellets as a function of their density for pellets fabricated by pressing at 180 °C with a load of 4.5 tons for 10 minutes.

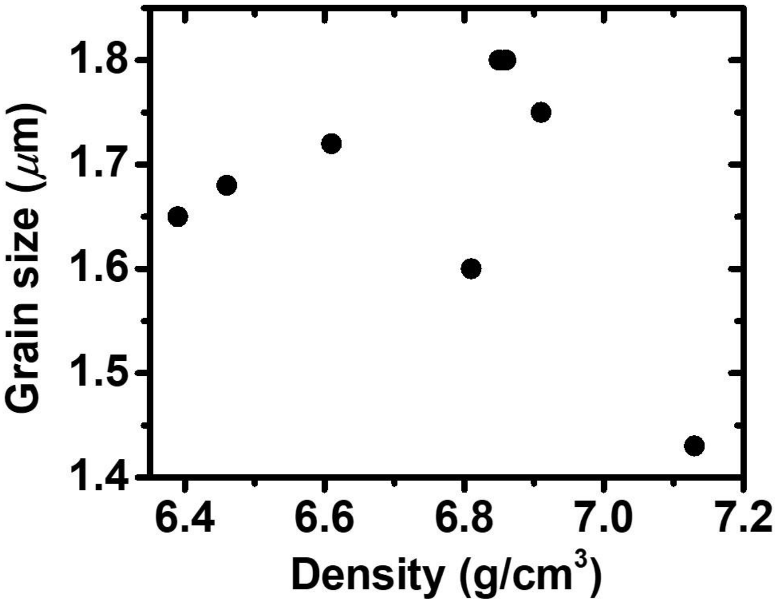

Figure 44. Grain size of the UO_3 pellets as a function of their density for pellets that were fabricated by pressing at 180 °C with a load of 4.5 ton for 10 minutes.

5.2.3. Stoichiometry of UO_3 Samples

The stoichiometry of the UO_3 samples was determined from potentiometric titration and inductively coupled plasma mass spectrometry (ICP-MS) in conjunction with x-ray diffraction (to estimate the amount of hydrates). ICP-MS was used to check the reliability of the data obtained from titration, since there were speculations about the applicability of titration to UO_3 (discussed in **Section 3.3.2**). The stoichiometry results from both the methods agree in terms of predicting hyper- and hypostoichiometry, however, there are discrepancies in the stoichiometry values obtained from the two experiments. This could potentially be due to inaccuracy in estimating the amount of hydrates from the XRD data, which lacked some "features" in the XRD scan (as will be explained in **Section 5.2.4**). Overall, the values of O/U were found to be 2.81–3.03 from titration and 2.88–3.09 from ICP-MS (combined with XRD). The O/U values of the UO_3 samples are listed in Table 13.

5.2.4. Phase of UO_3 Samples

The phase of a subset of UO_3 pellets was studied by grazing incidence x-ray diffraction. Unlike powders, bulk samples diffract x-rays as a function of the orientation of the individual grains within the sample. Since it cannot be assumed that each grain is randomly oriented in the bulk sample, counting statistics can be greatly reduced based upon the preferred orientation (or texture) of the grains, which is related to processing methods [110], [175]. This can lead to a loss of information as certain planes of diffraction may be absent in the resultant spectra.

The diffraction spectra of most of the UO_3 samples, as shown in Figure 45, match with γ-UO_3, albeit several characteristic diffraction peaks that correspond to the 2θ values in the range of 25–40° are missing [81]. This could potentially be due to the preferred orientation of crystallites masking the aforementioned diffraction peaks. The high intensity peaks that correspond to 2θ values of above 40°, shown in Figure 45(b), correspond to aluminum [176], which is a result of the x-ray being diffracted off of the aluminum sample holder, since the diameter of the x-ray beam was larger than the sample diameter. A comparison of all of the XRD data shows a distinct change in peak intensities and symmetry in the 2θ range of 17–20°. This indicates a varying amount of an additional phase within the sample, which is most likely a uranium hydrate, based on the peak position. Although it was not possible to precisely identify the phase composition for each sample, a reasonable estimate was made that 90% of the bulk material is γ-UO_3 and the remaining 10% is a hydrated phase.

Of the samples studied with x-ray diffraction, one sample (423) was identified as consisting of ~91% α-UO_3 and ~9% α-$UO_2(OH)_2$ as shown in Figure 46. The amount of hydrate was estimated based on the best matching peak that corresponded to the α-$UO_2(OH)_2$ phase. Sample 423 is one of two samples (423 and 424) fabricated from powder conditioned at 480 °C, unlike other samples which were fabricated from powder conditioned at or below 400 °C. The powder conditioned at 480 °C appeared brown unlike the powder conditioned at or below 400 °C, which appeared orange (see **Section 5.1**). Sample 423, along with 424, had density values higher than those of other samples, which is consistent with the literature that the density of α-UO_3 is higher than that of γ-UO_3. These samples also had a lower band gap and resistivity as compared to other samples, as shown in Table 14 and will be discussed in **Section 5.3** and **Section 5.4**.

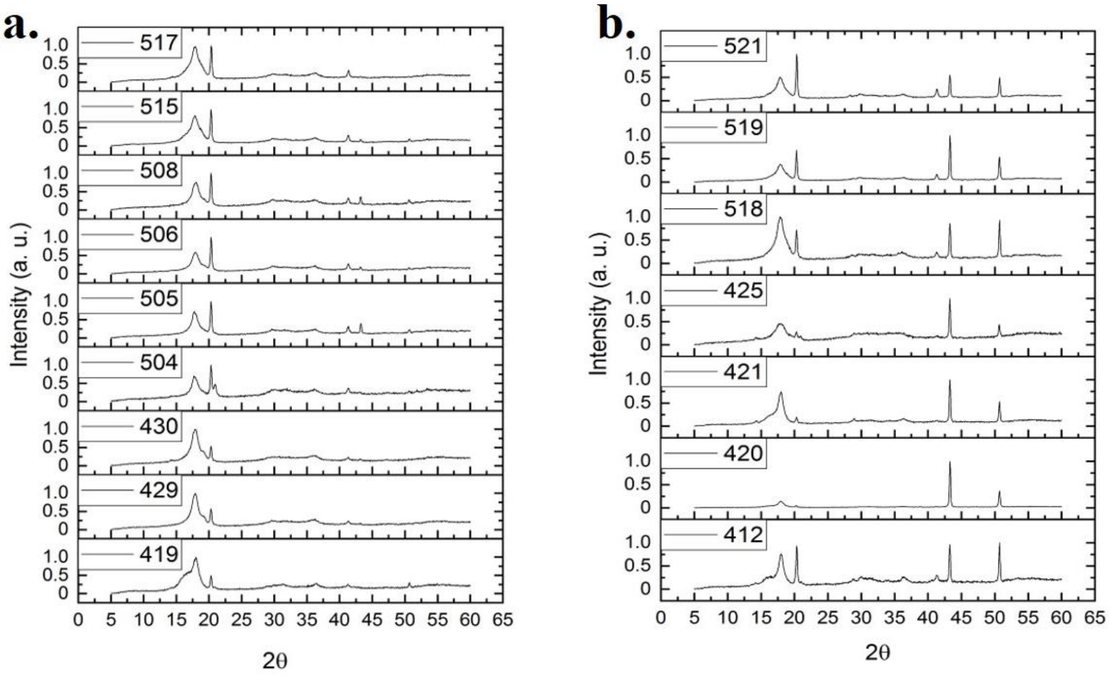

Figure 45. X-ray diffraction data of some UO_3 samples: (a) data that do not show aluminum peaks (b) data that show aluminum peaks.

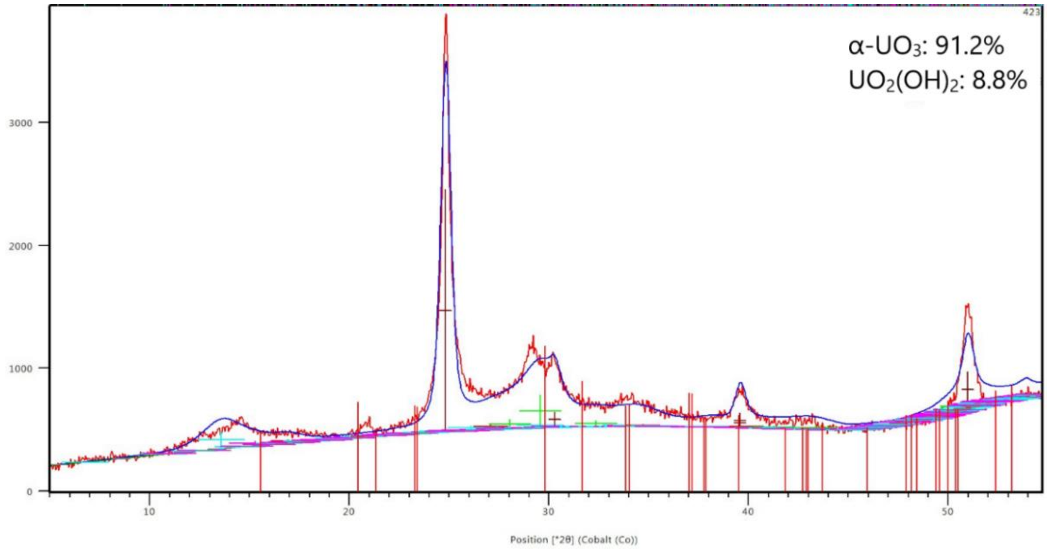

Figure 46. X-ray diffraction pattern of sample 423 with Rietveld refinement overlay showing the best matches with α-UO_3 and α-$UO_2(OH)_2$.

5.3. Electronic Structure Study: Band Gap

A knowledge of the band gap of a material to be used for neutron detection is relevant for several reasons. First, the number (n) of charge carriers excited in the detector material following a neutron absorption event depends on the band gap (E_g) of the material as given by [87]:

$$n = \frac{Q}{\frac{14}{5}E_g + r(\hbar\omega)} \tag{5.1}$$

where Q is the energy deposited in the detector by the product(s) of nuclear reaction, and $r(\hbar\omega)$ is the scattering factor, which satisfies the condition: $0.5 \leq r\,(\hbar\omega) \leq 1$ eV. Thus, n is inversely proportional to E_g, and a lower band gap will lead to a higher charge generation. The higher number of charge carriers generated, the higher the signal current during a detection event.

Second, the optical band gap defines the photon energy required to excite e–h pairs in a material. This knowledge is useful from a practical standpoint in carrying out photoconductivity-based experiments.

Third, the band gap information is important because this plays a role in determining the type of contact (injecting/blocking) made between a bulk material and different electrode. The type of contact affects the overall behavior of a device, and different types of contacts are suitable for different charge transport experiments as well as neutron detector configurations. The type of contact formed between a material and electrode depends on the band lineup of the two. Ultimately, several pieces of information are needed to construct a band diagram for a material; indirectly, we can use a combination of band gap, work function, and the energy difference between the Fermi level and the valence band edge (Figure 47).

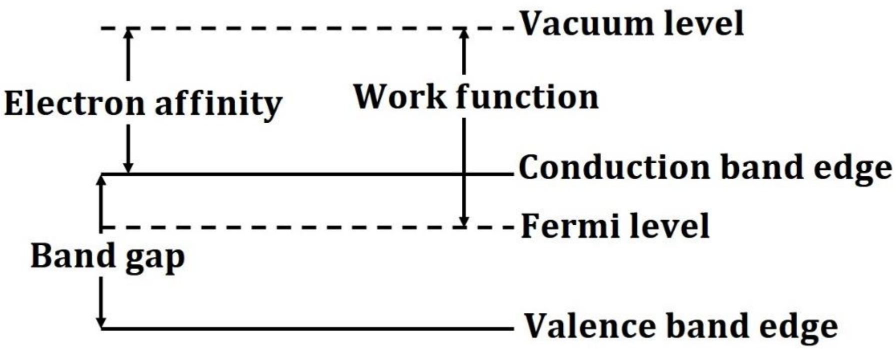

Figure 47. Representation of energy bands of a semiconductor (*n*-type).

The band gap of the UO_3 samples was studied by diffuse reflectance spectroscopy. The optical band gaps for all of the samples are shown in Table 14. Early samples prepared without powder conditioning (100 through 300 range) exhibit multiple band edges (Figure 48 a and b, for example), which may support the proposed existence of one or more hydrated phases [70]. The dominant band edge could be fit to both direct and indirect band gap values, giving values in the range of 2.39–3.14 eV and 2.11–2.27 eV for these, respectively. The remaining samples which underwent powder conditioning (400 onwards) exhibited a more distinct band edge, possibly suggesting a higher phase purity, and fit best to indirect band gap values, although fits for direct band gap values are also shown. Indirect band gap values ranged from 1.84 to 2.06 eV. The samples assigned as α-UO_3 exhibited slightly lower band gaps of 1.94 (sample 423, Figure 48 c) and 1.91 eV (sample 424), whereas the remaining samples assigned as γ-UO_3 exhibited band gaps of ~2.0 eV (Figure 48 d, for example). Samples 404 and 406, for which powder conditioning was done at 400 °C, also display lower band gaps (1.84 and 1.94 eV), which suggest that these too, may comprise the α phase. No evident trend was observed between the band gap values and the sample fabrication conditions. The remaining results of analysis of the band gap of the UO_3 pellets are given in APPENDIX D.

The band gap values of powdered samples of α-UO_3 and γ-UO_3 have been previously reported by Khilla and Rofail [86] to be 2.61 and 2.38 eV, respectively, based on the arbitrary definition of the optical band gap as equal to the photon energy corresponding to the midpoint of the absorption edge. Additionally, He *et al*. [70] reported theoretical band gap values of 2.65 and 2.35 eV for α- and γ-UO_3 respectively, and Brincat *et al.* [145] reported theoretical band gap values of 1.59 and 2.39 eV for α- and γ-UO_3 respectively using a DFT+U approximation. The direct band gap values of α-UO_3 are close to the values reported by Khilla and Rofail as well as He *et al.* In contrast, the indirect band gap values obtained from our experiments are, in general, lower than the literature values and the direct band gap values are mostly higher than the literature values. It should be noted that in the work of both He *et al*. and Brincat *et al.*, the Hubbard coefficient parameters for UO_3 have been assumed as equal to those for UO_2; the values may be different in reality because these parameters depend on the atomic coordination (**Section 3.6.5**). This could potentially explain the discrepancy between the literature-reported values and those reported here.

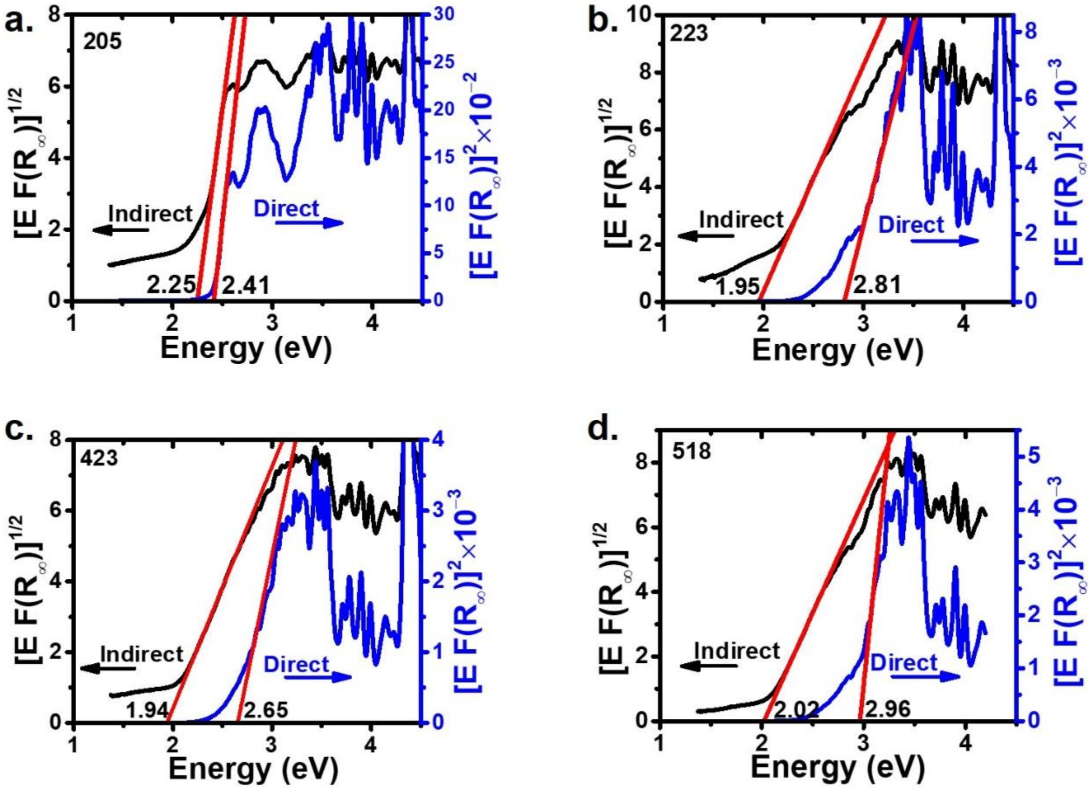

Figure 48. Band gap analysis of some representative samples: (a) sample 205, prepared without powder conditioning (b) sample 223, prepared without powder conditioning (c) sample 423, characterized as α-UO_3, and (d) sample 518, characterized as γ-UO_3.

Table 14. Band gap and resistivity of UO_3 samples.

Sample	**Band gap (eV)**		**Resistivity (Ω-cm)**
	Indirect	**Direct**	
100.10.2	2.22	2.42	7.95×10^{10}
250.10.2	2.11	3.14	1.24×10^{10}
100.10.8	2.23	2.42	–
250.10.8	2.27	2.43	4.14×10^{10}
201	2.72	3.24	9.32×10^{11}
203	2.16	2.39	–
204	2.23	2.39	8.31×10^{11}
205	2.25	2.41	–
219	2.25	2.42	–
223	1.95	2.81	–
226	1.93	2.89	–
404	1.84	2.50	–
406	1.94	2.72	–
411	2.00	2.91	–
412	2.02	2.86	3.87×10^{10}
418	2.03	2.86	–
419	2.02	2.95	9.29×10^{10}
420	2.05	2.95	3.22×10^{10}
421	2.05	2.98	3.14×10^{10}
422	2.06	2.97	–
423	1.94	2.65	2.05×10^{8}
424	1.91	2.67	4.29×10^{6}
425	1.97	2.73	–

Sample	Band gap (eV)		Resistivity (Ω-cm)
	Indirect	Direct	
427	1.98	2.81	1.55×10^{9}
429	1.99	2.89	2.89×10^{9}
430	2.01	2.88	–
501	2.01	2.84	1.41×10^{10}
503	2.03	2.88	–
504	2.03	2.88	7.89×10^{9}
505	2.00	2.91	5.71×10^{9}
506	1.95	2.89	1.21×10^{10}
508	1.97	2.88	–
515	2.01	2.93	2.36×10^{10}
517	2.03	2.95	–
518	2.02	2.96	1.69×10^{10}
519	2.01	2.89	1.55×10^{10}
521	2.02	2.87	–

5.4. Resistivity

The resistivity of the UO_3 pellets was determined by current–voltage measurements. The measured resistivity values were, on average, in the range of 10^{9}–10^{10} Ω-cm and are summarized in Table 14. Two of the early samples, 201 and 204, exhibited even higher resistivities. These samples were prepared without powder conditioning and pressed at the maximum operating temperature for the die. The resistivity values for samples 423 and 424, characterized as α-UO_3 rather than γ-UO_3, exhibited lower values on the order of 10^{8} and 10^{6} Ω-cm, close to the value of $\sim10^{7}$ Ω-

cm reported in the literature [85]. The current–voltage graphs of two representative samples are shown in Figure 49 and the remaining results are shown in APPENDIX E. No clear correlation was observed between the resistivity values and the sample fabrication conditions as seen from the resistivity vs density graph in Figure 50 and resistivity vs grain size graph in Figure 51.

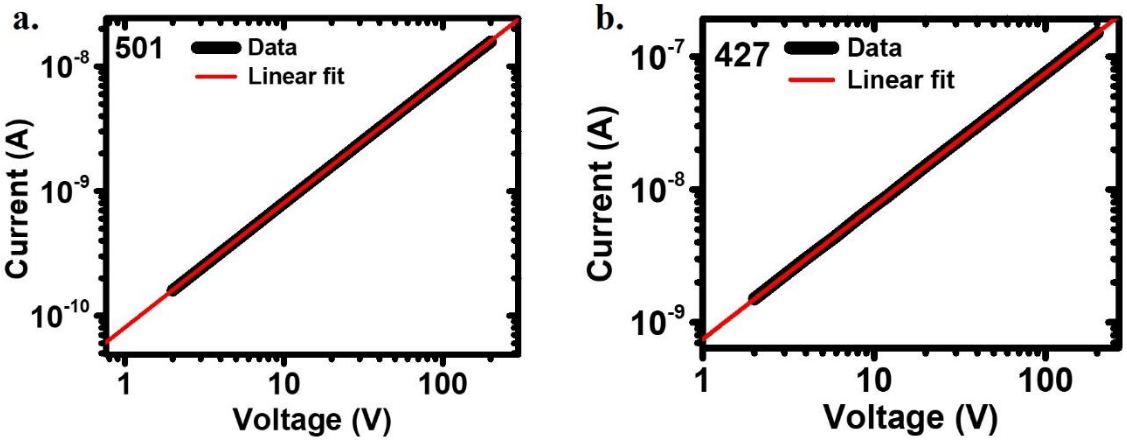

Figure 49. *I*–*V* characteristics of (a) samples 501 (b) sample 427.

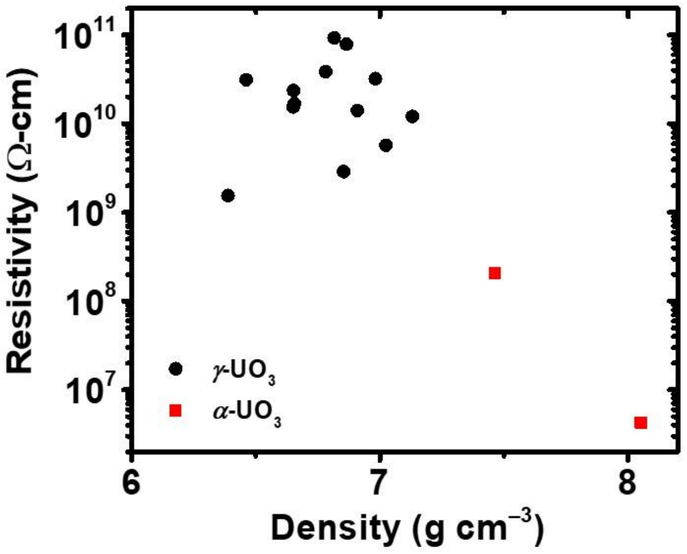

Figure 50. Resistivity of the UO$_3$ samples as a function of their density.

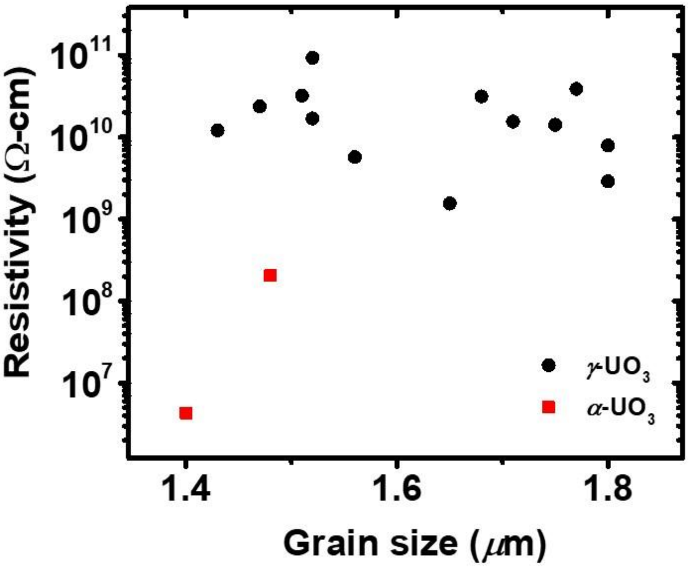

Figure 51. Resistivity of the UO$_3$ samples as a function of their grain size.

5.5. Charge Carrier Mobility from Space-Charge-Limited-Current

We conducted high-voltage *I*–*V* measurements on a subset of the UO_3 samples, increasing voltage from zero until an electrical breakdown was observed. The *I*–*V* graphs of most samples were obtained as straight lines. However, for a couple of samples (410 and 412), the *I*–*V* graph showed the transition from a linear to a super-linear region, possibly indicating space-charge effect. The result of high-voltage *I*–*V* measurements on sample 410 is shown in Figure 52 and the result for sample 412 is shown in APPENDIX F. The *I*–*V* graph has a region of maximum slope of 1.68, suggesting the onset of a space-charge region at about 1000 V. Since, we did not observe a region in the log–log plot with a clear slope of 2, from which we can extract charge carrier mobility via Equation (3.42), instead we calculated a maximum value based on the transition point. Taking 1000 V as the minimum voltage for the beginning of the space-charge regime in the UO_3 samples, we can calculate the maximum value of charge carrier mobility using Equation (3.40):

$$\mu_{\max} = \frac{d^2}{\epsilon \rho V_{\max}} \tag{5.2}$$

The dielectric constant was approximated from capacitance–voltage measurements as 14. So, using $\epsilon = 14 \times 8.854 \times 10^{-12}$ F·m^{-1}, $\rho = 10^9$ Ω-cm, and $d = 1$ mm, Equation (5.2) gives $\mu_{\max} = 8 \times 10^{-3}$ cm^2·V^{-1}·s^{-1}. This suggests that the charge carrier mobility is lower than 8×10^{-3} cm^2·V^{-1}·s^{-1}.

Since most samples have very similar resistivity, it is safe to assume that this boundary of maximum charge carrier mobility holds for most samples, if the carrier concentration in each sample is in the same range.

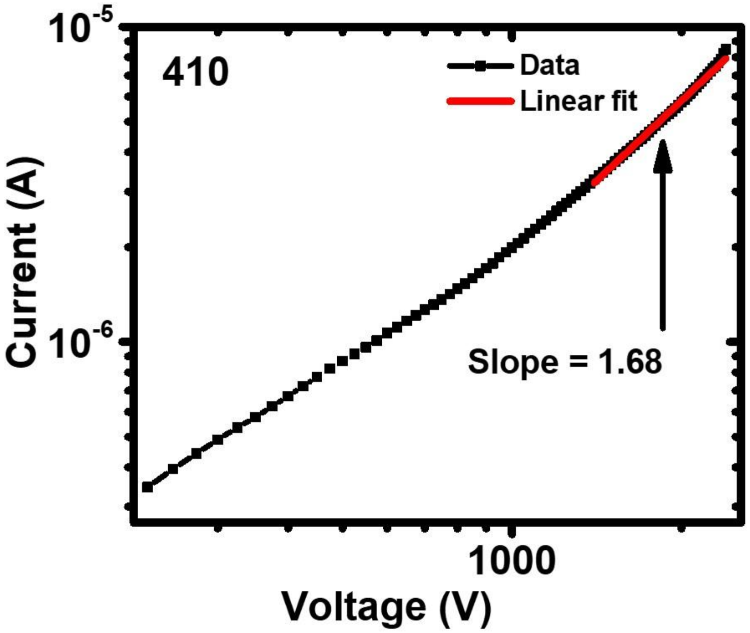

Figure 52. *I–V* characteristic of sample 410 measured using high-voltage program/circuit.

5.6. Mobility and Mobility–Lifetime of Charge Carriers from Photoconductivity

Transient (i.e., ToF) and steady-state photoconductivity experiments were conducted on UO_3 samples in an attempt to extract charge carrier mobility and mobility–lifetime product respectively. In the ToF photoconductivity experiment, a light pulse excites the charge carriers in a sample and an external electric field sweeps the excited charge carriers towards the collecting electrode, producing a transient signal current. The transit time is then obtained from the transient signal, from which the charge carrier mobility can be obtained. The signal current can be integrated over the transit time to obtain the charge collected for different bias voltages, which can then be used to obtain the mobility–lifetime product of the charge carriers using a Hecht analysis. The charge carrier mobility–lifetime can also be determined by a Hecht analysis of the photocurrent–

voltage data obtained from the steady-state photoconductivity. In this method, a sample is irradiated with a beam of light to obtain photocurrent through the sample as a function of bias voltage.

The results of some measurements of steady-state photoconductivity are shown in Figure 53. All samples showed non-negligible photoconductivity, however, we did not see any photocurrent saturation. In fact, the dark current shows some space charge effect. This suggests that the contacts may not be blocking.

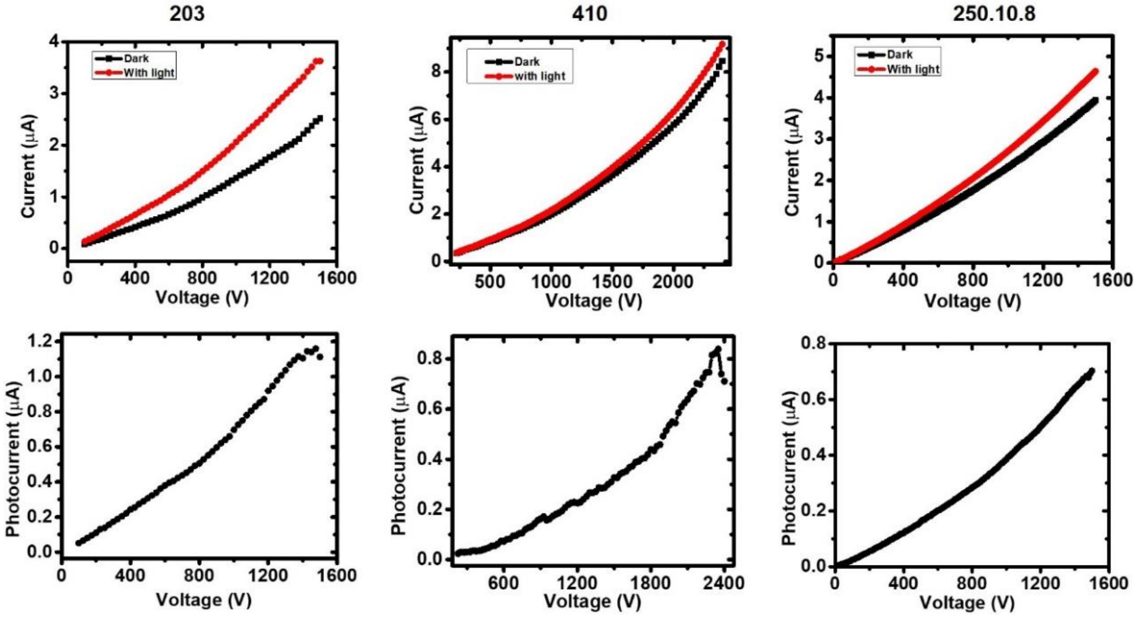

Figure 53. Results of steady-state photoconductivity experiments on sample 203, 410 and 250.10.8.

Time-of-flight (ToF) photoconductivity experiments were conducted on several samples with bias voltage ranging from a few hundred volts to a few kilovolts. Although a clear transient photocurrent signal was obtained (Figure 54), the transit time was not observed even for an applied voltage as high as 3500 V (see Figure 25 and **Section 3.8.3**). Assuming no alternative effects are at play, we can estimate the maximum charge carrier mobility, based on the lack of signal. Since the transient current decayed to zero at about 100 μs, we will assume that the transit time of charge carriers is more than 100 μs at an applied voltage of 3500 V. From Equation (3.46):

$$\mu_{\mathrm{max}} = \frac{d^2}{V t_{\mathrm{tr(min)}}} \tag{5.3}$$

where, $t_{\mathrm{tr(min)}}$ is the minimum transit time, and μ_{max} is the maximum carrier mobility. Here, $t_{\mathrm{tr(min)}}$ = 100 μs, d = 1 mm, and V = 3500 V. So, $\mu_{\mathrm{max}} = 3\times10^{-2}$ cm^2·V^{-1}·s^{-1}.

The maximum value of charge carrier mobility calculated here is slightly higher than that calculated from the space-charge-limited current analysis, which is consistent. This suggests that if the charge carrier mobility is in fact lower than 10^{-3} cm^2·V^{-1}·s^{-1}, then we cannot observe the appropriate signal with either of these methods.

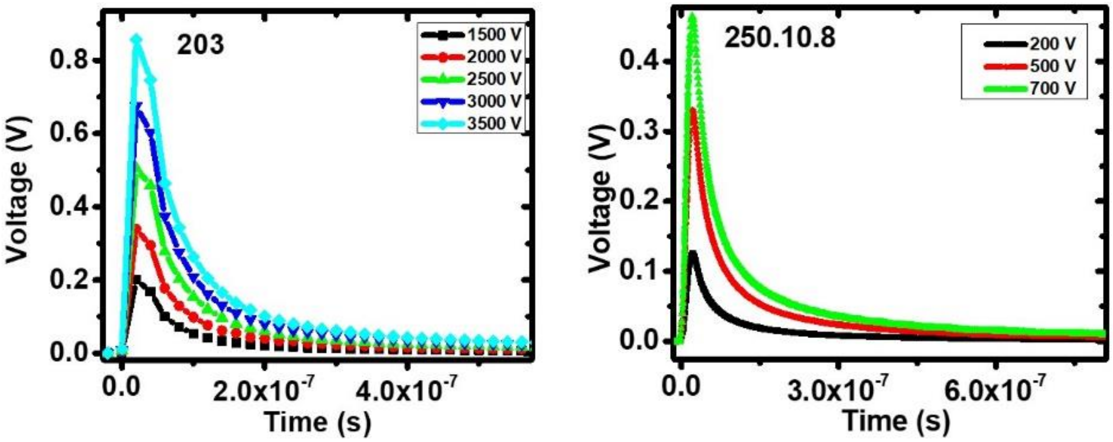

Figure 54. Transient photocurrent signal for different voltages for samples 203 and 250.10.8.

In order to obtain the charge carrier mobility of such a high-resistance, low-mobility material, the thickness of the sample can be decreased, so that the transit time of the charge carriers is shorter and observable in the ToF signal. However, the sample should be thick enough so that most of the incident light is absorbed at the sample surface. Also, a slightly thinner sample will be useful in obtaining a space-charge-limited current at a lower voltage, as seen from Equation (3.41). For example, if the thickness of a material is reduced to half, the voltage required to achieve the space-charge regime in the material will be reduced by a factor of four. An additional and probably the most effective way to observe the carrier mobility is to increase it by some way (e.g., doping, increasing grain size, altering stoichiometry/carrier concentration), which will be discussed in brief in the following sections.

5.6.1. Discussion on Potential Ways to Improve Charge Carrier Mobility

Fundamentally, the charge carrier mobility of a material depends on its effective mass (m^*) and mean relaxation time, as given by the equation:

$$\mu = \frac{e \, \langle \tau_{\mathrm{rel}} \rangle}{m^*} \tag{5.4}$$

where e is the charge of an electron and $\langle \tau_{\mathrm{rel}} \rangle$ is the mean relaxation time, which is the time for which a charge carrier is accelerated by the electric field before being scattered. Therefore, the effective mass and the scattering of the charge carriers are fundamentally responsible for controlling their mobility in a material.

5.6.1.1. Effective Mass

The effective mass of an electron is its apparent mass while responding to forces inside a crystal. Electrons moving in a crystal experience a periodic potential due to the ion cores, which give rise to energy band and band gaps, as described by the band theory of solids. According to band theory, the movement of charge carriers in a periodic potential can be described by modeling the behavior of a free particle with that mass: this mass is called the effective mass of the charge carrier.

The effective mass of charge carriers in compound semiconductors is associated with the orbitals that form the conduction and valence bands. For example, in oxides of metals with unfilled *d*-orbitals, the valence band minima are mainly formed from fully occupied 2*p*-orbitals of oxygen whereas the conduction band minima (CBM) are made up of empty, primarily large, spherically symmetric *s*-orbitals of metal cations. Such an electronic structure in certain metal oxides, for example ZnO and SnO_2, leads to small electron effective mass and hence large electron mobility. The *s*-orbitals, which have large spatial sizes and spread almost spherically, form largely hybridized CBM with large band dispersion, which is the reason for the small electron effective mass [177], [178]. On the other hand, if the contribution of the *s*-orbitals to the CBM is much smaller compared to that of other orbitals, the electron effective mass is large, for example in the case of ZrO_2 [179], [180]. Extending this idea, UO_3 should have a large electron effective mass because its CBM are mainly formed from the 5*f*-orbitals of uranium, as seen in the literature [145], and will be seen in **Section 5.6.1.4**.

5.6.1.2. Scattering

The scattering mechanism in a crystal consists of three important mechanisms: scattering at crystal defects, scattering at wanted impurity atoms, and scattering due to phonons.

Scattering at crystal defects can result from crystal impurities such as the presence of foreign atoms, which alters the localized potential for electrons, or from imperfections in crystals such as defects and grain boundaries, or from physical damage to crystals such as cracks. Scattering at wanted impurity atoms refers to the scattering due to dopants, which occurs when a charge carrier is deflected by the electrostatic potential of an ionized donor or acceptor. This type of scattering decreases with temperature because at high temperature the charge carriers move faster and are less effectively scattered. Scattering from phonons arises due to thermal vibrations of the crystal atoms. Some lattice vibrations cause positive and negative ions at adjacent lattice sites to “swing” against each other, giving rise to a time-varying electric field, which scatters the charge carriers. This type of scattering increases with increasing temperature because lattice vibrations become more pronounced at higher temperatures. The opposing effects of temperature on the latter two mechanisms somewhat cancel each other out as the temperature increases [32]. Assuming that τ_{defect}, τ_{dopant}, and τ_{phonon} are the relaxation times associated with these three scattering mechanisms respectively, the mean scattering time is given as:

$$\frac{1}{\langle\tau_{\mathrm{rel}}\rangle}=\frac{1}{\tau_{\mathrm{defect}}}+\frac{1}{\tau_{\mathrm{dopant}}}+\frac{1}{\tau_{\mathrm{phonon}}} \tag{5.5}$$

Equation (5.5) shows that the smallest relaxation time dominates.

5.6.1.3. Ways to Increase Charge Carrier Mobility

From Equation (5.4), we see that there are two ways to potentially enhance the charge carrier mobility in a material: decreasing the effective mass and increasing the mean relaxation time of charge carriers.

The effective mass of charge carriers in a material could be tailored to tune the charge carrier mobility [181], [182]. Based on the discussion in **Section 5.6.1.1**, the contribution of the metal *s*-orbitals to the conduction band could be increased to decrease the electron effective mass, which may lead to increased electron mobility. This could potentially be achieved by doping and/or making ternary compounds (or mixed crystals). For example, Amemiya and Sakai [183] have theoretically studied InSb crystals and suggested that adding Bi to a InSb crystal may lead to an increased charge carrier mobility. However, the change in effective mass, in general, is not orders-of-magnitude. As such, the increase is charge carrier mobility is relatively small.

The mean relaxation time of charge carriers can be increased by decreasing the factors that contribute to scattering: scattering at foreign atoms can be decreased by making a pure crystal; scattering at grain boundaries can be reduced by increasing the grain size, preferably making a single crystal; scattering at crystal defects such as vacancies can be reduced by adding suitable dopants in order to compensate those defects. For example, Polyakov *et al.* [184] increased the electron mobility in GaN and reduced the free electron concentration by 10 orders-of-magnitude by doping it with Fe. This indicates that the defects in GaN that contribute to free electrons were compensated thereby decreasing the free carrier concentration and lowering the scattering effect, which helped to increase the charge carrier mobility. The compensation doping is also likely to increase the resistivity of materials by decreasing the free charge carrier concentration, which would make for a near-perfect scenario for a radiation detector material.

5.6.1.4. Computational Studies of Electronic Structures of UO_3 and Mixed Crystals

Towards the possibility of tuning the electron effective mass, we carried out computational studies of variation in the electronic structure of γ-UO_3 when atoms of other elements are added to the crystal. First the electronic structure of γ-UO_3 was calculated for a 64-atom (16 uranium and 48 oxygen) crystal. Then a uranium atom was replaced with a foreign atom and the electronic structure was calculated again. Foreign atoms with ionic radii close to that of uranium were chosen. Since the ionic radius of a uranium atom in UO_3 is 0.73 Å [185], the atoms chosen for adding were chromium (ionic radius of 0.73 Å for oxidation state of II), copper (ionic radius of 0.73 Å for oxidation state of II), molybdenum (ionic radius of 0.73 Å for oxidation state of VI), titanium (ionic radius of 0.74 Å for oxidation state of IV), and niobium (ionic radius of 0.72 Å for oxidation state of state of III). We wanted to see if the contribution to the conduction band by the metal cation *s*-orbital increases, which would give us a qualitative idea about the decrease in electron effective mass, and therefore improved charge carrier mobility (see **Section 5.6.1.1**).

The electronic structure of γ-UO_3 was calculated by the DFT+U method using VASP as described in **Section 3.6**. The partial density of states (PDOS) of γ-UO_3 is shown in Figure 55, which is in agreement with the literature [145]. The conduction band consists of primarily U 5*f*-orbitals whereas the valence band consists of primarily O 2*p*-orbitals. This agrees with the U^{6+} oxidation state and $5f^0$ electronic configuration of uranium in UO_3, as mentioned in **Section 1.4.3**. There are small contributions of the U 7*s*-, 6*d*-, and 6*p*-orbitals as well as the O 2*s*-orbitals to both the valence and conduction band. Finally, there are small contributions of the U 5*f*-orbitals to the valence band and the O 2*p*-orbitals to the conduction band, which has been attributed to the degree of covalency in U–O bonds in the literature [145]. The band gap value obtained is 2.23 eV, which is slightly higher than out experimental result of ~2 eV (**Section 5.3**). Overall, since the conduction band of UO_3 is primarily composed of U 5*f*-orbitals, we expect a high electron effective mass and therefore a low charge carrier mobility, as discussed in **Section 5.6.1.1**.

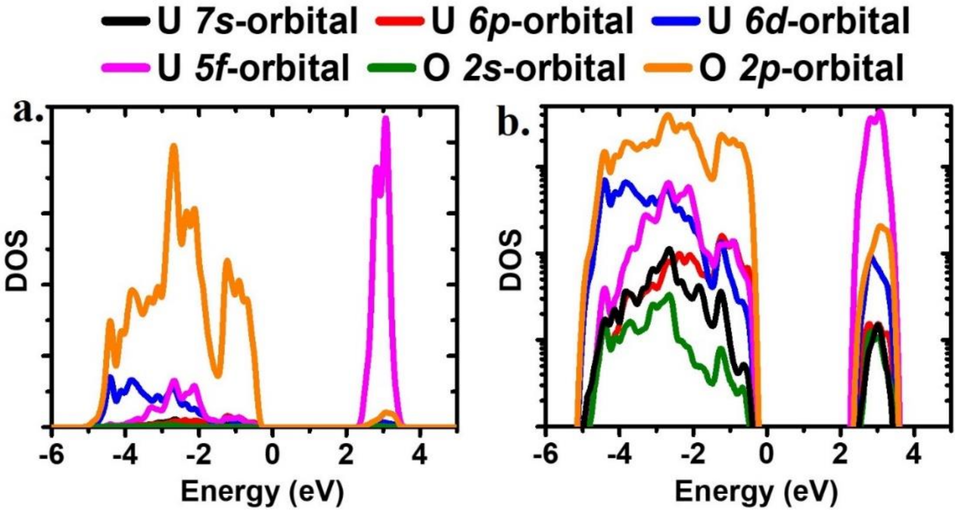

Figure 55. PDOS of γ-UO$_3$ calculated by the DFT+U method showing that the conduction band of γ-UO$_3$ consists of mainly 5*f*- and 6*d*-orbitals of U and 2*s*-orbitals of O. (a) conventional representation (b) log-scale used in y-axis for a better view of all the states.

Figure 56 shows an example of the PDOS of the conduction band of a Cr-mixed UO$_3$ system. We do not observe a significant contribution of the cation *s*-orbital to the conduction band of the mixed crystal. Figure 57 shows a comparison between relative contributions of cation *s*-orbitals to the conduction band of pure UO$_3$ and Cr-mixed UO$_3$. Although we observe a definite effect of chromium, it is not clear enough to conclude if the contribution of the cation *s*-orbital has increased in Cr-mixed UO$_3$. Similar results were obtained when the mixing atom was changed. Therefore, no conclusion can be drawn regarding the charge carrier mobility of mixed crystals of UO$_3$. The PDOS of the conduction band of remaining mixed crystals are shown in APPENDIX G.

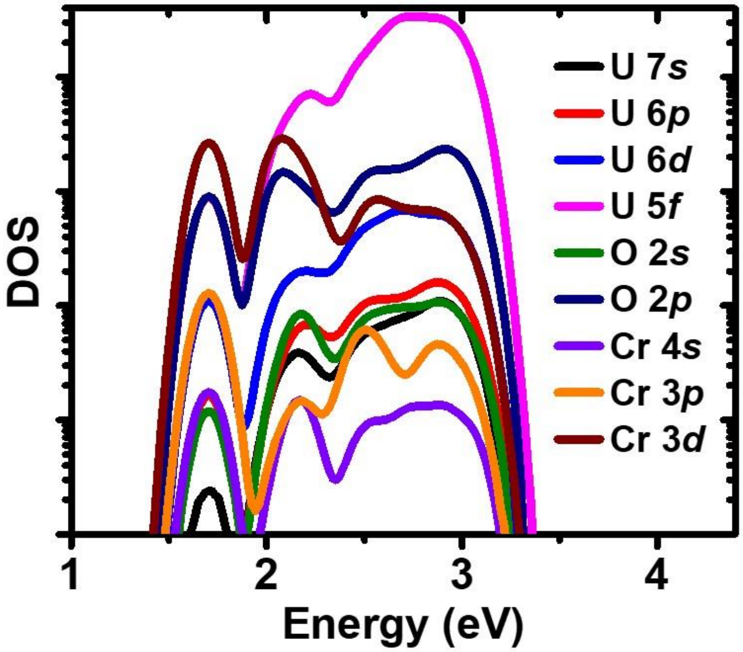

Figure 56. PDOS of conduction band of Cr-mixed UO_3.

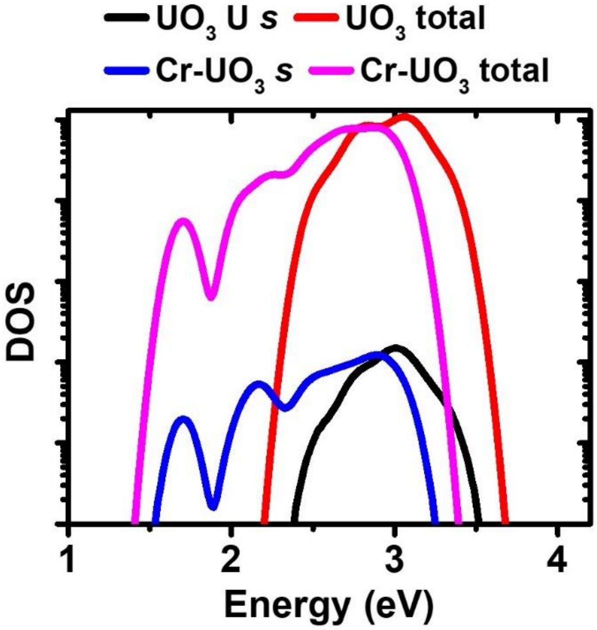

Figure 57. Comparison of contribution of cation *s*-orbital to the conduction band in UO_3 and Cr-mixed UO_3.

In order to further probe the electronic structure of UO_3 (and its mixed oxides), we attempted to estimate the electron effective mass directly from the curvature of the conduction band ($m^* = \hbar^2/(\partial^2 E/\partial k^2)$). However, the calculated band structure predicted a very high band gap (>3 eV) and a very low electron effective mass, which is unlikely (see **Section 5.7**). Since we could not obtain a reliable band structure, additional refined calculations will be required to estimate the electron effective mass directly.

5.7. Polaronic Effect in UO_3

A description of charge carriers in terms of electrons and holes is insufficient in some crystals (such as many II–VI semiconductors, alkali halides, and many oxides) in which the Coulomb interaction between a conduction electron and the lattice ions results in a strong electron–phonon coupling. The electron and its coupled phonon together are treated as a single composite particle, referred to as a polaron. Physically, an electron polaron corresponds to an electron pulling nearby positive ions towards it and pushing nearby negative ions away [186]–[190]. The hole polaron can be described analogously, however, this discussion will be limited to electron polarons only, since UO_3 is an *n*-type semiconductor.

The strength of the electron–phonon coupling in a material is given by a number referred to as Fröhlich's constant, α, given as [191]:

$$\alpha = \frac{e^2 u}{16\pi^2 \epsilon_0 \hbar^2 \nu}\left(\frac{1}{\epsilon_\infty} - \frac{1}{\epsilon}\right) \tag{5.6}$$

where e is the electronic charge, ϵ_0 is the permittivity of free space, and ϵ and ϵ_∞ are the static and high-frequency dielectric constants of the material. The quantities u and v are defined by the following equations:

$$u = \sqrt{2m^* h\nu} \tag{5.7}$$

$$\nu = \nu_0 \sqrt{\frac{\epsilon}{\epsilon_\infty}} \tag{5.8}$$

Here, m^* is the electron effective mass, v is the frequency of optical phonons, and v_0 is the reststrahlen frequency, which can be determined from infrared spectra (given by the frequency that corresponds to maximum absorption). Equation (5.7) gives the dimension of the polaron and Equation (5.8) gives the maximum frequency of lattice vibrations of the crystal. The parameter α is approximately equal to twice the total number of phonons coupled with the electron. The polaronic effect is regarded to be significant when the value of α is 1 or larger [190], [191].

The low charge carrier mobilities in UO_2 and U_3O_8 have been explained in terms of polarons in the literature [42], [44], [67], [192]. Here, we use the same approach to examine the polaronic effect in UO_3. We examine three things: the strength of electron–phonon coupling (α), the time spent by electrons at a lattice point, and the dimension of the polaron. We start by calculating the value of α, using Equations (5.6), (5.7), and (5.8).

For UO_3, we used $\epsilon_\infty = 3.17$, obtained from the square of the refractive index value [193], $\epsilon = 14$ (**Section 5.5**), and $v_0 = 850$ cm^{-1} [194]. Since the value of the electron effective mass is not available in the literature, we used the mass of a free electron. This gives $\alpha \approx 1.9$, which shows that the polaronic effects are significant. It should be noted that α is greater than 1 even if the electron effective mass is as low as 0.3 times the free electron mass. However, since the electron mobility of UO_3 is very low, it is highly unlikely that this would be the case, and in fact uranium oxides are expected to have electron effective mass values greater than the free electron mass [67]. Therefore, the polaronic effect is very likely contributing to the low electron mobility in UO_3.

The transition probability per unit time of an electron between lattice sites is given by the equation [195]:

$$W = \mu\left(\frac{kT}{ea^2}\right) \tag{5.9}$$

where μ is the electron mobility, k is the Boltzmann constant, T is the absolute temperature, and a is the distance between two nearest cations.

For UO_3, we use our estimated value of $\mu = 10^{-2}$ $cm^2{\cdot}V^{-1}s^{-1}$ (*vide supra*) and $a \approx$ 3.5 Å [82] in Equation (5.9), which gives $W = 2.1\times10^{11}$ s^{-1} (at room temperature). The maximum frequency of lattice vibrations, calculated using Equation (5.8), is 5.4×10^{13} s^{-1}. Therefore, the frequency of lattice vibrations is greater than the probability per unit time of transition of electrons between lattice sites, which means that the electron will stay around the cation for a sufficiently long time to polarize its neighborhood and thus can be said to be in the polaron state.

Using Equation (5.7), we obtain the dimension of the polaron as 5.8 Å (again we have assumed the electron effective mass as the free electron mass), which is comparable to the distance between neighboring cations in UO_3. This is a strong indicator of the existence of a “small” polaron [186].

In this way, we have presented three arguments to claim that the charge carrier in UO_3 is a small polaron. Since small polarons are generally transported via thermally activated hopping, such polaronic effects in a material can be experimentally verified from temperature dependence of conductivity by plotting σT vs $1/T$, where σ is the conductivity of the material at an absolute temperature T [42]. This will be a part of future work.

5.8. Summary

UO_3 pellets were prepared by uniaxial hot pressing from powder that was conditioned by exposing to various oxygen environments (5–92% O_2/Ar) and temperatures (200–480 °C). Most pellets had density values of 85–90% of theoretical density. When studied with x-ray diffraction, most pellets were found to be composed of $\sim$90% γ-UO_3 and $\sim$10% α-$UO_2(OH)_2$, a hydrate form of uranium oxide. Most samples, whose stoichiometry was measured, were hypostoichiometric. No correlation was observed between the sample fabrication conditions and their basic properties (e.g., density and stoichiometry). The formation of hydrates made it very challenging to properly characterize and control the material properties.

The data obtained from diffuse reflectance spectroscopy of UO_3 were analyzed for both direct and indirect band gaps, using Tauc's analysis, which gave an indirect band gap of $\sim$2 eV and a direct band gap of $\sim$2.9 eV for most samples. The electronic structure was studied computationally by DFT+U method using Vienna *ab initio* simulation package. The partial density of states obtained for γ-UO_3 agreed with literature and gave a band gap value of 2.23 eV, slightly higher than the value obtained from our experiment. The resistivity values of the samples were generally found to be 10^9–10^{10} Ω-cm, which are slightly higher than the literature reported values. The charge carrier mobility could not be determined exactly due to the lack of proper signal. Therefore, based on the absence of signal, a maximum value of 10^{-3}–10^{-2} $cm^2 \cdot V^{-1} \cdot s^{-1}$ of charge carrier mobility was calculated. We have suggested that the charge carrier mobility needs to be increased to be measurable and to consider UO_3 for neutron detection.

We explored computationally the possibility of tuning the electron effective mass (to alter the electron mobility) in UO_3 by adding a foreign atom (one among chromium, copper, molybdenum, niobium, and titanium) to increase the contribution of the cation *s*-orbitals to the conduction band. Although we did observe changes in the conduction band of the mixed crystal, the changes were too small to draw any conclusion. Finally, we studied the existence of significant polaronic effects in UO_3, which may have contributed to low electron mobility and showed mathematically that this was indeed the case. Since both the charge carrier mobility and mobility–lifetime are too low to measure exactly, UO_3 will not be very useful as a direct-conversion neutron detector material in its current state.

Future studies should include ways to mitigate the formation of hydrates by incorporating techniques such as handling of the sample in inert atmospheres only and increasing the density to near theoretical density. It is necessary to improve the charge carrier mobilities, for example by exploring the possibility of compensation doping, or using special sample fabrication techniques. Growing single crystals may help to mitigate some of the problems of charge transport properties. Therefore, it is worth exploring the methods to fabricate single crystals of UO_3. More aggressive changes (i.e., larger ranges) in stoichiometry and microstructure and their effects in the charge transport properties of UO_3 should be studied. Additionally, studies can be done on the characteristics of metal–UO_3 interface, which will be crucial for semiconductor device fabrication.

CHAPTER 6. CONCLUSION AND FUTURE WORK

In this work, uranium oxides—UO_2, U_3O_8, and UO_3—were studied in order to determine their efficacy as solid-state direct-conversion neutron detectors. Uranium oxides could become attractive materials for neutron detectors because of the massive amount of energy released during neutron-induced fission of uranium nuclei. The focus of this study was to evaluate the intrinsic charge transport properties of uranium oxides and determine the properties that would be required for these materials to act as neutron detectors. Both thermal neutrons (25 meV energy) and fast neutrons (1 and 10 MeV energies) were considered in this study.

By modeling uranium oxides as neutron detectors, we found that thicker detectors (thickness on the order of cm) would be required for fast neutrons to have a reasonable absorption probability, while slightly thinner detectors will likely work for thermal neutrons. It is also necessary to have appropriate isotopic combinations. For example, a 1 cm thick oxide of natural uranium will have a 1.5–4% absorption probability of 10 MeV neutrons. Similarly, 1 cm thick oxides of ^{235}U will have $\sim$2% absorption probability of 1 MeV neutrons. Finally, 1 cm thick oxide of depleted and natural uranium will have absorption probability of 3–4% and 7–9% respectively for thermal neutrons. Overall, the absorption probability depends on the combination of uranium isotope and energy of the neutrons.

A major source of noise in these detectors would be the leakage current originating due to the α-decay of uranium nuclei, which depends on the mass of uranium in the detector and the integration time. Therefore, in order to detect neutrons, the integration time should be limited such that the number of electron–hole pairs generated by fission fragments is greater than that generated by α-particles. However, making the integration time too short will diminish the signal. Assuming that the integration time is set equal to the transit time of the charge carriers in a detector with a cross-sectional area of 1 cm^2 and thickness of 1–10 mm, we calculated that a charge carrier mobility of 1–10 $cm^2 \cdot V^{-1} \cdot s^{-1}$ and lifetime of 10^{-4}–10^{-5} s would be required for neutron detection. The lifetime required will be lowered if the charge carrier mobility is higher. Additionally, a resistivity of $\sim 10^{12}$ Ω-cm would be ideal; however, this requirement can be lowered significantly if a correct heterostructure (such as a reverse-biased diode) can be achieved. A possible scenario may be a natural uranium oxide detector, 1 cm thick, operating at 1000 $V \cdot cm^{-1}$ with a detection efficiency of ∼2% for 10 MeV neutrons and ∼6% for thermal neutrons.

Stochiometric α-U_3O_8 pellets were fabricated and sintered to obtain stoichiometric samples with ∼95% theoretical density. The resistivity values of these samples were on the order of 10^2–10^4 Ω-cm. Similarly, non-stoichiometric α-U_3O_8 were also fabricated which were also ∼95% theoretical density. The resistivity values of these samples were on the order of 10^2–10^3 Ω-cm with the resistivity decreasing in general when the samples deviated slightly from stoichiometry. Attempts to increase the resistivity by altering the sample fabrication conditions were not successful. The charge carrier mobility could not be determined by the DC Hall effect measurements and a maximum mobility of 1 $cm^2 \cdot V^{-1} \cdot s^{-1}$ was estimated. As such, U_3O_8 will not be very useful as a neutron detector material unless the charge carrier mobility can be increased. Future studies should include advanced charge carrier mobility measurement methods to determine precisely the mobility. Also, it is important to explore the ways to improve the charge carrier mobility by techniques such as doping and/or using specialized sample fabrication techniques or growing single crystals. It is worth exploring the variation in electrical properties when the stoichiometry and microstructures are changed more aggressively. Additional future work could be to find potential dopants to make U_3O_8 a *p*-type semiconductor. This will open a path to fabricate *p*–*n* junction diode of this oxide, which may allow the fabrication reverse-biased diode neutron detectors. This will help to circumvent the problem of low resistivity of the material. Additionally, other studies such as the U_3O_8 work function, and contact types made with metal could be studied, since such information will be critical for semiconductor device fabrication.

UO_3 pellets were prepared by uniaxial hot pressing and were found to be 85–90% of theoretical density. Studies with X-ray diffraction showed that most samples consisted of ∼90% of γ-UO_3 and ∼10% α-$UO_2(OH)_2$. Most pellets were found to have a direct band gap values of ∼2 eV and indirect band gap values of ∼2.9 eV. The resistivity values of the samples were on the order of 10^9–10^{10} Ω-cm, slightly higher than the literature-reported values. No clear trends were observed between sample properties and fabrication conditions. Formation of hydrates in the pellets presented challenges in exact characterization and consequently in investigating trends and tuning the material properties. The charge carrier mobility could not be determined exactly; instead a maximum value on the order of 10^{-3}–10^{-2} $cm^2 \cdot V^{-1} \cdot s^{-1}$ was estimated. The reason behind such small charge carrier mobility has been linked to polaronic effects in UO_3. The charge carrier mobility needs to be improved in order to consider UO_3 as a detector material. We did some computational studies to explore the effects on the conduction band of UO_3 on mixing of foreign elements, however the changes were too tiny to draw any conclusions.

The future studies of UO_3 could be the studies like those suggested for U_3O_8 (*vide supra*). The main study should be focused in increasing the charge carrier mobility of the material. There could potentially be novel techniques to fabricate samples with better charge transport properties. For example, the charge carrier mobility of UO_2 was improved by about two orders-of-magnitude by growing single crystals by hydrothermal synthesis [196]. Other future studies should include the study of hydrates formation and developing fabrication process that minimizes the hydration of UO_3. This may be achievable by increasing the densification of the pellets.

Since the charge transport properties of U_3O_8 and UO_3 do not currently meet the requirements for neutron detection, these materials will not be much useful in the forms prepared. However, the possibility of improving charge transport properties should be explored, which may provide a way of using these materials for direct-conversion neutron detection.

APPENDIX A: EXAMPLE VASP INPUT FILES

INCAR file

```
System = Gamma-UO3

Electronic and Ionic Optimization:

PREC = Normal       ! Determines precision
ALGO   = Normal     ! Determines electronic minimization algorithm (blocked
Davidson iteration scheme).
ENCUT = 500 eV    ! Cut-off energy.
EDIFF = 1.0E-6    ! Energy difference convergence limit for electronic optimization.
EDIFFG = -0.01 ! Energy difference convergence limit for ionic optimization
IBRION = 2        ! Ionic relaxation algorithm (Conjugate gradient algorithm)
NSW    = 1200      ! Number of ionic steps.
ISIF   = 3        ! Principal degrees of freedom.
GGA = PE          ! Determines GGA functional used (Perdew-Burke-Ernzerhof)
ISPIN = 2         !Spin polarized calculation
NBLOCK = 1        ! Determines how often pair correlation function and DOS are
calculated
KBLOCK = 50       ! Determines ionic relaxation algorithm (conjugate gradients)
IWAVPR =1         ! Determines how charge density is extrapolated between ionic steps
ISYM = 0 ! Turn off symmetry

DOS related:
ISMEAR = 0        ! Gaussian Smearing
SIGMA = 0.10      ! Determines smearing width
NEDOS =3001 ! Specific number of gridpoints on which the DOS is evaluated.

Miscellaneous:
LORBIT = 11       ! Controls writing of output PROCAR with site projected
wavefunctions
LASPH =  T        ! Includes non-spherical contributions form gradient corrections

DFT+U Calculations:
LDAU = T          ! Turns on DFT+U
LDAUTYPE = 2      ! Determines DFT+U type Dudarev
LDAUL = 3 -1      ! L quantum numbers for each species using DFT+U, f not used
LDAUU = 4.50 0.00 ! U portion of Hubbard coefficient for each species
LDAUJ = 0.54 0.00 ! J portion of Hubbard coefficient for each species
LDAUPRINT = 2     ! Verbosity of output, in OUTCAR, writes occupancy matrix
LMAXMIX = 6       ! Mixing parameter, set for f electrons, to give fast convergence

Magnetic Calculations:
```

```
MAGMOM = 2 -2 2 -2 2 -2 2 -2 2 -2 2 -2 2 -2 2 -2 48*0
```

KPOINT file

```
G
0 ! 0 means automatic generation scheme
G ! G means gamma centered grid
6   6   2 ! Subdivisions along the reciprocal lattice vectors
0   0   0 ! Optional shift of the mesh
```

POSCAR file

```
O3 U
1.0
       6.9012999535         0.0000000000         0.0000000000
       0.0000000000         6.9012999535         0.0000000000
       0.0000000000         0.0000000000        19.9754009247
    U    O
   16   48
Direct
     0.000000000         0.250000000         0.061799999
     0.000000000         0.750000000         0.938199997
     0.500000000         0.750000000         0.561800003
     0.500000000         0.250000000         0.438199997
     0.000000000         0.750000000         0.311800003
     0.000000000         0.250000000         0.688199997
     0.500000000         0.250000000         0.811800003
     0.500000000         0.750000000         0.188199997
     0.000000000         0.000000000         0.500000000
     0.500000000         0.000000000         0.000000000
     0.250000000         0.750000000         0.750000000
     0.750000000         0.250000000         0.250000000
     0.250000000         0.250000000         0.250000000
     0.750000000         0.750000000         0.750000000
     0.500000000         0.500000000         0.000000000
     0.000000000         0.500000000         0.500000000
     0.000000000         0.049600001         0.264499992
     0.000000000         0.950399995         0.735499978
     0.500000000         0.950399995         0.764500022
     0.500000000         0.049600001         0.235500008
     0.200399995         0.750000000         0.514500022
     0.799600005         0.250000000         0.485500008
     0.299600005         0.250000000         0.014499992
     0.700399995         0.750000000         0.985499978
     0.299600005         0.750000000         0.985499978
```

0.700399995	0.250000000	0.014499992
0.200399995	0.250000000	0.485500008
0.799600005	0.750000000	0.514500022
0.500000000	0.549600005	0.764500022
0.500000000	0.450399995	0.235500008
0.000000000	0.450399995	0.264499992
0.000000000	0.549600005	0.735499978
0.000000000	0.947600007	0.407299995
0.000000000	0.052399993	0.592700005
0.500000000	0.052399993	0.907299995
0.500000000	0.947600007	0.092700005
0.302399993	0.750000000	0.657299995
0.697600007	0.250000000	0.342700005
0.197600007	0.250000000	0.157299995
0.802399993	0.750000000	0.842700005
0.197600007	0.750000000	0.842700005
0.802399993	0.250000000	0.157299995
0.302399993	0.250000000	0.342700005
0.697600007	0.750000000	0.657299995
0.500000000	0.447600007	0.907299995
0.500000000	0.552399993	0.092700005
0.000000000	0.552399993	0.407299995
0.000000000	0.447600007	0.592700005
0.000000000	0.509999990	0.066000000
0.000000000	0.490000010	0.934000015
0.500000000	0.490000010	0.565999985
0.500000000	0.509999990	0.434000015
0.740000010	0.750000000	0.315999985
0.259999990	0.250000000	0.684000015
0.759999990	0.250000000	0.815999985
0.240000010	0.750000000	0.184000000
0.759999990	0.750000000	0.184000000
0.240000010	0.250000000	0.815999985
0.740000010	0.250000000	0.684000015
0.259999990	0.750000000	0.315999985
0.500000000	0.009999990	0.565999985
0.500000000	0.990000010	0.434000015
0.000000000	0.990000010	0.066000000
0.000000000	0.009999990	0.934000015

APPENDIX B: I–V MEASUREMENTS ON U_3O_8

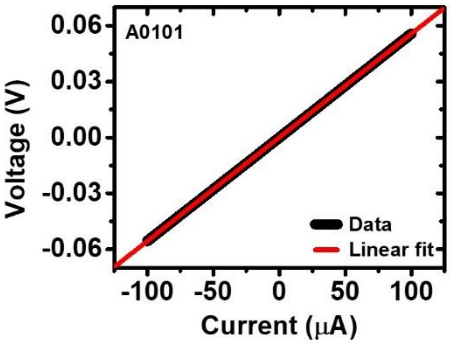

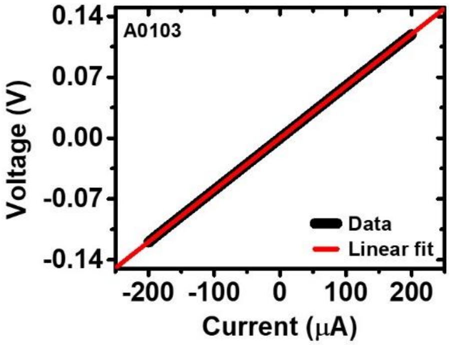

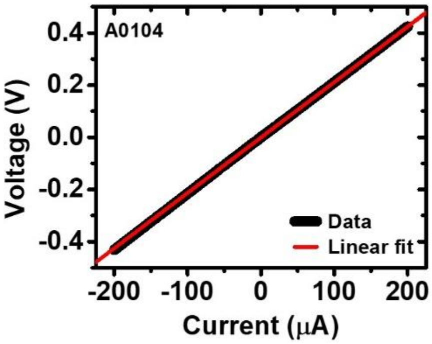

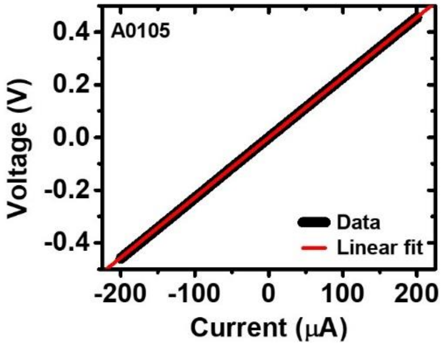

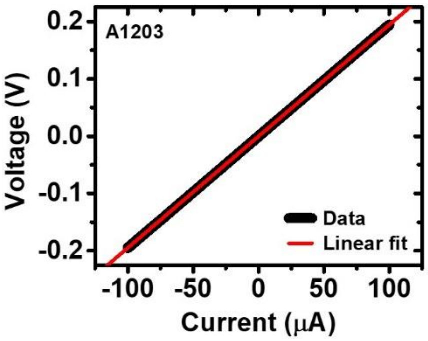

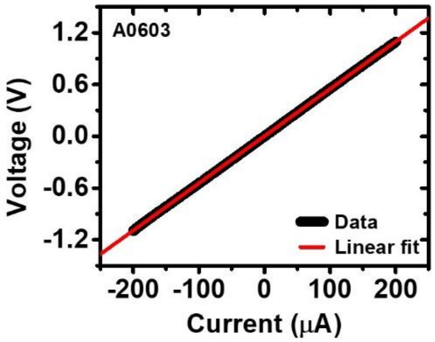

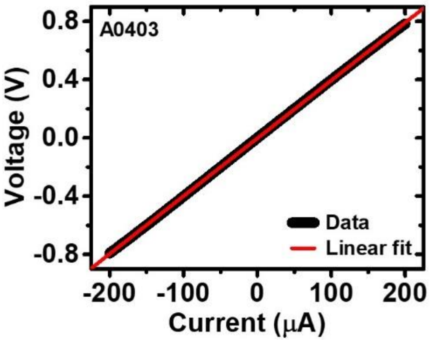

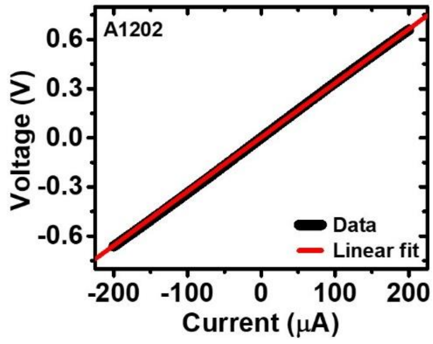

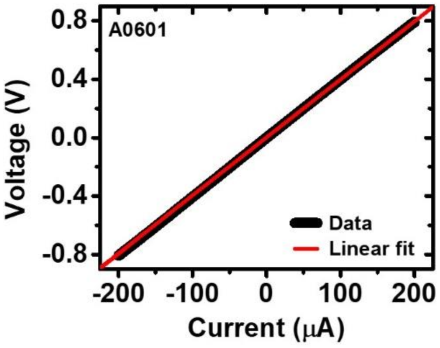
A0601
Voltage (V)
0.8
0.4
0.0
-0.4
-0.8
Data
Linear fit
-200
-100
0
100
200
Current (μA)

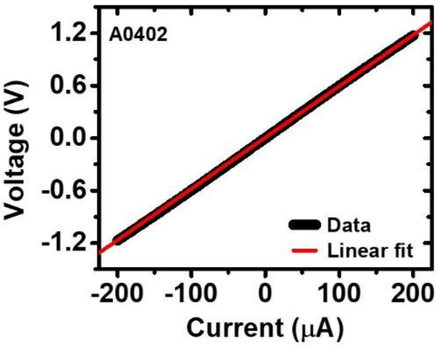
A0402
Voltage (V)
1.2
0.6
0.0
-0.6
-1.2
Data
Linear fit
-200
-100
0
100
200
Current (μA)

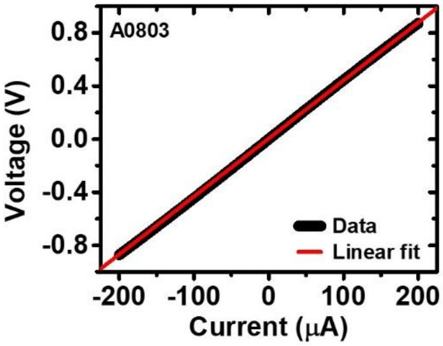
A0803
Voltage (V)
0.8
0.4
0.0
-0.4
-0.8
Data
Linear fit
-200
-100
0
100
200
Current (μA)

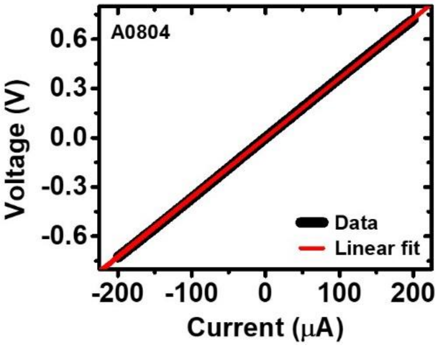
A0804
Voltage (V)
0.6
0.3
0.0
-0.3
-0.6
Data
Linear fit
-200
-100
0
100
200
Current (μA)

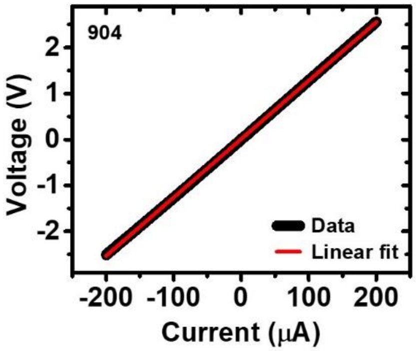
904
Voltage (V)
2
1
0
-1
-2
Data
Linear fit
-200
-100
0
100
200
Current (μA)

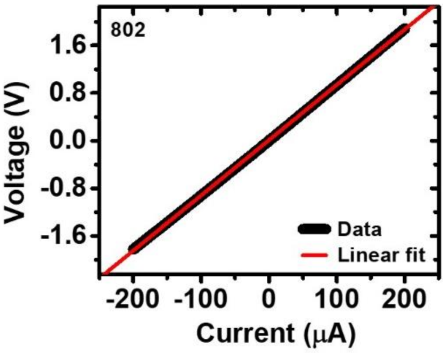
802
Voltage (V)
1.6
0.8
0.0
-0.8
-1.6
Data
Linear fit
-200
-100
0
100
200
Current (μA)

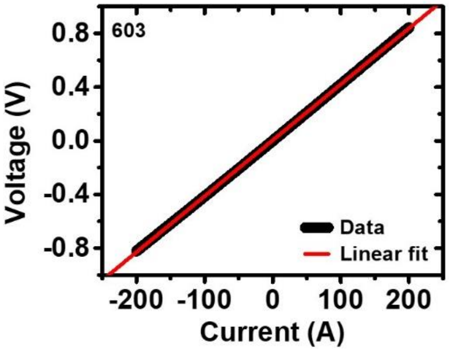
603
Voltage (V)
0.8
0.4
0.0
-0.4
-0.8
Data
Linear fit
-200
-100
0
100
200
Current (A)

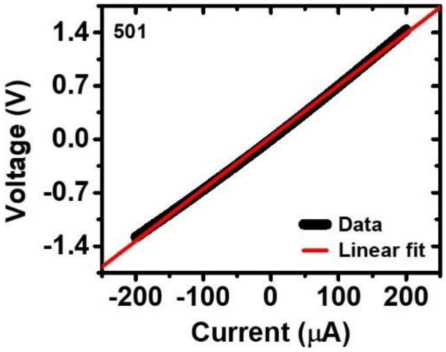
501
Voltage (V)
1.4
0.7
0.0
-0.7
-1.4
Data
Linear fit
-200
-100
0
100
200
Current (μA)

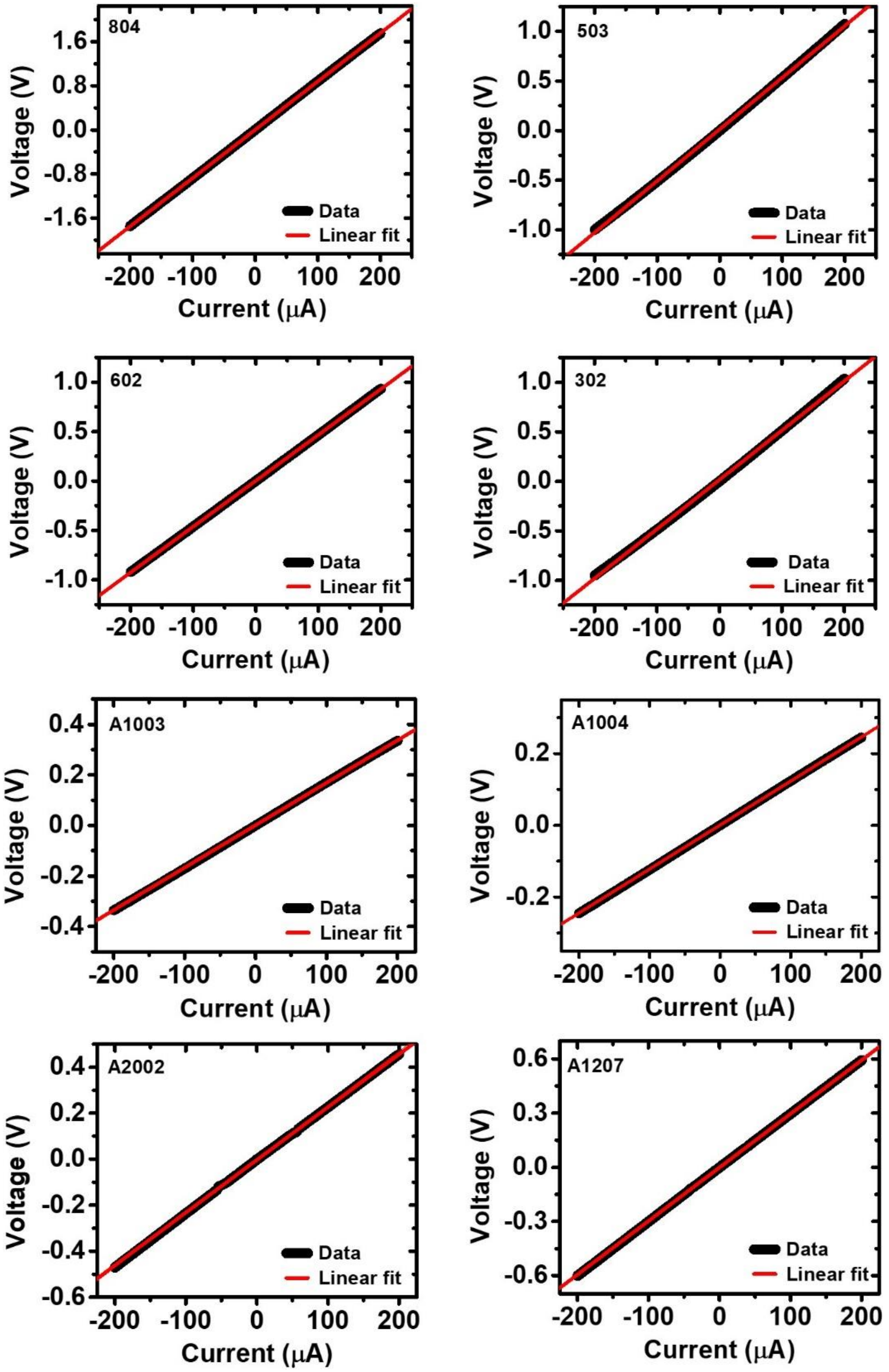
804
1.6
0.8
0.0
-0.8
-1.6
Voltage (V)
-200 -100 0 100 200
Current (μA)
Data
Linear fit
503
1.0
0.5
0.0
-0.5
-1.0
Voltage (V)
-200 -100 0 100 200
Current (μA)
Data
Linear fit
602
1.0
0.5
0.0
-0.5
-1.0
Voltage (V)
-200 -100 0 100 200
Current (μA)
Data
Linear fit
302
1.0
0.5
0.0
-0.5
-1.0
Voltage (V)
-200 -100 0 100 200
Current (μA)
Data
Linear fit
A1003
0.4
0.2
0.0
-0.2
-0.4
Voltage (V)
-200 -100 0 100 200
Current (μA)
Data
Linear fit
A1004
0.2
0.0
-0.2
Voltage (V)
-200 -100 0 100 200
Current (μA)
Data
Linear fit
A2002
0.4
0.2
0.0
-0.2
-0.4
-0.6
Voltage (V)
-200 -100 0 100 200
Current (μA)
Data
Linear fit
A1207
0.6
0.3
0.0
-0.3
-0.6
Voltage (V)
-200 -100 0 100 200
Current (μA)
Data
Linear fit

APPENDIX C: HALL EFFECT MEASUREMENTS ON U_3O_8

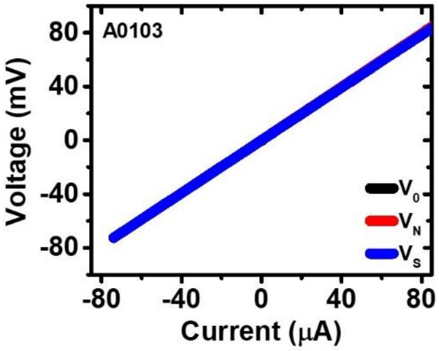

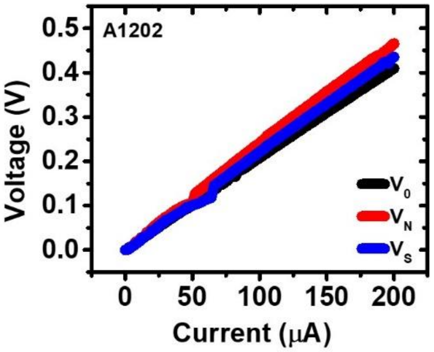

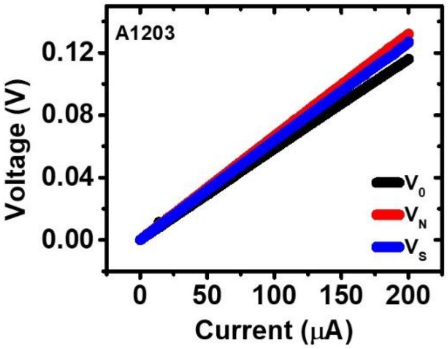

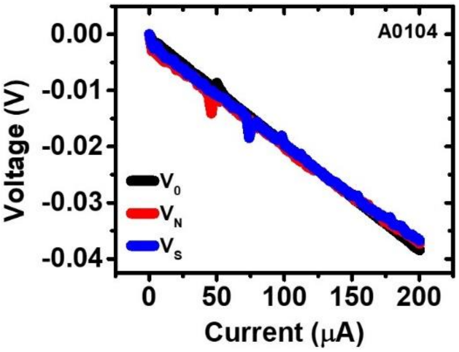

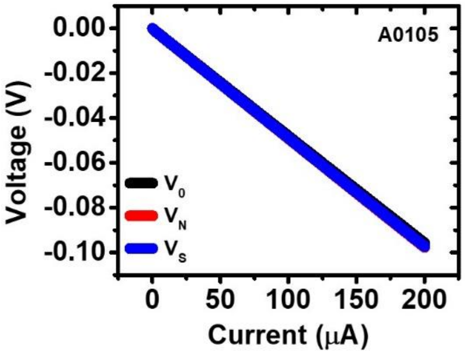

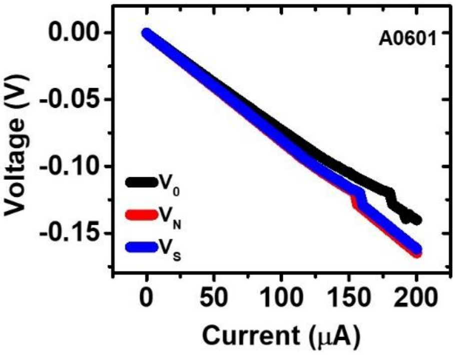

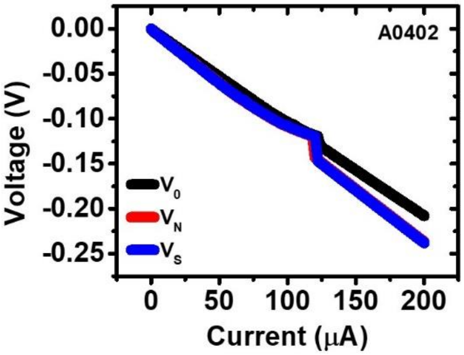

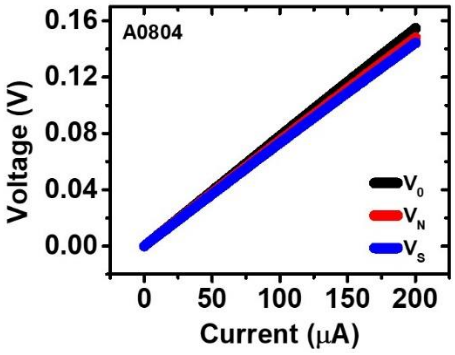

APPENDIX D: BAND GAP ANALYSIS OF UO_3

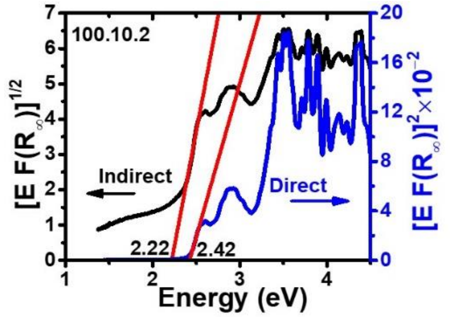

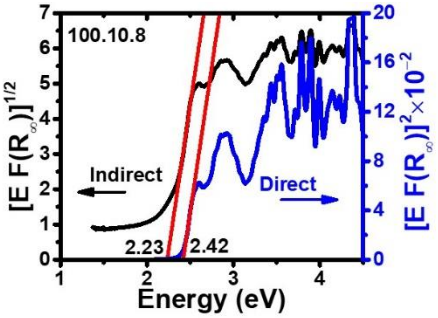

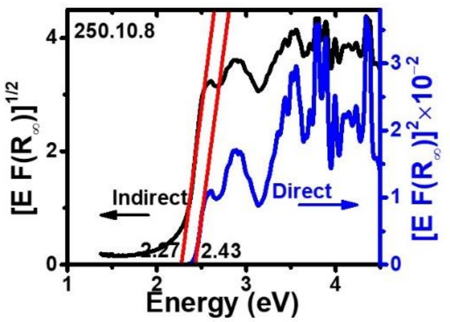

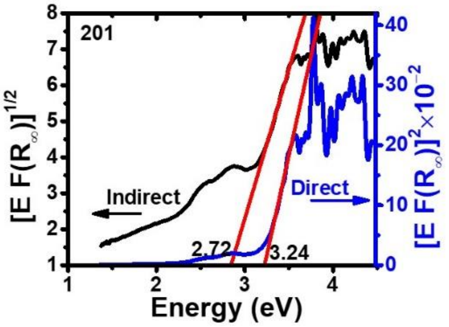

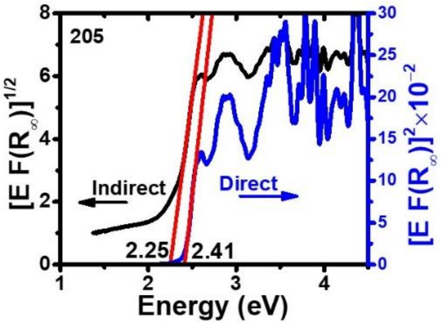

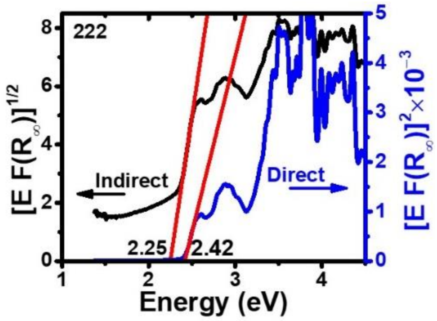

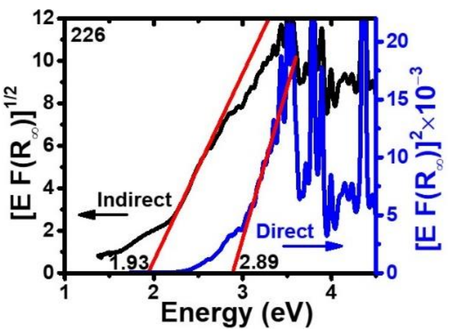

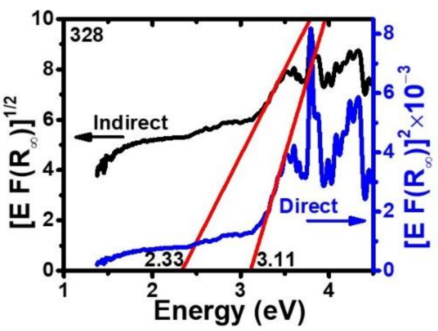

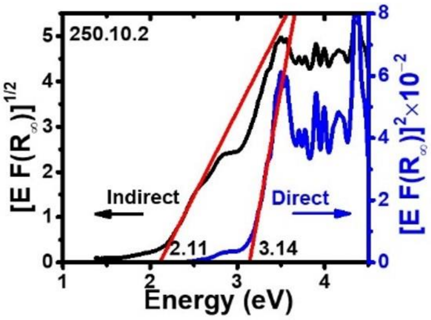
250.10.2
[E F(R∞)]^1/2
[E F(R∞)]^2×10^−2
Indirect
Direct
2.11
3.14
Energy (eV)
0
1
2
3
4
5
2
4
6
8

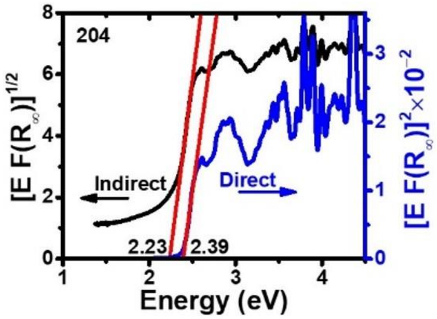
204
[E F(R∞)]^1/2
[E F(R∞)]^2×10^−2
Indirect
Direct
2.23
2.39
Energy (eV)
0
2
4
6
8
1
2
3

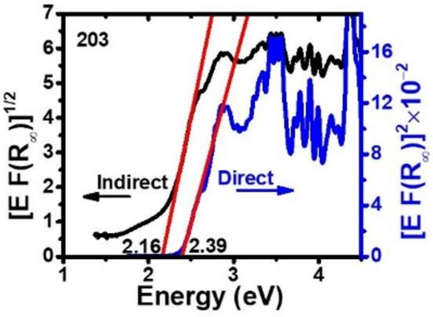
203
[E F(R∞)]^1/2
[E F(R∞)]^2×10^−2
Indirect
Direct
2.16
2.39
Energy (eV)
0
1
2
3
4
5
6
7
4
8
12
16

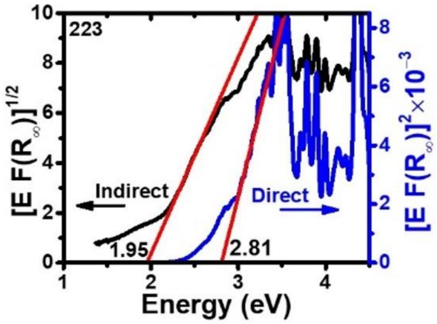
223
[E F(R∞)]^1/2
[E F(R∞)]^2×10^−3
Indirect
Direct
1.95
2.81
Energy (eV)
0
2
4
6
8
10
2
4
6
8

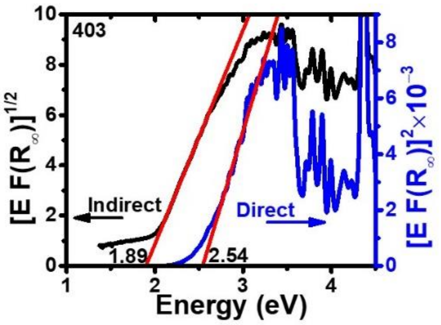
403
[E F(R∞)]^1/2
[E F(R∞)]^2×10^−3
Indirect
Direct
1.89
2.54
Energy (eV)
0
2
4
6
8
10
2
4
6
8

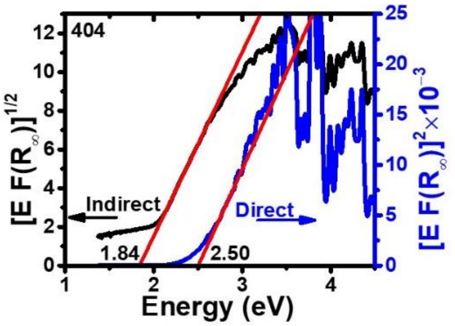
404
[E F(R∞)]^1/2
[E F(R∞)]^2×10^−3
Indirect
Direct
1.84
2.50
Energy (eV)
0
2
4
6
8
10
12
5
10
15
20
25

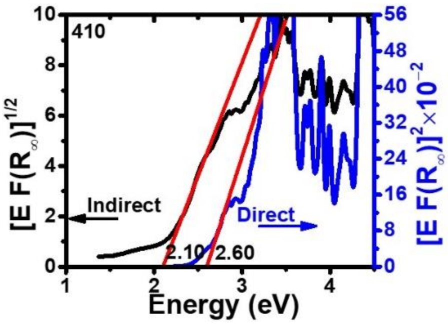
410
[E F(R∞)]^1/2
[E F(R∞)]^2×10^−2
Indirect
Direct
2.10
2.60
Energy (eV)
0
2
4
6
8
10
8
16
24
32
40
48
56

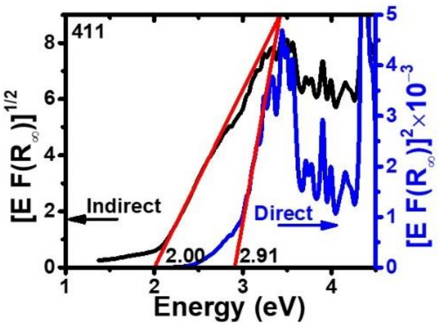
411
[E F(R∞)]^1/2
[E F(R∞)]^2×10^−3
Indirect
Direct
2.00
2.91
Energy (eV)
0
2
4
6
8
1
2
3
4
5

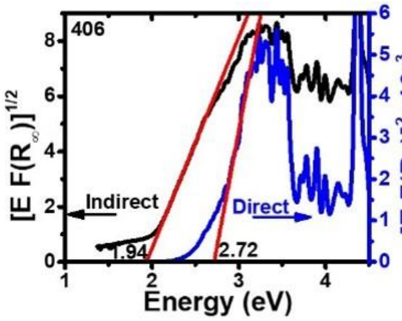
406
[E F(R∞)]^1/2
[E F(R∞)]^2×10^−3
Indirect
Direct
1.94
2.72
Energy (eV)
0
2
4
6
8
1
2
3
4
0
1
2
3
4
5
6

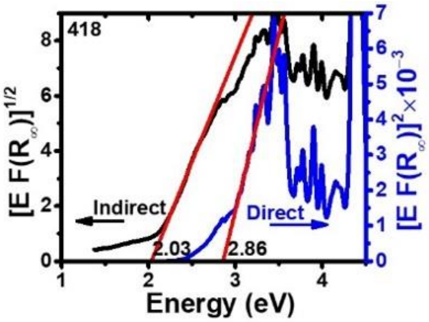
418
[E F(R∞)]^1/2
[E F(R∞)]^2×10^−3
Indirect
Direct
2.03
2.86
Energy (eV)
0
2
4
6
8
1
2
3
4
0
1
2
3
4
5
6
7

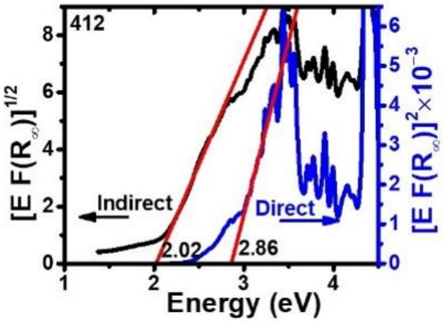
412
[E F(R∞)]^1/2
[E F(R∞)]^2×10^−3
Indirect
Direct
2.02
2.86
Energy (eV)
0
2
4
6
8
1
2
3
4
0
1
2
3
4
5
6

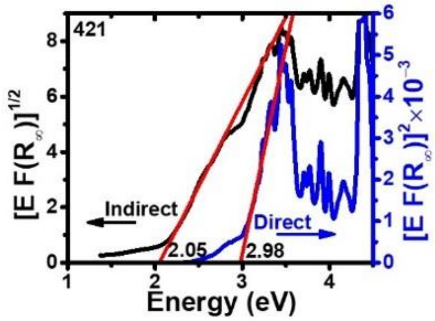
421
[E F(R∞)]^1/2
[E F(R∞)]^2×10^−3
Indirect
Direct
2.05
2.98
Energy (eV)
0
2
4
6
8
1
2
3
4
0
1
2
3
4
5
6

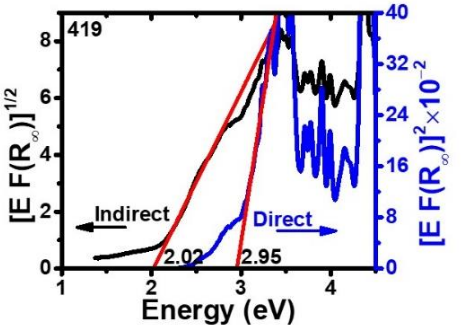
419
[E F(R∞)]^1/2
[E F(R∞)]^2×10^−2
Indirect
Direct
2.02
2.95
Energy (eV)
0
2
4
6
8
1
2
3
4
0
8
16
24
32
40

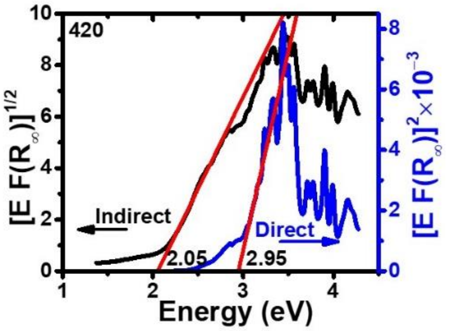
420
[E F(R∞)]^1/2
[E F(R∞)]^2×10^−3
Indirect
Direct
2.05
2.95
Energy (eV)
0
2
4
6
8
10
1
2
3
4
0
2
4
6
8

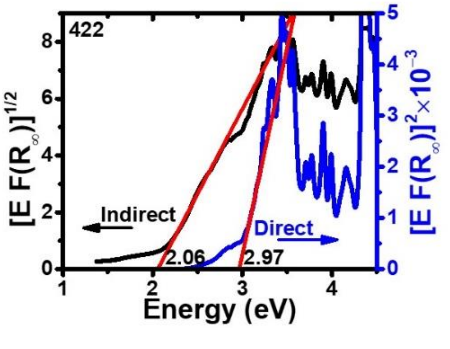
422
[E F(R∞)]^1/2
[E F(R∞)]^2×10^−3
Indirect
Direct
2.06
2.97
Energy (eV)
0
2
4
6
8
1
2
3
4
0
1
2
3
4
5

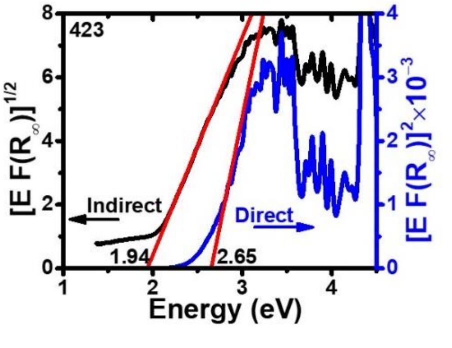
423
[E F(R∞)]^1/2
[E F(R∞)]^2×10^−3
Indirect
Direct
1.94
2.65
Energy (eV)
0
2
4
6
8
1
2
3
4
0
1
2
3
4

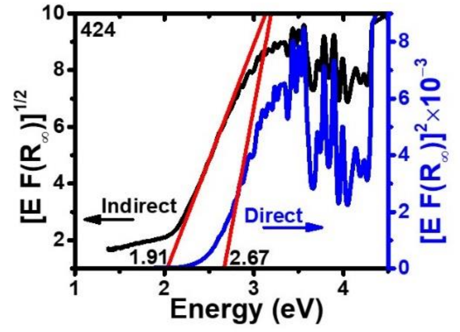
424
[E F(R$_\infty$)]$^{1/2}$
[E F(R$_\infty$)]^2×10^{-3}
Energy (eV)
Indirect
Direct
1.91
2.67

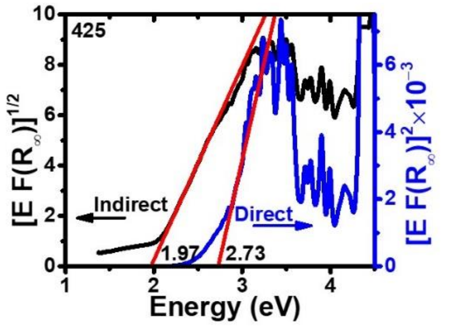
425
[E F(R$_\infty$)]$^{1/2}$
[E F(R$_\infty$)]^2×10^{-3}
Energy (eV)
Indirect
Direct
1.97
2.73

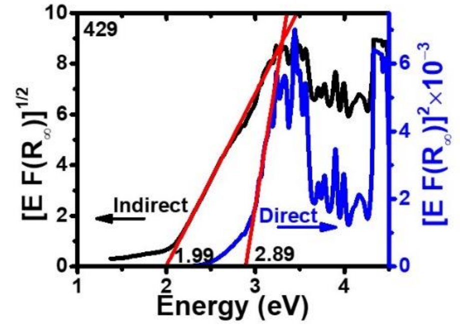
429
[E F(R$_\infty$)]$^{1/2}$
[E F(R$_\infty$)]^2×10^{-3}
Energy (eV)
Indirect
Direct
1.99
2.89

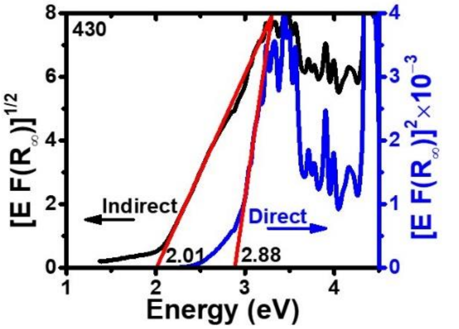
430
[E F(R$_\infty$)]$^{1/2}$
[E F(R$_\infty$)]^2×10^{-3}
Energy (eV)
Indirect
Direct
2.01
2.88

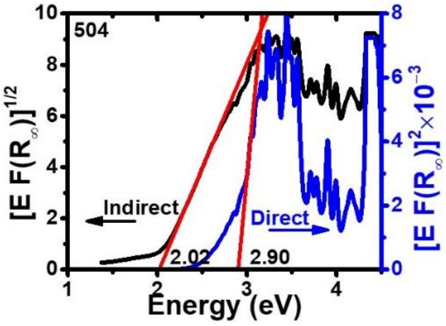
504
[E F(R$_\infty$)]$^{1/2}$
[E F(R$_\infty$)]^2×10^{-3}
Energy (eV)
Indirect
Direct
2.02
2.90

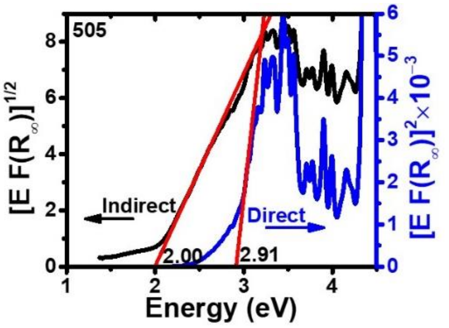
505
[E F(R$_\infty$)]$^{1/2}$
[E F(R$_\infty$)]^2×10^{-3}
Energy (eV)
Indirect
Direct
2.00
2.91

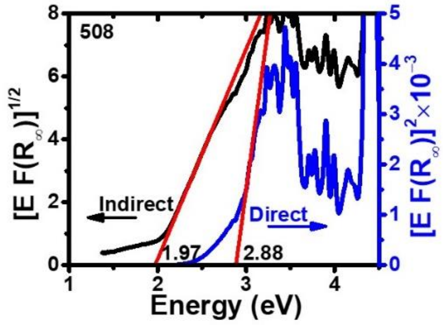
508
[E F(R$_\infty$)]$^{1/2}$
[E F(R$_\infty$)]^2×10^{-3}
Energy (eV)
Indirect
Direct
1.97
2.88

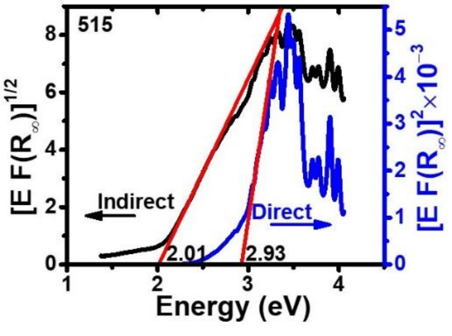
515
[E F(R$_\infty$)]$^{1/2}$
[E F(R$_\infty$)]^2×10^{-3}
Energy (eV)
Indirect
Direct
2.01
2.93

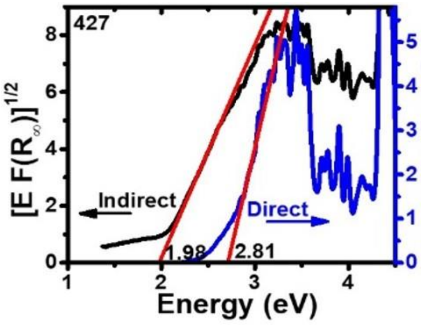
427
[E F(R$_\infty$)]$^{1/2}$
[E F(R$_\infty$)]^2×10^{-3}
Indirect
Direct
1.98
2.81
Energy (eV)
0
2
4
6
8
1
2
3
4
0
1
2
3
4
5

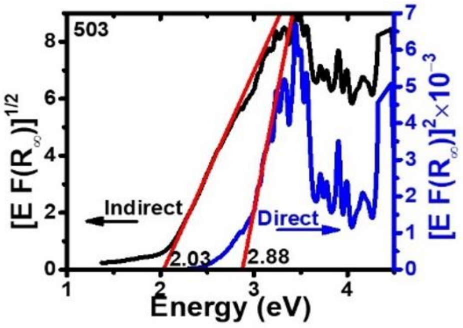
503
[E F(R$_\infty$)]$^{1/2}$
[E F(R$_\infty$)]^2×10^{-3}
Indirect
Direct
2.03
2.88
Energy (eV)
0
2
4
6
8
1
2
3
4
0
1
2
3
4
5
6
7

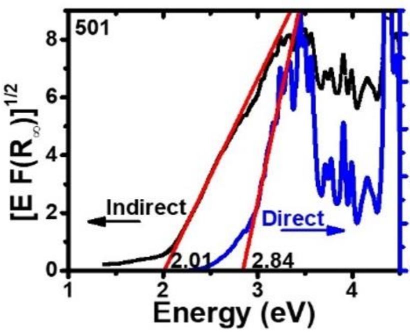
501
[E F(R$_\infty$)]$^{1/2}$
[E F(R$_\infty$)]^2×10^{-3}
Indirect
Direct
2.01
2.84
Energy (eV)
0
2
4
6
8
1
2
3
4
0
1
2
3
4
5

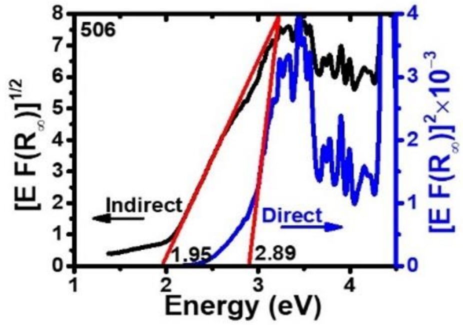
506
[E F(R$_\infty$)]$^{1/2}$
[E F(R$_\infty$)]^2×10^{-3}
Indirect
Direct
1.95
2.89
Energy (eV)
0
1
2
3
4
5
6
7
8
1
2
3
4
0
1
2
3
4

APPENDIX E: I–V MEASUREMENTS ON UO_3

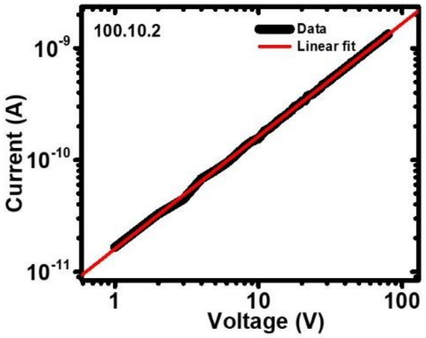

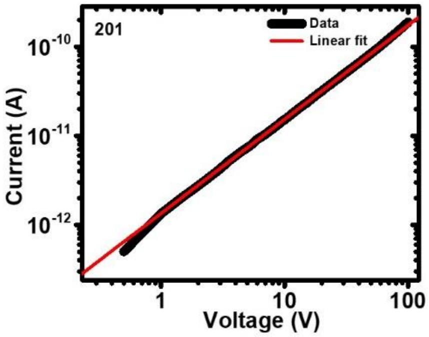

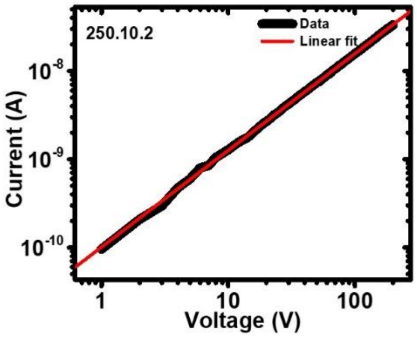

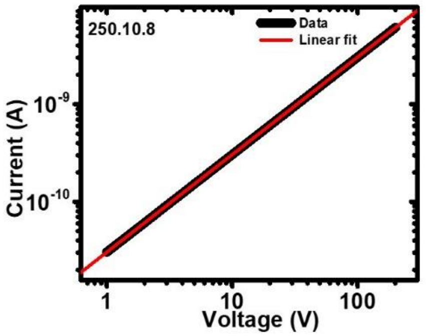

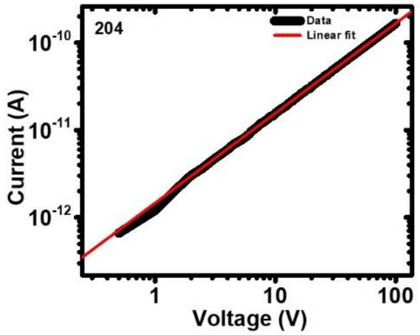

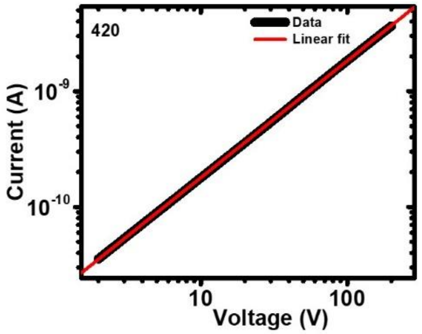

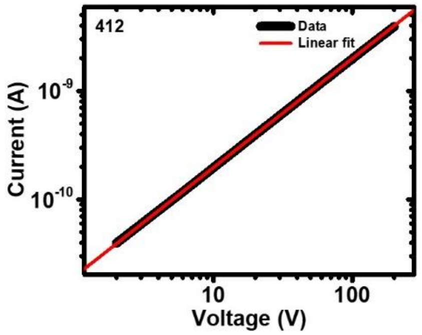

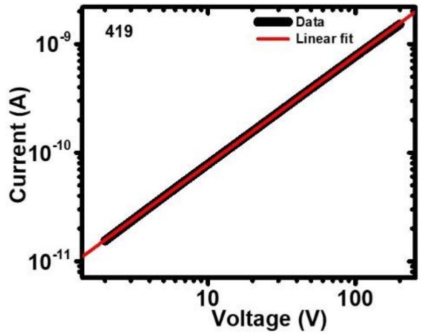

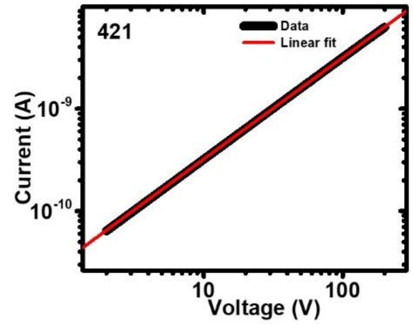
421
Data
Linear fit
Current (A)
10^{-9}
10^{-10}
10
100
Voltage (V)

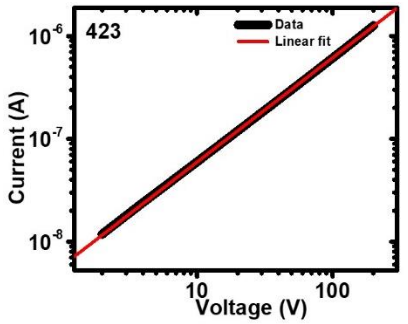
423
Data
Linear fit
Current (A)
10^{-6}
10^{-7}
10^{-8}
10
100
Voltage (V)

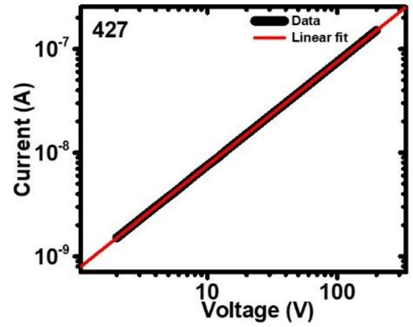
427
Data
Linear fit
Current (A)
10^{-7}
10^{-8}
10^{-9}
10
100
Voltage (V)

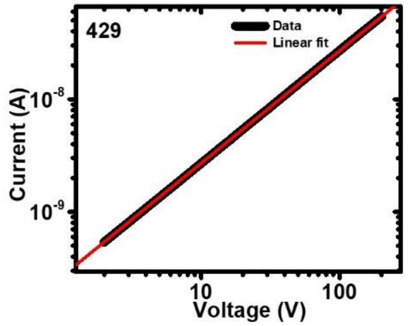
429
Data
Linear fit
Current (A)
10^{-8}
10^{-9}
10
100
Voltage (V)

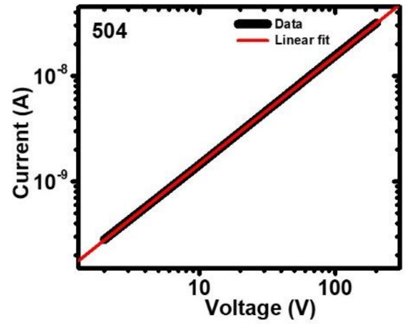
504
Data
Linear fit
Current (A)
10^{-8}
10^{-9}
10
100
Voltage (V)

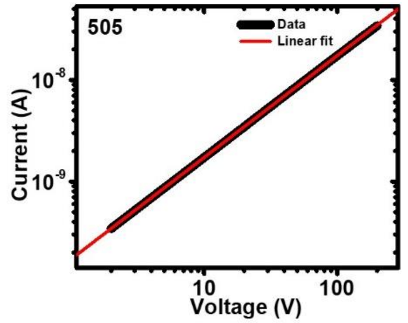
505
Data
Linear fit
Current (A)
10^{-8}
10^{-9}
10
100
Voltage (V)

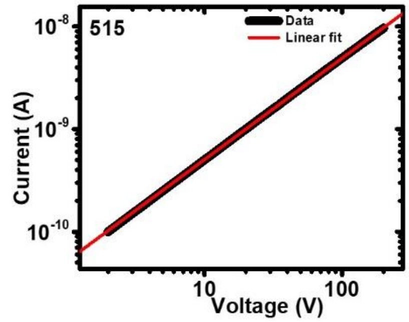
515
Data
Linear fit
Current (A)
10^{-8}
10^{-9}
10^{-10}
10
100
Voltage (V)

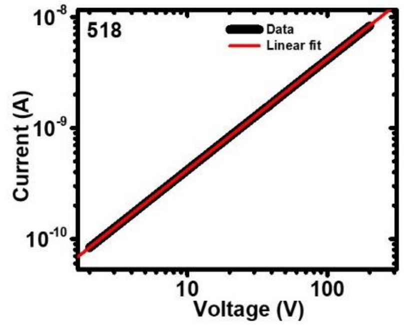
518
Data
Linear fit
Current (A)
10^{-8}
10^{-9}
10^{-10}
10
100
Voltage (V)

APPENDIX F: HIGH VOLTAGE MEASUREMENTS ON UO$_3$

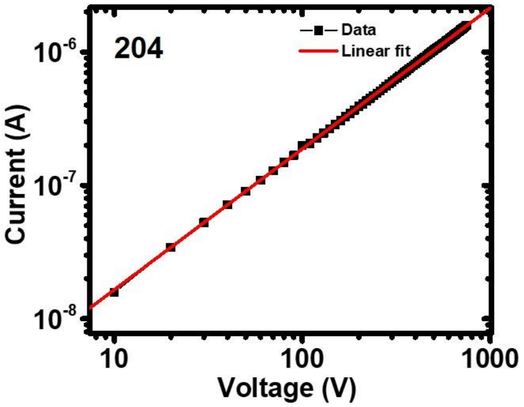

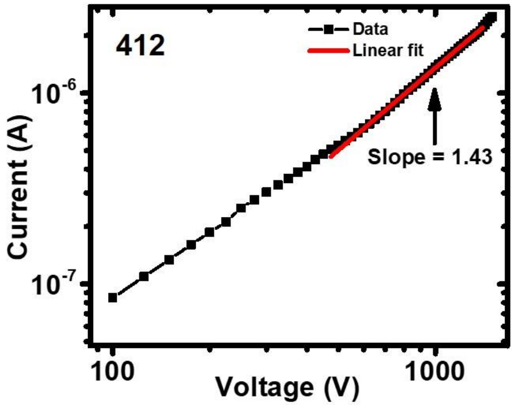

APPENDIX G: ELECTRONIC STRUCTURE OF MIXED CRYSTALS OF UO$_3$

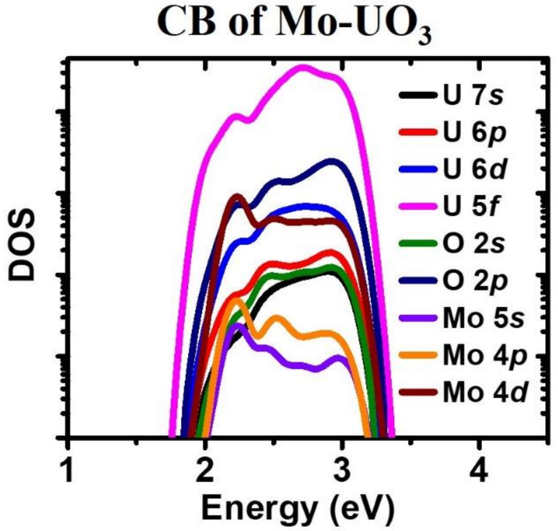
CB of Mo-UO$_3$

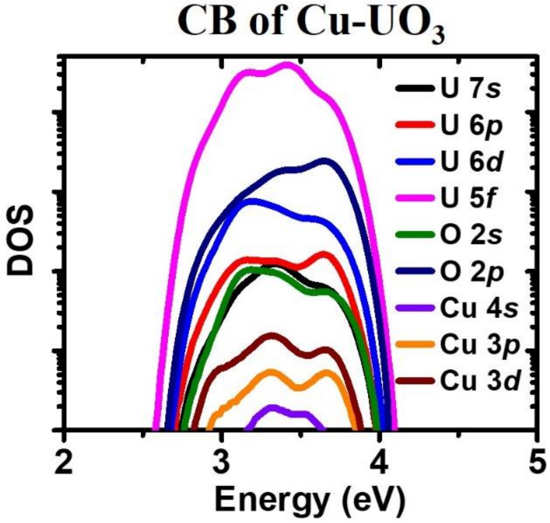
CB of Cu-UO$_3$

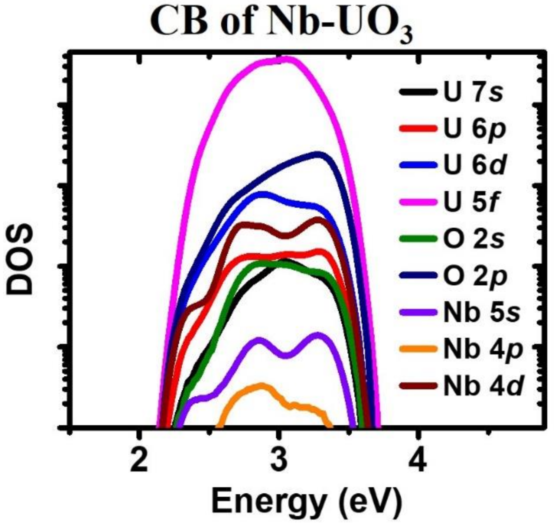
CB of Nb-UO$_3$

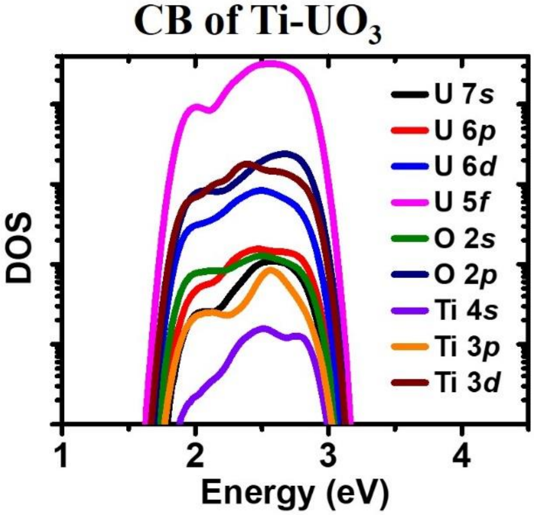
CB of Ti-UO$_3$

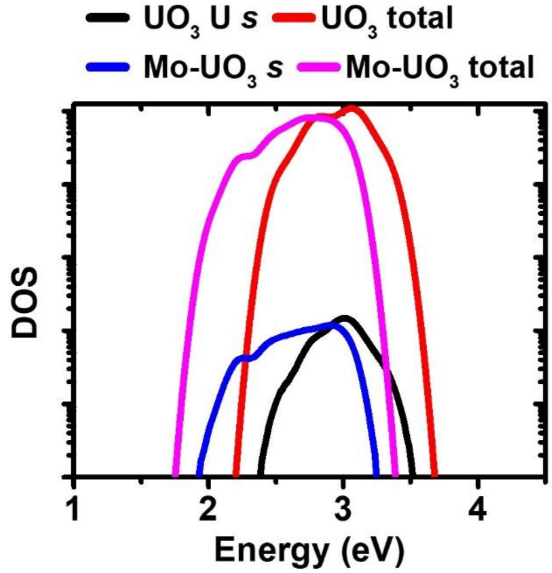
UO_3 U *s*
UO_3 total
Mo-UO_3 *s*
Mo-UO_3 total
DOS
1
2
3
4
Energy (eV)

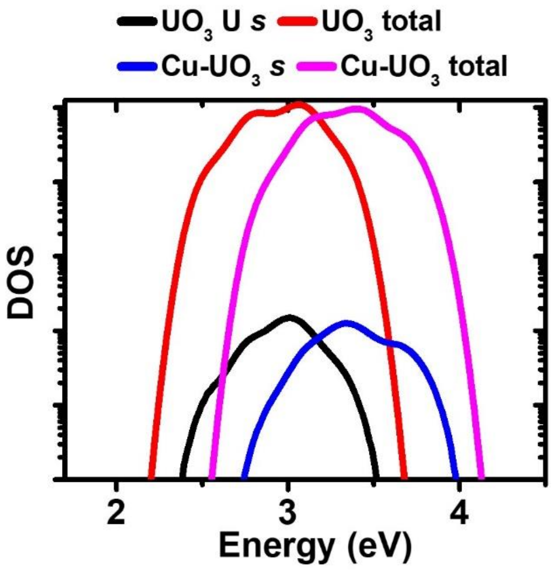
UO_3 U *s*
UO_3 total
Cu-UO_3 *s*
Cu-UO_3 total
DOS
2
3
4
Energy (eV)

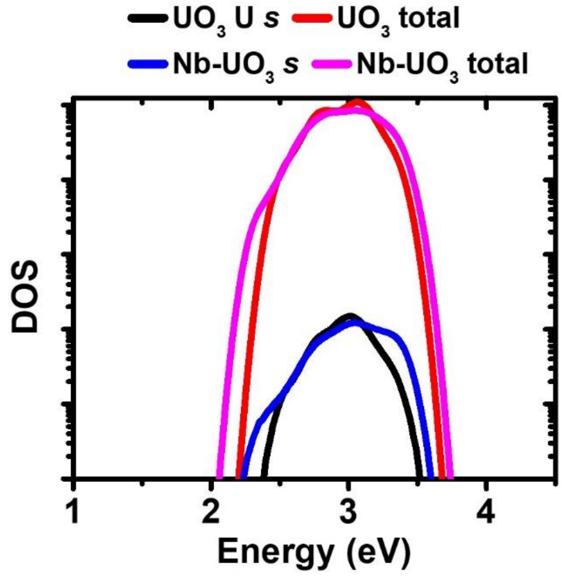
UO_3 U *s*
UO_3 total
Nb-UO_3 *s*
Nb-UO_3 total
DOS
1
2
3
4
Energy (eV)

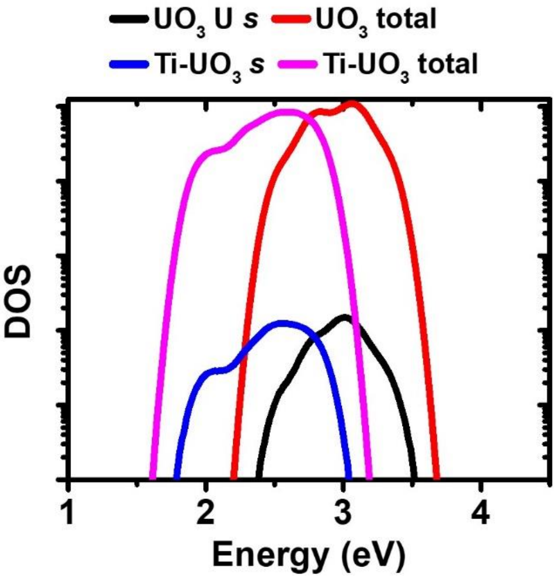
UO_3 U *s*
UO_3 total
Ti-UO_3 *s*
Ti-UO_3 total
DOS
1
2
3
4
Energy (eV)

REFERENCES

[1] T. Elevant, B. Wolle, and A. Weller, “Proposed neutron diagnostics for Wendelstein 7-X stellarator,” *Rev. Sci. Instrum.*, vol. 70, no. 1, pp. 1185–1189, Jan. 1999. doi: 10.1063/1.1149321.

[2] L. C. Johnson, C. W. Barnes, A. Krasilnikov, F. B. Marcus, and T. Nishitani, “Neutron diagnostics for ITER,” *Rev. Sci. Instrum.*, vol. 68, no. 1, pp. 569–572, 1997. doi: 10.1063/1.1147906.

[3] D. R. Kania, S. Lane, B. Jones, C. Bennett, S. Prussin, and M. Derzon, “High speed detection of thermonuclear neutrons with solid state detectors,” *IEEE Trans. Nucl. Sci.*, vol. 35, no. 1, pp. 387–388, Feb. 1988. doi: 10.1109/23.12749.

[4] F. H. Ruddy, A. R. Dulloo, T. V. Congedo, and J. G. Seidel, “Monitoring of Neutron and Gamma Radiation,” USPTO 5,969,359, 1999.

[5] S. Fetter *et al.*, “Detecting nuclear warheads,” *Sci. Glob. Secur.*, vol. 1, no. 3–4, pp. 225–253, Jan. 1990. doi: 10.1080/08929889008426333.

[6] T. Matsumoto and O. Aizawa, “Dose measuring system for boron neutron capture therapy,” *Nucl. Inst. Methods Phys. Res. A*, vol. 271, no. 3, pp. 662–670, 1988. doi: 10.1016/0168-9002(88)90337-3.

[7] C. Sunil, A. Saxena, R. K. Choudhury, and L. M. Pant, “Neutron yield and dose equivalent from heavy ion interactions on thick target,” *Nucl. Instruments Methods Phys. Res. Sect. A Accel. Spectrometers, Detect. Assoc. Equip.*, vol. 534, no. 3, pp. 518–530, Dec. 2004. doi: 10.1016/j.nima.2004.06.131.

[8] W. C. Feldman *et al.*, “The Lunar Prospector gamma-ray and neutron spectrometers,” *Nucl. Instruments Methods Phys. Res. Sect. A Accel. Spectrometers, Detect. Assoc. Equip.*, vol. 422, no. 1–3, pp. 562–566, Feb. 1999. doi: 10.1016/S0168-9002(98)00934-6.

[9] M. Takada, S. Taniguchi, T. Nakamura, and K. Fujitaka, “Development of a phoswich detector to detect neutrons and charged particles for space application,” *IEEE Trans. Nucl. Sci.*, vol. 45, no. 3, pp. 888–893, Jun. 1998. doi:

10.1109/23.682656.

[10] E. O. Wollan and C. G. Shull, “The diffraction of neutrons by crystalline powders,” *Phys. Rev.*, vol. 73, no. 8, pp. 830–841, 1948. doi: 10.1103/PhysRev.73.830.

[11] A. J. Peurrung, “Recent developments in neutron detection,” *Nucl. Instruments Methods Phys. Res. Sect. A Accel. Spectrometers, Detect. Assoc. Equip.*, vol. 443, no. 2–3, pp. 400–415, Apr. 2000. doi: 10.1016/S0168-9002(99)01165-1.

[12] Y. Danon *et al.*, “Towards high efficiency solid-state thermal and fast neutron detectors,” *J. Instrum.*, vol. 7, no. 03, pp. C03014–C03014, Mar. 2012. doi: 10.1088/1748-0221/7/03/C03014.

[13] R. J. Nikolic, C. L. Cheung, C. E. Reinhardt, and T. F. Wang, “Roadmap for high efficiency solid-state neutron detectors,” in *Proceedings of SPIR - Volume 6013: Optoelectronic Devices: Physics, Fabrication, and Application II*, 2005, vol. 6013, p. 601305. doi: 10.1117/12.633256.

[14] P. Chaudhari, A. Singh, A. Topkar, and R. Dusane, “Fabrication and characterization of silicon based thermal neutron detector with hot wire chemical vapor deposited boron carbide converter,” *Nucl. Instruments Methods Phys. Res. Sect. A Accel. Spectrometers, Detect. Assoc. Equip.*, vol. 779, pp. 33–38, Apr. 2015. doi: 10.1016/j.nima.2015.01.043.

[15] R. T. Kouzes *et al.*, “Neutron detection alternatives to 3He for national security applications,” *Nucl. Instruments Methods Phys. Res. Sect. A Accel. Spectrometers, Detect. Assoc. Equip.*, vol. 623, no. 3, pp. 1035–1045, Nov. 2010. doi: 10.1016/j.nima.2010.08.021.

[16] D. Henzlova *et al.*, “Current Status of Helium-3 Alternative Technologies for Nuclear Safeguards,” Los Alamos, NM (United States), Dec. 2015. doi: 10.2172/1227248.

[17] R. T. Kouzes *et al.*, “Alternatives to 3He for Neutron Detection for Homeland Security,” *Proc. Inst. Nucl. Mater. Manag. Annu. Meet.*, no. March 2015, pp. 1–9,

2010http://library3.webster.edu/login?url=http://search.ebscohost.com/login.aspx?direct=true&db=eih&AN=58108174&site=ehost-live&scope=cite.

[18] A. N. Caruso, “The physics of solid-state neutron detector materials and geometries,” *J. Phys. Condens. Matter*, vol. 22, no. 44, p. 443201, Oct. 2010. doi: 10.1088/0953-8984/22/44/443201.

[19] S. Mukhopadhyay, R. Maurer, P. Guss, and C. Kruschwitz, “Review of current neutron detection systems for emergency response,” in *Proc. SPIE 9213, Hard X-Ray, Gamma-Ray, and Neutron Detector Physics XVI*, 2014, vol. 9213, p. 92130T. doi: 10.1117/12.2058165.

[20] C. A. Kruschwitz *et al.*, “Semiconductor neutron detectors using depleted uranium oxide,” in *Hard X-Ray, Gamma-Ray, and Neutron Detector Physics Xvi*, 2014, vol. 9213, p. 92130C. doi: 10.1117/12.2063501.

[21] M. K. Parida, K. Prabakar, and S. T. Sundari, “Efficiency of depleted UO2 based semiconductor neutron detectors in direct and indirect configuration - A GEANT4 simulation study,” *J. Instrum.*, vol. 13, no. 3, 2018. doi: 10.1088/1748-0221/13/03/P03006.

[22] R. A. August, G. W. Phillips, and J. H. Cutchin, “A High Efficiency Fast Neutron Detctor,” NRL Memorandum Report, Washington, DC, 1989.

[23] “Evaluated Nuclear Data File (ENDF),” 2018. https://www.nndc.bnl.gov/exfor/endf00.jsp

[24] G. Knoll, *Radiation detection and measurement*, Fourth Edition, Hoboken, NJ: John Wiley & Sons Inc., 2010.

[25] D. S. McGregor, R. T. Klann, H. K. Gersch, and J. D. Sanders, “Designs for thin-film-coated semiconductor thermal neutron detectors,” *2001 IEEE Nucl. Sci. Symp. Conf. Rec. (Cat. No.01CH37310)*, vol. 4, pp. 2454–2458, 2001. doi: 10.1109/NSSMIC.2001.1009315.

[26] D. S. McGregor, S. L. Bellinger, and J. K. Shultis, “Present status of microstructured semiconductor neutron detectors,” *J. Cryst. Growth*, vol. 379, pp. 99–110, Sep. 2013. doi: 10.1016/j.jcrysgro.2012.10.061.

[27] “Domino Neutron Detector.” radectech.com/products/rdt-domino-v5-4.

[28] S. Majety, J. Li, X. K. Cao, R. Dahal, J. Y. Lin, and H. X. Jiang, “Metal-semiconductor-metal neutron detectors based on hexagonal boron nitride epitaxial layers,” in *Proc. SPIE 8507, Hard X-ray, Gamma-Ray, and Neutron Detctor Physics XIV*, 2012, vol. 8507, p. 85070R. doi: 10.1117/12.940748.

[29] A. Maity, S. J. Grenadier, J. Li, J. Y. Lin, and H. X. Jiang, “Hexagonal boron nitride neutron detectors with high detection efficiencies,” *J. Appl. Phys.*, vol. 123, no. 4, 2018. doi: 10.1063/1.5017979.

[30] S. Ramo, “Currents Induced by Electron Motion,” *Proc. IRE*, vol. 27, no. 9, pp. 0–1, 1939. doi: 10.1109/JRPROC.1939.228757.

[31] W. Shockley, “Currents to Conductors by a Moving Point Charge,” *J. Appl. Phys.*, vol. 9, no. 1, pp. 635–636, 1938. doi: 10.1063/1.1710367.

[32] A. Owens, *Compound Semiconductor Radiation Detectors*. Boca Raton, FL: CRC Press, 2012.

[33] H. Idriss, “Surface reactions of uranium oxide powder, thin films and single crystals,” *Surf. Sci. Rep.*, vol. 65, no. 3, pp. 67–109, Mar. 2010. doi: 10.1016/j.surfrep.2010.01.001.

[34] C. A. Colmenares, “The oxidation of thorium, uranium, and plutonium,” *Prog. Solid State Chem.*, vol. 9, no. C, pp. 139–239, 1975. doi: 10.1016/0079-6786(75)90016-3.

[35] J. L. Bates, C. A. Hinman, and T. Kawada, “Electrical Conductivity of Uranium Dioxide,” *J. Am. Ceram. Soc.*, vol. 50, no. 12, pp. 652–656, 1967. doi: 10.1111/j.1151-2916.1967.tb15021.x.

[36] R. K. Willardson, J. W. Moody, and H. L. Goering, “The electrical properties of uranium oxides,” *J. Inorg. Nucl. Chem.*, vol. 6, no. 1, pp. 19–33, Feb. 1958. doi: 10.1016/0022-1902(58)80096-2.

[37] H. P. Myers, T. Jonsson, and R. Westin, “Intrinsic semiconduction in uranium dioxide,” *Solid State Commun.*, vol. 2, no. 10, pp. 321–322, Oct. 1964. doi: 10.1016/0038-1098(64)90535-6.

[38] W. Hartmann, “Elektrische Untersuchungen an oxydischen Halbleitern,” *Zeitschrift für Phys.*, vol. 102, no. 11–12, pp. 709–733, 1936. doi: 10.1007/BF01338539.

[39] T. Meek, M. Hu, and M. J. Haire, “Semiconductive Properties of Uranium Oxides,” in *Waste Management Symposium*, 2001, pp. 0–6http://www.wmsym.org/archives/2001/14/14-3.pdf.

[40] B. G. Von Roedern, T. T. Meek, and M. J. Haire, “Some Electrical Properties of Ion-Implanted Urania — Part II: Preprint,” in *Society for the Advancement of Material and Process Engineering Symposium*, 2003https://www.nrel.gov/docs/fy03osti/33441.pdf.

[41] T. T. Meek, B. G. Von Roedern, and M. J. Haire, “Some Electrical Properties of UO2 - Part 1,” in *American Nuclear Society Annual Meeting*, 2003, pp. 0–3.

[42] P. Nagels, J. Devreese, and M. Denayer, “Electronic Conduction in Single Crystals of Uranium Dioxide,” *J. Appl. Phys.*, vol. 35, no. 4, pp. 1175–1180, Apr. 1964. doi: 10.1063/1.1713588.

[43] S. Iida, “Electrical Property of Uranium Dioxide,” *J. Phys. Soc. Japan*, vol. 20, no. 2, pp. 291–292, Feb. 1965. doi: 10.1143/JPSJ.20.291.

[44] S. Iida, “Electrical Properties of Non-Stoichiometric Uranium Dioxide,” *Jpn. J. Appl. Phys.*, vol. 4, no. 11, pp. 833–838, 1965. doi: 10.1143/JJAP.4.833.

[45] A. Rubio, “Comparative Study of the Relation Between the Electric Conductivity and Grain Size in Sintered Uranium Dioxide,” *Compt. Rend.*, vol. Ser. B, no. 9, pp. 1508–1510, 1971.

[46] L. Gmelin, *Uranium: Supplement volume*, no. pt. 3. 1979http://books.google.com/books?id=ZjsvAQAAIAAJ.

[47] R. A. Wolfe, “The Electrical Conductivity and Thermoelectric Power of Uranium Dioxide,” Office of Technical Services, Department of Commerce, Pittsburgh, 1963https://play.google.com/books/reader?id=kgYvzL_JWmYC&hl=en&pg=GBS.PP1.

[48] H. E. Schmidt, “Some considerations on the thermal conductivity of

stoichiometric uranium dioxide at high temperatures," *J. Nucl. Mater.*, vol. 39, no. 2, pp. 234–237, May 1971. doi: 10.1016/0022-3115(71)90032-8.

[49] V. Haase, H. Keller-Rudek, and et al., *Gmelin Handbook of Inorganic Chemistry Supplement Volume C5, Uranium Dioxide*, 8th ed. 1986.

[50] Z. A. Munir, "The electrical conductivity of doped and undoped uranium oxide," *Int. J. Thermophys.*, vol. 2, no. 2, pp. 177–186, Jun. 1981. doi: 10.1007/BF00503940.

[51] J. C. Killeen, "The effect of niobium oxide additions on the electrical conductivity of UO2," *J. Nucl. Mater.*, 1980. doi: 10.1016/0022-3115(80)90273-1.

[52] F. X. Zhang *et al.*, "High-pressure U3O8with the fluorite-type structure," *J. Solid State Chem.*, vol. 213, pp. 110–115, 2014. doi: 10.1016/j.jssc.2014.02.012.

[53] X. D. Wen, R. L. Martin, G. E. Scuseria, S. P. Rudin, E. R. Batista, and A. K. Burrell, "Screened hybrid and DFT + U studies of the structural, electronic, and optical properties of U3O8," *J. Phys. Condens. Matter*, vol. 25, no. 2, 2013. doi: 10.1088/0953-8984/25/2/025501.

[54] R. E. Rundle, N. C. Baenziger, A. S. Wilson, and R. A. McDonald, "The Structures of the Carbides, Nitrides and Oxides of Uranium1," *J. Am. Chem. Soc.*, vol. 70, no. 1, pp. 99–105, Jan. 1948. doi: 10.1021/ja01181a029.

[55] J. Selbin and J. D. Ortego, "Chemistry of uranium (V)," *Chem. Rev.*, vol. 69, no. 5, pp. 657–671, Oct. 1969. doi: 10.1021/cr60261a004.

[56] N. A. Brincat, S. C. Parker, M. Molinari, G. C. Allen, and M. T. Storr, "Density functional theory investigation of the layered uranium oxides U3O8and U2O5," *Dalt. Trans.*, vol. 44, no. 6, pp. 2613–2622, 2015. doi: 10.1039/c4dt02493a.

[57] B. O. Loopstra, "The structure of β-U_3O_8," *Acta Crystallogr. Sect. B Struct. Crystallogr. Cryst. Chem.*, vol. 26, no. 5, pp. 656–657, 1970. doi: 10.1107/S0567740870002935.

[58] B. O. Loopstra, "On the crystal structure of α-U_3O_8," *J. Inorg. Nucl. Chem.*, vol. 39, pp. 1713–1714, 1977.

[59] T. Matsui and K. Naito, “Electrical conductivity measurement and thermogravimetric study of pure and niobium-doped uranium dioxide,” *J. Nucl. Mater.*, vol. 136, no. 1, pp. 59–68, Oct. 1985. doi: 10.1016/0022-3115(85)90030-3.

[60] B. Szpunar and J. A. Szpunar, “Theoretical Investigation of Structural and Mechanical Properties of Uranium Oxides,” in *Uranium 2010, Proceeedings of the 3rd International Conference on Uranium*, 2010, vol. II, no. August, pp. 177–187.

[61] H. R. Hoekstra and S. Siegel, “The uranium-oxygen system: U_3O_8-UO_3,” *J. Inorg. Nucl. Chem.*, vol. 18, no. April 1960, pp. 154–165, Mar. 1961. doi: 10.1016/0022-1902(61)80383-7.

[62] P. S. Murti, R. B. Yadav, H. P. Nawada, P. R. V. Rao, and C. K. Mathews, “A study of the non-stoichiometry in U_3O_8,” *Thermochim. Acta*, vol. 140, pp. 299–303, Mar. 1989. doi: 10.1016/0040-6031(89)87311-3.

[63] G. C. Allen and N. R. Holmes, “A mechanism for the UO_2 to α-U_3O_8 phase transformation,” *J. Nucl. Mater.*, vol. 223, no. 3, pp. 231–237, 1995. doi: 10.1016/0022-3115(95)00025-9.

[64] G. Rousseau *et al.*, “A detailed study of UO_2 to U_3O_8 oxidation phases and the associated rate-limiting steps,” *J. Nucl. Mater.*, vol. 355, no. 1–3, pp. 10–20, 2006. doi: 10.1016/j.jnucmat.2006.03.015.

[65] N. Singh and M. D. Karkhanavala, “Studies of the Electrical Properties of Uranium Oxides. III. Room Temperature Measurements of the Hall Coefficients of α-U_3O_8 and delta-U_3O_8,” Atomic Energy Establishment, Bombay, India, 1964.

[66] M. A. Khilla, S. A. Elfekey, and M. E. Yahia, “Electrical-Conductivity of Some Uranium-Oxides in the Composition Range UO_3 - $U_3O_{8\text{-}z}$,” *Radiochim. Acta*, vol. 28, no. 2, pp. 115–117, 1981.

[67] N. Singh and M. D. Krakhanavala, “Studies on the electrical properties of uranium oxides II. Non-stoichiometric U_3O_8,” *Phys. Stat. Sol.*, vol. 17, pp. 501–508, 1966. doi: 10.1103/PhysRevB.81.205324.

[68] A. M. George and M. D. Karkhanavala, “Studies on the electrical properties of uranium oxides I. Electrical conductivity of α-U_3O_8,” *J. Phys. Chem. Solids*, vol. 24, pp. 1207–1212, 1963. doi: 10.1103/PhysRevB.81.205324.

[69] I. Tamotsu, N. Keiji, and O. Keichi, “Electrical conductivity study on phase transitions in U_3O_8,” *J. Nucl. Mater.*, vol. 35, no. 3, pp. 335–344, Jun. 1970. doi: 10.1016/0022-3115(70)90217-5.

[70] H. He, D. A. Andersson, D. D. Allred, and K. D. Rector, “Determination of the Insulation Gap of Uranium Oxides by Spectroscopic Ellipsometry and Density Functional Theory,” *J. Phys. Chem. C*, vol. 117, no. 32, pp. 16540–16551, Aug. 2013. doi: 10.1021/jp401149m.

[71] H. R. Hoekstra and S. Siegel, “The Uranium-Oxygen System: U_3O_8 to UO_3,” *Proc. Second United Nations Int. Conf. Peac. Use At. Energy*, vol. 28, no. Session C-10 P/1548, pp. 231–234, 1958.

[72] M. T. Weller, P. G. Dickens, and D. J. Penny, “The structure of δ-UO_3,” *Polyhedron*, vol. 7, no. 3, pp. 243–244, Jan. 1988. doi: 10.1016/S0277-5387(00)80559-8.

[73] E. H. P. Cordfunke and P. Aling, “System UO_3+ U_3O_8: dissociation pressure of γ-UO_3,” *Trans. Faraday Soc.*, vol. 61, p. 50, 1965. doi: 10.1039/tf9656100050.

[74] V. J. Wheeler, R. M. Dell, and E. Wait, “Uranium Trioxide and the UO_3 Hydrates,” *J. Inorg. Nucl. Chem.*, vol. 26, pp. 1829–1845, 1964.

[75] L. E. Sweet *et al.*, “Investigation of the polymorphs and hydrolysis of uranium trioxide,” *J. Radioanal. Nucl. Chem.*, vol. 296, no. 1, pp. 105–110, 2013. doi: 10.1007/s10967-012-2063-9.

[76] E. H. P. Cordfunke and P. C. Debets, “Preparation and properties of a new monohydrate of uranium trioxide ε-$UO_3 \cdot H_2O$,” *J. Inorg. Nucl. Chem.*, vol. 26, no. 10, pp. 1671–1677, Oct. 1964. doi: 10.1016/0022-1902(64)80094-4.

[77] M. Benedict, T. H. Pigford, and H. W. Levi, *Nuclear Chemical Engineering*, 2nd ed. 1981http://www.osti.gov/scitech/biblio/6056456.

[78] P. C. Debets, “The structure of β-UO_3,” *Acta Crystallogr.*, vol. 21, no. 4, pp.

589–593, Oct. 1966. doi: 10.1107/S0365110X66003505.

[79] C. Greaves and B. E. F. Fender, “The structure of α-UO_3 by neutron and electron diffraction,” *Acta Crystallogr. B*, vol. 28, no. 12, pp. 3609–3614, 1972. doi: 10.1107/S056774087200843X.

[80] R. Engmann and P. M. de Wolff, “The crystal structure of γ-UO_3,” *Acta Crystallogr.*, vol. 16, no. 10, pp. 993–996, Oct. 1963. doi: 10.1107/S0365110X63002656.

[81] B. O. Loopstra and E. H. P. Cordfunke, “On the structure of α-UO_3,” *Recl. des Trav. Chim. des Pays-Bas*, vol. 85, no. 2, pp. 135–142, Sep. 1966. doi: 10.1002/recl.19660850204.

[82] B. O. Loopstra, J. C. Taylor, and A. B. Waugh, “Neutron powder profile studies of the gamma uranium trioxide phases,” *J. Solid State Chem.*, vol. 20, no. 1, pp. 9–19, 1977. doi: https://doi.org/10.1016/0022-4596(77)90046-9.

[83] J. C. Taylor, “The structure of the α form of uranyl hydroxide,” *Acta Crystallogr. Sect. B Struct. Crystallogr. Cryst. Chem.*, vol. 27, no. 6, pp. 1088–1091, 1971. doi: 10.1107/S056774087100356X.

[84] L. E. Sweet *et al.*, “Investigations into the Polymorphs and Hydration Products of UO,” *Chem. Biol. Radiol. Nucl. Explos. Sens. Xiii*, vol. 8358, 2012. doi: Artn 83581r Doi 10.1117/12.919706.

[85] Z. M. Hanafi, F. M. Ismail, M. A. Khilla, and N. H. Rofail, “The Electrical Conductivity of the Different Uranium Trioxide ‘UO_3’ Phases,” *Radiochim. Acta*, vol. 49, no. 1, pp. 35–37, Jan. 1990. doi: 10.1524/ract.1990.49.1.35.

[86] M. A. Khilla and N. H. Rofail, “Optical Absorption Edge of Uranium Trioxide Phases : Part I,” *Radiochim. Acta*, vol. 40, pp. 155–158, 1986.

[87] C. A. Klein, “Bandgap Dependence and Related Features of Radiation Ionization Energies in Semiconductors,” *J. Appl. Phys.*, vol. 39, no. 4, pp. 2029–2038, Mar. 1968. doi: 10.1063/1.1656484.

[88] P. Blum, “Natural Gamma Radiation,” in *Physical Properties Handbook: A Guide to the Shipboard Measurement of Physical Properties of Deep-Sea Cores*,

ODP Technical Note, 26, 1997, pp. 5-1-5–14. doi: 10.1201/9780367812614-6.

[89] B. D. Milbrath, A. J. Peurrung, M. Bliss, and W. J. Weber, “Radiation detector materials: An overview,” *J. Mater. Res.*, vol. 23, no. 10, pp. 2561–2581, Oct. 2008. doi: 10.1557/JMR.2008.0319.

[90] I. Obodovskiy, *Fundamentals of Radiation and Chemical Safety*. 2015. doi: 10.1016/C2014-0-00520-5.

[91] “7. Natural Gamma-Ray Spectrometry,” in *Developments in Petroleum Science*, vol. 15, no. PA, 1984, pp. 113–134. doi: 10.1016/S0376-7361(08)70421-7.

[92] P. H. G. M. Hendriks, J. Limburg, and R. J. de Meijer, “Full-spectrum analysis of natural γ-ray spectra,” *J. Environ. Radioact.*, vol. 53, no. 3, pp. 365–380, Apr. 2001. doi: 10.1016/S0265-931X(00)00142-9.

[93] T. Ichimiya, T. Narita, and K. Kitao, “Natural Background Gamma-ray Spectrum List of Gamma-Rays Ordered in Energy from Natural Radionuclides,” Japan Atomic Energy Research Institute, 1998.

[94] H.-D. Choi and J. Kim, “Basic characterization of uranium by high-resolution gamma spectroscopy,” *Nucl. Eng. Technol.*, vol. 50, no. 6, pp. 929–936, Aug. 2018. doi: 10.1016/j.net.2018.04.008.

[95] “Gamma Ray Spectrum of 238U.” http://www.radiochemistry.org/periodictable/gamma_spectra/pdf/u238.pdf.

[96] “Gamma-Ray Spectrum of 235U.” http://www.radiochemistry.org/periodictable/gamma_spectra/pdf/u235.pdf.

[97] H. Guo, C. Tian, X. Wang, N. Lv, M. Ma, and Y. Wei, “Decay Chain Deduction of Uranium Fission Products,” *Health Phys.*, vol. 111, no. 1, pp. 17–21, Jul. 2016. doi: 10.1097/HP.0000000000000521.

[98] O. Litaize, D. Regnier, and O. Serot, “Prompt Fission Gamma-ray Spectra and Multiplicities for Various Fissioning Systems,” *Phys. Procedia*, vol. 59, no. C, pp. 89–94, 2014. doi: 10.1016/j.phpro.2014.10.014.

[99] P. Zigman and J. Mackin, “Early Time Decay of Fission Product Mixtures—II,” *Health Phys.*, vol. 5, no. 1, pp. 79–84, Mar. 1961. doi: 10.1097/00004032-

196103000-00010.

[100] J. R. Keane, “Gamma-ray spectrum of short lived fission products,” *Br. J. Appl. Phys.*, vol. 13, no. 3, pp. 131–133, Mar. 1962. doi: 10.1088/0508-3443/13/3/312.

[101] J. V. Boggs, “Gamma-Ray Spectra of Fission Products from U235 Fission as a Function of the Time After Fission,” The University of Oklahoma, 1966.

[102] “Uranium Radiation Properties,” 2016. http://www.wise-uranium.org/rup.html.

[103] R. L. Murray and K. E. Holbert, “Fission,” in *Nuclear Energy*, Elsevier, 2020, pp. 101–114. doi: 10.1016/B978-0-12-812881-7.00006-X.

[104] K. L. Murty and I. Charit, *An Introduction to Nuclear Materials: Fundamentals and Applications*. Wiley-VCH, 2013.

[105] L. Sweet *et al.*, “Investigation of Uranium Polymorphs,” Pacific Northwest National Laboratory, Richland, WA, 2011.

[106] W. Davies and W. Gray, “A rapid and specific titrimetric method for the precise determination of uranium using iron(II) sulphate as reductant,” *Talanta*, vol. 11, no. 8, pp. 1203–1211, Aug. 1964. doi: 10.1016/0039-9140(64)80171-5.

[107] T. Fujino, N. Sato, and K. Yamada, “Determination of the O/M ratios of polynary uranium oxides by Ce(IV)-Fe(II) back titration after dissolution in mixed sulphuric and phosphoric acids,” *Anal. Bioanal. Chem.*, vol. 354, no. 3, pp. 374–375, Jan. 1996. doi: 10.1007/s0021663540374.

[108] S. R. Dharwadkar and M. S. Chandrasekharaiah, “An improved titrimetric method for the determination of uranium: oxygen ratios,” *Anal. Chim. Acta*, vol. 45, no. 3, pp. 545–546, May 1969. doi: 10.1016/S0003-2670(01)95588-6.

[109] B. H. Toby and R. B. Von Dreele, “GSAS-II : the genesis of a modern open-source all purpose crystallography software package,” *J. Appl. Crystallogr.*, vol. 46, no. 2, pp. 544–549, Apr. 2013. doi: 10.1107/S0021889813003531.

[110] D. Simeone, G. Baldinozzi, D. Gosset, S. Le Caer, and J.-F. Bérar, “Grazing incidence X-ray diffraction for the study of polycrystalline layers,” *Thin Solid Films*, vol. 530, pp. 9–13, Mar. 2013. doi: 10.1016/j.tsf.2012.07.068.

[111] “ASTM E112-13: Standard test methods for determining average grain size,”

ASTM Int., pp. 1–28, 2013. doi: 10.1520/E0112-13.

[112] P. Kubelka and F. Munk, “Ein Beitrag zur Optik der Farbanstriche,” *Zeitschrift für Tech. Phys.*, vol. 12, pp. 593–601, 1931. doi: 10.4236/msce.2014.28004.

[113] Z. M. Khoshhesab, “Reflectance IR Spectroscopy,” in *Infrared Spectroscopy - Materials Science, Engineering and Technology Edited*, 2012, pp. 233–244. doi: 10.5772/2055.

[114] Mortimer Abramowitz, “Olympus Microscopy Resource Center | Specular and Diffuse Reflection - Java Tutorial,” *Olympus America, Inc.*, 2012. http://www.olympusmicro.com/primer/java/reflection/specular/.

[115] “Diffuse Reflection,” 2004. http://www.encyclopedia.com/science-and-technology/computers-and-electrical-engineering/computers-and-computing/diffuse.

[116] H. G. Wendlandt, Wesley Wm. Hecht, *Reflectance Spectroscopy*. Interscience Publishers, 1966.

[117] J. Tauc, “Optical properties and electronic structure of amorphous Ge and Si,” *Mater. Res. Bull.*, vol. 3, no. 1, pp. 37–46, 1968. doi: 10.1016/0025-5408(68)90023-8.

[118] M. Nowak, B. Kauch, and P. Szperlich, “Determination of energy band gap of nanocrystalline SbSI using diffuse reflectance spectroscopy,” *Rev. Sci. Instrum.*, vol. 80, no. 4, pp. 4–7, 2009. doi: 10.1063/1.3103603.

[119] P. Fochs, “The measurement of the energy gap of semiconductors from their diffuse reflection spectra,” *Proc. Phys. Soc. Sect. B*, vol. 70, pp. 70–75, 1956http://iopscience.iop.org/0370-1301/69/1/309.

[120] M. Born and R. Oppenheimer, “Zur Quantentheorie der Molekeln,” *Ann. Phys.*, vol. 389, no. 20, pp. 457–484, 1927. doi: 10.1002/andp.19273892002.

[121] P. Hohenberg and W. Kohn, “Inhomogeneous Electron Gas,” *Phys. Rev.*, vol. 136, no. 3B, pp. B864–B871, Nov. 1964. doi: 10.1103/PhysRev.136.B864.

[122] W. Kohn and L. J. Sham, “Self-Consistent Equations Including Exchange and Correlation Effects,” *Phys. Rev.*, vol. 140, no. 4A, pp. A1133–A1138, Nov. 1965.

doi: 10.1103/PhysRev.140.A1133.

[123] R. M. Martin, *Electronic Structure: Basic Theory and Practical Methods*. Cambridge: Cambridge University Press, 2004.

[124] D. C. Langreth and J. P. Perdew, “Theory of nonuniform electronic systems. I. Analysis of the gradient approximation and a generalization that works,” *Phys. Rev. B*, vol. 21, no. 12, pp. 5469–5493, Jun. 1980. doi: 10.1103/PhysRevB.21.5469.

[125] D. C. Langreth and M. J. Mehl, “Beyond the local-density approximation in calculations of ground-state electronic properties,” *Phys. Rev. B*, vol. 28, no. 4, pp. 1809–1834, 1983. doi: 10.1103/PhysRevB.28.1809.

[126] A. D. Becke, “Density-functional exchange-energy approximation with correct asymptotic behavior,” *Phys. Rev. A*, vol. 38, no. 6, pp. 3098–3100, Sep. 1988. doi: 10.1103/PhysRevA.38.3098.

[127] J. P. Perdew and Y. Wang, “Accurate and simple analytic representation of the electron-gas correlation energy,” *Phys. Rev. B*, vol. 45, no. 23, pp. 13244–13249, Jun. 1992. doi: 10.1103/PhysRevB.45.13244.

[128] J. P. Perdew, K. Burke, and M. Ernzerhof, “Generalized Gradient Approximation Made Simple,” *Phys. Rev. Lett.*, vol. 77, no. 18, pp. 3865–3868, Oct. 1996. doi: 10.1103/PhysRevLett.77.3865.

[129] C. Lee, W. Yang, and R. G. Parr, “Development of the Colle-Salvetti correlation-energy formula into a functional of the electron density,” *Phys. Rev. B*, vol. 37, no. 2, pp. 785–789, Jan. 1988. doi: 10.1103/PhysRevB.37.785.

[130] R. H. Hertwig and W. Koch, “On the parameterization of the local correlation functional. What is Becke-3-LYP?,” *Chem. Phys. Lett.*, vol. 268, no. 5–6, pp. 345–351, Apr. 1997. doi: 10.1016/S0009-2614(97)00207-8.

[131] V. I. Anisimov, F. Aryasetiawan, and A. I. Lichtenstein, “First-principles calculations of the electronic structure and spectra of strongly correlated systems: the LDA + U method,” *J. Phys. Condens. Matter*, vol. 9, no. 4, pp. 767–808, Jan. 1997. doi: 10.1088/0953-8984/9/4/002.

[132] J. Hubbard, “Electron correlations in narrow energy bands - IV. The atomic representation,” *Proc. R. Soc. London. Ser. A. Math. Phys. Sci.*, vol. 285, no. 1403, pp. 542–560, May 1965. doi: 10.1098/rspa.1965.0124.

[133] S. L. Dudarev, G. A. Botton, S. Y. Savrasov, Z. Szotek, W. M. Temmerman, and A. P. Sutton, “Electronic Structure and Elastic Properties of Strongly Correlated Metal Oxides from First Principles: LSDA + U, SIC-LSDA and EELS Study of UO2 and NiO,” *Phys. status solidi*, vol. 166, no. 1, pp. 429–443, Mar. 1998. doi: 10.1002/(SICI)1521-396X(199803)166:1<429::AID-PSSA429>3.0.CO;2-F.

[134] A. I. Liechtenstein, V. I. Anisimov, and J. Zaanen, “Density-functional theory and strong interactions: Orbital ordering in Mott-Hubbard insulators,” *Phys. Rev. B*, vol. 52, no. 8, pp. R5467–R5470, Aug. 1995. doi: 10.1103/PhysRevB.52.R5467.

[135] A. Kotani and T. Yamazaki, “Systematic Analysis of Core Photoemission Spectra for Actinide Di-Oxides and Rare-Earth Sesqui-Oxides,” *Prog. Theor. Phys. Suppl.*, vol. 108, no. 108, pp. 117–131, 1992. doi: 10.1143/PTPS.108.117.

[136] M. C. Payne, M. P. Teter, D. C. Allan, T. A. Arias, and J. D. Joannopoulos, “Iterative minimization techniques for ab initio total-energy calculations: molecular dynamics and conjugate gradients,” *Rev. Mod. Phys.*, vol. 64, no. 4, pp. 1045–1097, Oct. 1992. doi: 10.1103/RevModPhys.64.1045.

[137] G. Kresse, J. Hafner, and R. J. Needs, “Optimized norm-conserving pseudopotentials,” *J. Phys. Condens. Matter*, vol. 4, no. 36, pp. 7451–7468, Sep. 1992. doi: 10.1088/0953-8984/4/36/018.

[138] D. Vanderbilt, “Soft self-consistent pseudopotentials in a generalized eigenvalue formalism,” *Phys. Rev. B*, vol. 41, no. 11, pp. 7892–7895, Apr. 1990. doi: 10.1103/PhysRevB.41.7892.

[139] G. Kresse and J. Hafner, “Norm-conserving and ultrasoft pseudopotentials for first-row and transition elements,” *J. Phys. Condens. Matter*, vol. 6, no. 40, pp. 8245–8257, Oct. 1994. doi: 10.1088/0953-8984/6/40/015.

[140] P. E. Blöchl, “Projector augmented-wave method,” *Phys. Rev. B*, vol. 50, no. 24,

pp. 17953–17979, Dec. 1994. doi: 10.1103/PhysRevB.50.17953.

[141] G. Kresse and D. Joubert, “From ultrasoft pseudopotentials to the projector augmented-wave method,” *Phys. Rev. B*, vol. 59, no. 3, pp. 1758–1775, Jan. 1999. doi: 10.1103/PhysRevB.59.1758.

[142] C. Kittel, *Introduction to Solid State Physics*. John Wiley and Sons, Inc, 2005.

[143] G. Kresse, M. Marsman, and J. Furthmuller, “VASP the GUIDE,” 2018. https://cms.mpi.univie.ac.at/vasp/vasp.pdf.

[144] “Crystallography Open Database.” http://www.crystallography.net/cod/result.php.

[145] N. A. Brincat, S. C. Parker, M. Molinari, G. C. Allen, and M. T. Storr, “Ab initio investigation of the UO_3 polymorphs: Structural properties and thermodynamic stability,” *Inorg. Chem.*, vol. 53, no. 23, pp. 12253–12264, 2014. doi: 10.1021/ic500791m.

[146] L. J. van der Pauw, “A method of measuring the resistivity and Hall coefficient on lamellae of arbitrary shape,” *Philips Technical Review*, vol. 20. pp. 220–224, 1958. doi: 537.723.1:53.081.7+538.632:083.9.

[147] L. B. Valdes, “Resistivity Measurements on Germanium for Transistors,” *Procedings of the I.R.E.*, vol. 29, pp. 420–427, 1954. doi: 10.1109/JRPROC.1954.274680.

[148] P. Blood and J. W. Orton, *The Electrical Characterization of Semiconductors: Majority Carriers and Electron States*. San Diego, CA: Academic Press Limited, 1992.

[149] D. K. Schroder, *Semiconductor Material and Device Characterization*. Hoboken, New Jersey: John Wiley & Sons, 2006.

[150] A. Kokil, K. Yang, and J. Kumar, “Techniques for characterization of charge carrier mobility in organic semiconductors,” *J. Polym. Sci. Part B Polym. Phys.*, vol. 50, no. 15, pp. 1130–1144, Aug. 2012. doi: 10.1002/polb.23103.

[151] S. W. Tsang, S. K. So, and J. B. Xu, “Application of admittance spectroscopy to evaluate carrier mobility in organic charge transport materials,” *J. Appl. Phys.*,

vol. 99, no. 1, p. 013706, 2006. doi: 10.1063/1.2158494.

[152] N. F. MoT and R. W. Gurney, *Electronic Processes in Ionic Crystals,* 2nd ed. Oxford University Press, 1950.

[153] G. Juška, K. Arlauskas, M. Viliūnas, and J. Kočka, “Extraction Current Transients: New Method of Study of Charge Transport in Microcrystalline Silicon,” *Phys. Rev. Lett.*, vol. 84, no. 21, pp. 4946–4949, May 2000. doi: 10.1103/PhysRevLett.84.4946.

[154] M. Brinza, J. Willekens, M. L. Benkhedir, E. V. Emelianova, and G. J. Adriaenssens, “Photoconductivity methods in materials research,” *J. Mater. Sci. Mater. Electron.*, vol. 16, no. 11–12, pp. 703–713, Nov. 2005. doi: 10.1007/s10854-005-4972-7.

[155] J. Lindemuth and S.-I. Mizuta, “Hall measurements on low mobility materials and high resistivity materials,” *Proc. SPIE 8110, Thin Film Sol. Technol. III*, 2011. doi: 10.1117/12.893100.

[156] P. N. Murgatroyd, “Theory of space-charge-limited current enhanced by Frenkel effect,” *J. Phys. D. Appl. Phys.*, vol. 3, no. 2, p. 308, Feb. 1970. doi: 10.1088/0022-3727/3/2/308.

[157] J. G. Simmons, “Poole-Frenkel effect and Schottky effect in metal-insulator-metal systems,” *Phys. Rev.*, vol. 155, no. 3, pp. 657–660, 1967. doi: 10.1103/PhysRev.155.657.

[158] S. M. Sze and M. K. Lee, *Semiconductor Devices: Physics and Technology*, Third. 2012. doi: 10.1002/9780470068328.

[159] S. Tiwari and N. C. Greenham, “Charge mobility measurement techniques in organic semiconductors,” *Opt. Quantum Electron.*, vol. 41, no. 2, pp. 69–89, Aug. 2009. doi: 10.1007/s11082-009-9323-0.

[160] H. C. F. Martens, H. B. Brom, and P. W. M. Blom, “Frequency-dependent electrical response of holes in poly(p-phenylene vinylene),” *Phys. Rev. B*, vol. 60, no. 12, pp. 8489–8492, 1999.

[161] S. Ishihara, T. Okachi, and H. Naito, “Impedance spectroscopy measurements of

charge carrier mobility in 4,4’-N,N’-dicarbazole-biphenyl thin films doped with tris(2-phenylpyridine) iridium,” *Thin Solid Films*, vol. 518, no. 2, pp. 452–456, 2009. doi: 10.1016/j.tsf.2009.07.003.

[162] E. H. Hall, “On a New Action of the Magnet on Electric Currents,” *Am. J. Math.*, vol. 2, no. 3, p. 287, Sep. 1879. doi: 10.2307/2369245.

[163] W. E. Spear, “Drift mobility techniques for the study of electrical transport properties in insulating solids,” *J. Non. Cryst. Solids*, vol. 1, no. 3, pp. 197–214, Apr. 1969. doi: 10.1016/0022-3093(69)90001-5.

[164] K. Fuchs, “The conductivity of thin metallic films according to the electron theory of metals,” *Math. Proc. Cambridge Philos. Soc.*, vol. 34, no. 1, pp. 100–108, Jan. 1938. doi: 10.1017/S0305004100019952.

[165] A. F. Mayadas, M. Shatzkes, and J. F. Janak, “ELECTRICAL RESISTIVITY MODEL FOR POLYCRYSTALLINE FILMS: THE CASE OF SPECULAR REFLECTION AT EXTERNAL SURFACES,” *Appl. Phys. Lett.*, vol. 14, no. 11, pp. 345–347, Jun. 1969. doi: 10.1063/1.1652680.

[166] E. B. Rudnyi, E. A. Kaibicheva, and L. N. Sidorov, “The Electron Affinity of UO3,” *Rapid Commun. Mass Spectrosc.*, vol. 6, no. March, pp. 356–360, 1992.

[167] H. B. Michaelson, “The work function of the elements and its periodicity,” *J. Appl. Phys.*, vol. 48, no. 11, pp. 4729–4733, 1977. doi: 10.1063/1.323539.

[168] T. T. Meek and B. von Roedern, “Semiconductor devices fabricated from actinide oxides,” *Vacuum*, vol. 83, no. 1, pp. 226–228, 2008. doi: 10.1016/j.vacuum.2008.04.005.

[169] A. Axelevitch, B. Gorenstein, and G. Golan, “Investigation of Optical Transmission in Thin Metal Films,” *Phys. Procedia*, vol. 32, pp. 1–13, 2012. doi: 10.1016/j.phpro.2012.03.510.

[170] R. H. Bube, *Photoconductivity of Solids*, John Wiley & Sons, 1960.

[171] K. von Hecht, “Zum Mechanismus des lichtelektrischen Primarstromes in isolierenden Kristallen,” *Zeitschrift fur Phys.*, vol. 77, pp. 235–245, 1932. doi: 10.1007/BF01338917.

[172] L. E. Sweet *et al.*, "Investigations into the Polymorphs and Hydration Products of UO_3," *Chem. Biol. Radiol. Nucl. Explos. Sens. Xiii*, vol. 8358, pp. 1–7, 2012. doi: Artn 83581r Doi 10.1117/12.919706.

[173] "Ianthinite Mineral Data." http://webmineral.com/data/Ianthinite.shtml.

[174] L. R. Morss, N. M. Edelstein, and J. Fuger, Eds., *The Chemistry of the Actinide and Transactinide Elements*. Dordrecht: Springer Netherlands, 2006. doi: 10.1007/1-4020-3598-5.

[175] O. Sakata and M. Nakamura, "Grazing Incidence X-Ray Diffraction," in *Springer Series in Surface Sciences*, vol. 51, no. 1, 2013, pp. 165–190. doi: 10.1007/978-3-642-34243-1_6.

[176] B. F. Figgins, G. O. Jones, and D. P. Riley, "LXXVII. The thermal expansion of aluminium at low temperatures as measured by an X-ray diffraction method," *Philos. Mag.*, vol. 1, no. 8, pp. 747–758, Aug. 1956. doi: 10.1080/14786435608238150.

[177] T. Kamiya, K. Nomura, and H. Hosono, "Origins of High Mobility and Low Operation Voltage of Amorphous Oxide TFTs: Electronic Structure, Electron Transport, Defects and Doping," *J. Disp. Technol.*, vol. 5, no. 7, pp. 273–288, Jul. 2009. doi: 10.1109/JDT.2009.2021582.

[178] R. L. Hoffman, "Effects of channel stoichiometry and processing temperature on the electrical characteristics of zinc tin oxide thin-film transistors," *Solid. State. Electron.*, vol. 50, no. 5, pp. 784–787, May 2006. doi: 10.1016/j.sse.2006.03.004.

[179] J. C. Garcia *et al.*, "Structural, electronic, and optical properties of ZrO2 from ab initio calculations," *J. Appl. Phys.*, vol. 100, no. 10, p. 104103, Nov. 2006. doi: 10.1063/1.2386967.

[180] G. Hautier, A. Miglio, D. Waroquiers, G.-M. Rignanese, and X. Gonze, "How Does Chemistry Influence Electron Effective Mass in Oxides? A High-Throughput Computational Analysis," *Chem. Mater.*, vol. 26, no. 19, pp. 5447–5458, Oct. 2014. doi: 10.1021/cm404079a.

[181] M. G. Silveirinha and N. Engheta, "Transformation electronics: Tailoring the

effective mass of electrons," *Phys. Rev. B*, vol. 86, no. 16, p. 161104, Oct. 2012. doi: 10.1103/PhysRevB.86.161104.

[182] G. Schweicher, Y. Olivier, V. Lemaur, and Y. H. Geerts, "What currently limits charge carrier mobility in crystals of molecular semiconductors?," *Isr. J. Chem.*, vol. 54, no. 5–6, pp. 595–620, 2014. doi: 10.1002/ijch.201400047.

[183] Y. Amemiya and Y. Sakai, "Electron mobility in InSb-based mixed crystals," *Electr. Eng. Japan*, vol. 93, no. 6, pp. 124–130, 1973. doi: 10.1002/eej.4390930619.

[184] A. Y. Polyakov *et al.*, "Properties of Fe-doped, thick, freestanding GaN crystals grown by hydride vapor phase epitaxy," *J. Vac. Sci. Technol. B Microelectron. Nanom. Struct.*, vol. 25, no. 3, p. 686, 2007. doi: 10.1116/1.2718962.

[185] R. D. Shannon, "Revised effective ionic radii and systematic studies of interatomic distances in halides and chalcogenides," *Acta Crystallogr. Sect. A*, vol. 32, no. 5, pp. 751–767, Sep. 1976. doi: 10.1107/S0567739476001551.

[186] D. Ter Haar, Ed., *Collected Papers of L.D. Landau*, First. New York: Gordon and Breach, Science Publishers, 1965.

[187] D. J. Howarth and E. H. Sondheimer, "The theory of electronic conduction in polar semi-conductors," *Proc. R. Soc. London. Ser. A. Math. Phys. Sci.*, vol. 219, no. 1136, pp. 53–74, Aug. 1953. doi: 10.1098/rspa.1953.0130.

[188] M. I. Klinger, "Self-trapped electron and hole states," *Sov. Phys. Uspekhi*, vol. 28, no. 5, pp. 391–413, May 1985. doi: 10.1070/PU1985v028n05ABEH003797.

[189] C. G. Kuper and G. D. Whitefield, Eds., *Polarons and Excitons*. New York: Plenum Press, 1963.

[190] J. T. Devreese, "Polarons," in *digital Encyclopedia of Applied Physics*, Weinheim, Germany: Wiley-VCH Verlag GmbH & Co. KGaA, 2003, pp. 383–383. doi: 10.1002/3527600434.eap347.

[191] H. Fröhlich, "Electrons in lattice fields," *Adv. Phys.*, vol. 3, no. 11, pp. 325–361, Jul. 1954. doi: 10.1080/00018735400101213.

[192] J. M. Casado, J. H. Harding, and G. J. Hyland, "Small-polaron hopping in Mott-

insulating UO2,” *J. Phys. Condens. Matter*, vol. 6, no. 25, pp. 4685–4698, 1994. doi: 10.1088/0953-8984/6/25/007.

[193] S. S. Batsanov, E. D. Ruchkin, and I. A. Poroshina, “Refractive Indices of Uranium Compounds,” in *Physics Education*, vol. 17, no. 2, 2016, pp. 57–60. doi: 10.1007/978-981-10-0797-2_7.

[194] M. A. Khilla, S. A. El-Fekey, and N. H. Rofail, “Infrared Absorption Study of Uranium Trioxide Phases,” *Radiochim. Acta*, vol. 40, no. 4, pp. 185–190, Jan. 1986. doi: 10.1524/ract.1986.40.4.185.

[195] J. Yamashita and T. Kurosawa, “Heitler-London Approach To Electrical Conductivity and Application to d -Electron Conductions,” *J. Phys. Soc. Japan*, vol. 15, no. 5, pp. 802–821, May 1960. doi: 10.1143/JPSJ.15.802.

[196] C. M. Young, “Evaluation of Hydrothermally Synthesized Uranium Dioxide for Novel Semiconductor Applications,” Air Force Institute of Technology, 2016.

VITA

Shailesh Dhungana was born in Morang, Nepal. He completed B.Sc. and M.Sc. in Physics from Tribhuvan University, Kathmandu, Nepal. He joined the University of Missouri-Kansas City in Fall 2014 as a PhD student and started working on his research in mid-2015. He aspires to be involved in academia and/or research after graduation.